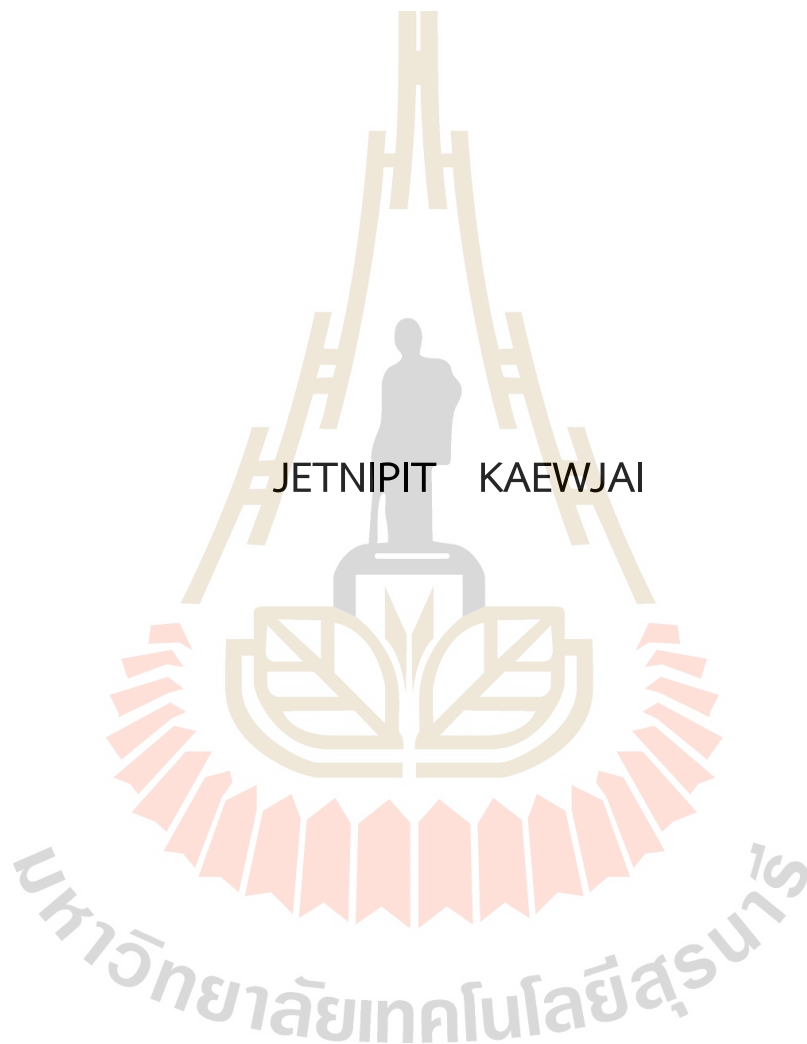


INVESTIGATION OF MONOLITHIC ACTIVE PIXEL SENSOR
FOR INNER TRACKING SYSTEM



JETNIPIT KAEWJAI

A Thesis Submitted in Partial Fulfillment of the Requirements for the
Degree of Doctor of Philosophy in Physics
Suranaree University of Technology
Academic Year 2024

การวิเคราะห์เซนเซอร์ฟิกเชลตบสนองชนิดโมโนลิทิกสำหรับระบบ
ตรวจจับทางเดินของอนุภาคชั้นใน



นายเจตนิพิฐ แก้วใจ

วิทยานิพนธ์นี้เป็นส่วนหนึ่งของการศึกษาตามหลักสูตรปริญญาวิทยาศาสตรดุษฎีบัณฑิต
สาขาวิชาฟิสิกส์
มหาวิทยาลัยเทคโนโลยีสุรนารี
ปีการศึกษา 2567

INVESTIGATION OF MONOLITHIC ACTIVE PIXEL SENSOR FOR INNER TRACKING SYSTEM

Suranaree University of Technology has approved this thesis submitted in partial fulfillment of the requirements for the Degree of Doctor of Philosophy.

Thesis Examining Committee



(Dr. Wanchaloem Poonsawat)

Chairperson



(Asst. Prof. Dr. Chinorat Kobdaj)

Member (Thesis Advisor)



(Dr. Krittada Kittimarapun)

Member



(Asst. Prof. Dr. Christoph Herold)

Member



(Prof. Dr. Yupeng Yan)

Member

มหาวิทยาลัยเทคโนโลยีสุรนารี



(Assoc. Prof. Dr. Yupaporn Ruksakulpiwat)

Vice Rector for Academic Affairs

and Quality Assurance



(Prof. Dr. Santi Maensiri)

Dean of Institute of Science

เจตนิพิฐ แก้วใจ : การวิเคราะห์เซนเซอร์พิกเซลตอบสนองชนิดโมนอลิติกสำหรับระบบ
ตรวจจับทางเดินของอนุภาคชั้นใน (INVESTIGATION OF MONOLITHIC ACTIVE PIXEL
SENSOR FOR INNER TRACKING SYSTEM). อาจารย์ที่ปรึกษา : ผู้ช่วยศาสตราจารย์
ดร.ชินรัตน์ กอบเดช, 105 หน้า.

คำสำคัญ: หัววัดอนุภาค/ เซนเซอร์พิกเซลตอบสนองชนิดโมนอลิติก/ ประสิทธิภาพการตรวจจับ
อนุภาค/ ความละเอียดเชิงพื้นที่

วิทยานิพนธ์ฉบับนี้นำเสนอการศึกษาเชิงลึกเกี่ยวกับเซนเซอร์พิกเซลตอบสนองชนิดโมนอลิ
ติกและการประยุกต์ใช้ในฟิสิกส์พลังงานสูง โดยมุ่งเน้นไปที่การพัฒนาเทคโนโลยีเซนเซอร์สำหรับหัว
วัดอนุภาค ALICE ที่เครื่องเร่งอนุภาคขนาดใหญ่ โดยเซนเซอร์ต้นแบบรุ่นใหม่ที่ใช้กระบวนการผลิต
CMOS 65 นาโนเมตร ได้รับการออกแบบสำหรับการปรับปรุงหัววัด ITS3 โดยมีการฝังชั้น deep p-
well เพื่อเพิ่มประสิทธิภาพในการเก็บรวบรวมประจุและลดงบประมาณวัสดุเหลือเพียง 0.05% X_0 ต่อ
ชั้น นอกจากนี้ ต้นแบบเซนเซอร์นี้ยังใช้เทคนิคการต่อชั้น (stitching) เพื่อสร้างเซนเซอร์ขนาดใหญ่ที่
บางเป็นพิเศษ งานวิจัยนี้มุ่งเน้นไปที่โครงสร้างทดสอบเซนเซอร์ชนิด APTS-SF ซึ่งมีจุดเด่นที่การอ่าน
ค่าแบบอนาล็อกความเร็วสูง การทดสอบในห้องปฏิบัติการได้มีการปรับแต่งพารามิเตอร์สัญญาณพัลส์
ของเซนเซอร์โดยการปรับแรงดันไบอัสและแรงดันขับเคลื่อน เพื่อให้ได้ค่าไวที่เหมาะสมที่สุด
สำหรับการตรวจจับอนุภาคได้อย่างแม่นยำ จากนั้น เซนเซอร์ถูกทดสอบกับแหล่งกำเนิดรังสี ^{55}Fe เพื่อ
วัดประสิทธิภาพการเก็บอนุภาค (CCE) โดยผลการทดลองแสดงให้เห็นว่าการเปลี่ยนแปลงแรงดันขับ
เคลื่อนมีผลกระทบต่อ CCE น้อยมาก แต่การเพิ่มแรงดันขับเคลื่อนสามารถเพิ่มค่าความกว้างของ
สัญญาณได้ นอกจากนี้ยังมีการวิเคราะห์หัตถ์พิกเซลของอนุภาค พบว่าอนุภาคไม่มีผลกระทบที่ชัดเจน
ต่อประสิทธิภาพของเซนเซอร์ การศึกษาความทนทานต่อรังสีของเซนเซอร์ดำเนินการโดยการฉายลำ
โปรตอนพลังงาน 70 MeV ที่ KCMH ภายใต้ปริมาณรังสีรวมที่ 100 krad และ 500 krad พบว่า CCE
ลดลงเมื่อได้รับปริมาณรังสีที่สูงขึ้น นอกจากนี้ยังมีการทดสอบเซนเซอร์กับลำอิเล็กตรอนพลังงาน 1.2
GeV ที่สถานีทดสอบเซนเซอร์ BTF ของสถาบันวิจัยแสงซินโครตรอน แต่ไม่ได้ผลลัพธ์ที่ชัดเจน อย่างไรก็ตาม
การทดสอบกับลำพลังงาน 120 GeV จากเครื่องเร่งอนุภาค ณ CERN SPS พบว่าเซนเซอร์มีค่า
ประสิทธิภาพการตรวจจับอนุภาคที่ 99% แม้จะได้รับปริมาณรังสีรวมสูงถึง 300 Mrad โดยเซนเซอร์
ทำงานได้ดีที่สุดที่ค่าขั้นต่ำที่ 100 อิเล็กตรอน พร้อมกับค่าความต่างศักย์ย้อนกลับที่ -4.8 V ซึ่งเป็นค่าที่
เหมาะสมที่สุดระหว่างประสิทธิภาพการตรวจจับอนุภาคและความละเอียดเชิงพื้นที่ งานวิจัยนี้มีส่วน
สำคัญในการพัฒนาเทคโนโลยี MAPS สำหรับการอัปเดตการทดลองทางฟิสิกส์พลังงานสูงในอนาคต
โดยให้ข้อมูลเชิงลึกเกี่ยวกับกลไกการเก็บประจุ ความทนทานต่อรังสี และเงื่อนไขการทำงานที่เหมาะสมที่สุด

สาขาวิชาฟิสิกส์
ปีการศึกษา 2567

ลายมือชื่อนักศึกษา เจตนิพิฐ แก้วใจ
ลายมือชื่ออาจารย์ที่ปรึกษา ชินรัตน์ กอบเดช

JETNIPIT KAEWJAI : INVESTIGATION OF MONOLITHIC ACTIVE PIXEL SENSOR FOR INNER TRACKING SYSTEM. THESIS ADVISOR : ASST. PROF. CHINORAT KOBDAJ, Ph.D. 105 PP.

Keyword: pixel sensor telescope/ monolithic active pixel sensor (MAPS)/ detection efficiency/ spatial resolution

This dissertation presents an in-depth investigation of Monolithic Active Pixel Sensors (MAPS) and their application in high-energy physics experiments, focusing on advancements in sensor technology for the ALICE experiment at LHC. A new MAPS prototype, developed using 65 nm CMOS imaging process technology, was designed for the ITS3 upgrade, incorporating a deep p-well implant to enhance charge collection and reduce the material budget to 0.05% X_0 per layer. The prototype also employs innovative stitching techniques to fabricate a large-area, ultra-thin sensor. The study specifically examines the Analog Pixel Test Structure—Source Follower (APTS-SF) sensor, characterized by its high-speed analog readout. Laboratory tests optimized the sensor's pulsing behavior through variations in bias voltage and substrate voltage, achieving an optimal trigger threshold for precise particle detection. The sensor was tested with an ^{55}Fe radioactive source to evaluate CCE. Results indicate minimal impact of substrate bias variation on CCE, although higher substrate bias improved signal amplitude. Radiation hardness studies were conducted using a 70 MeV proton beam at KCMH, exposing the sensor to total ionizing doses of 100 krad and 500 krad. The findings reveal a degradation in CCE with increasing radiation dose. Beam tests at SLRI further characterized the APTS sensor. While beam tests at the SLRI-BTF with a 1.2 GeV electron beam did not yield conclusive results, tests at CERN SPS using a 120 GeV pion beam demonstrated high detection efficiency (99%) despite irradiation with a total ionizing dose of 300 Mrad. The sensor operated optimally at a charge threshold of 100 electrons with a substrate bias of -4.8 V, balancing detection efficiency and spatial resolution. This work contributes to the ongoing development of advanced MAPS technology for future upgrades in high-energy physics experiments, providing key insights into charge collection mechanisms, radiation tolerance, and optimal sensor operating conditions.

School of Physics
Academic Year 2024

Student's Signature _____
Advisor's Signature _____
C. Kobdaj

ACKNOWLEDGEMENTS

Since my childhood, I have been captivated by the wonders of the universe. Looking up at the sky, I would marvel at the beauty of space phenomena such as comets and nebulae. It was during these moments that my curiosity sparked, and I first questioned how such phenomena occurred. Later, as I learned about the "Big Bang Theory," my interest in understanding the origins of the universe deepened, which ultimately led me to study physics from my bachelor's degree onwards. I began my doctoral studies at Suranaree University of Technology (SUT) under the One Research One Graduate (OROG) scholarship, the scholarship under Suranaree University of Technology (SUT) and my supervisor, Asst. Prof. Chinorat Kobdaj. During the first year of my Ph.D., I continued my research on particle detector sensors, building upon the work I had done during my master's degree. I am honored to be a member of the A Large Ion Collider Experiment (ALICE) at the European Organization for Nuclear Research (CERN), where I have had the opportunity to collaborate with brilliant minds who inspired me with their motivation and expertise. My involvement in ALICE led to several enriching experiences, including test beam campaigns at the Super Proton Synchrotron (SPS), Proton Synchrotron (PS), and Deutsches Elektronen-Synchrotron (DESY) in 2021 and 2022, where I investigated the Monolithic Active Pixel Sensor (MAPS) prototype under particle beams. In 2023, I had the privilege of being part of the Run Coordination (RC) crew as a Run Manager (RM), an experience that further enhanced my understanding and contributed to my growth as a researcher. I am grateful for the opportunities and challenges that have shaped my academic journey, and I look forward to continuing my research and contributing to the field of physics.

I would like to express my deepest gratitude to my supervisor, Asst. Prof. Chinorat Kobdaj, who has been a guiding mentor since my bachelor's degree and continues to support me throughout my Ph.D. journey. I am truly thankful for his advice, not only on research methodologies but also on many aspects of life that have shaped my personal and professional growth.

I would also like to thank another important supervisor and expert, Dr. Kritsada Kittimanapun, for his invaluable support and guidance. He trained me on how to operate the Beam Test Facility (BTF) at the Synchrotron Light Research Institute (SLRI),

providing me with essential knowledge for my research. Additionally, his suggestions on thesis writing were immensely helpful in refining my work.

In addition, I am grateful to the members of the Nuclear and Particle Group in the School of Physics at Suranaree University of Technology. I am extremely thankful to them for sharing their expertise, offering sincere and valuable guidance, and providing encouragement throughout my academic journey.

I would also like to express my heartfelt gratitude to my parents for their unwavering support throughout my Ph.D. journey. Their encouragement, love, and understanding have been a constant source of strength, and I am truly thankful for all they have done for me. Their belief in my abilities and their sacrifices have made it possible for me to pursue my dreams, and I am forever grateful for their presence in my life.

Finally, I would like to express my gratitude to myself for the perseverance and courage I have demonstrated throughout this Ph.D. journey. The path was not always easy, but I have grown immensely through every challenge and obstacle. This journey has not only been an academic pursuit but also a process of self-development, where I have learned to push my limits, adapt, and be resilient. I am proud of the person I have become, and I acknowledge my dedication and commitment to reaching this milestone in my life. This achievement is a reflection of my determination to stay true to my goals and to continue learning and growing, both as a researcher and as an individual.

มหาวิทยาลัยเทคโนโลยีสุรนารี

Jetnipit Kaewjai

CONTENTS

	Page
ABSTRACT IN THAI	I
ABSTRACT IN ENGLISH	II
ACKNOWLEDGEMENTS	III
CONTENTS	V
LIST OF TABLES	IX
LIST OF FIGURES	X
LIST OF ABBREVIATIONS	XVII
CHAPTER	
I INTRODUCTION	1
1.1 Quantum Chromodynamic (QCD)	2
1.1.1 Hadronic phase	3
1.1.2 Quark-gluon plasma (QGP) phase	3
1.1.3 Color superconductivity	4
1.2 A Large Ion Collider Experiment (ALICE)	4
1.2.1 The ALICE motivations	4
1.2.2 ALICE apparatus	5
1.2.3 Present Inner Tracking System (ITS2)	7
1.2.4 ALICE upgrade plan	8
1.3 Thesis outline	10
II MONOLITHIC ACTIVE PIXEL SENSOR FUNDAMENTALS	12
2.1 Monolithic Active Pixel Sensor (MAPS)	12
2.1.1 Semiconductor Physics	12
2.1.2 Electronic band structure	14
2.1.3 P-N Junction	15
2.1.4 Electric Field in the Depletion Region	16
2.1.5 Effect of Magnetic Field	16
2.1.6 Reverse Bias in a P-N Junction	17
2.1.7 Operation principles of MAPS	18
2.2 Silicon properties of MAPS	19

CONTENTS (Continued)

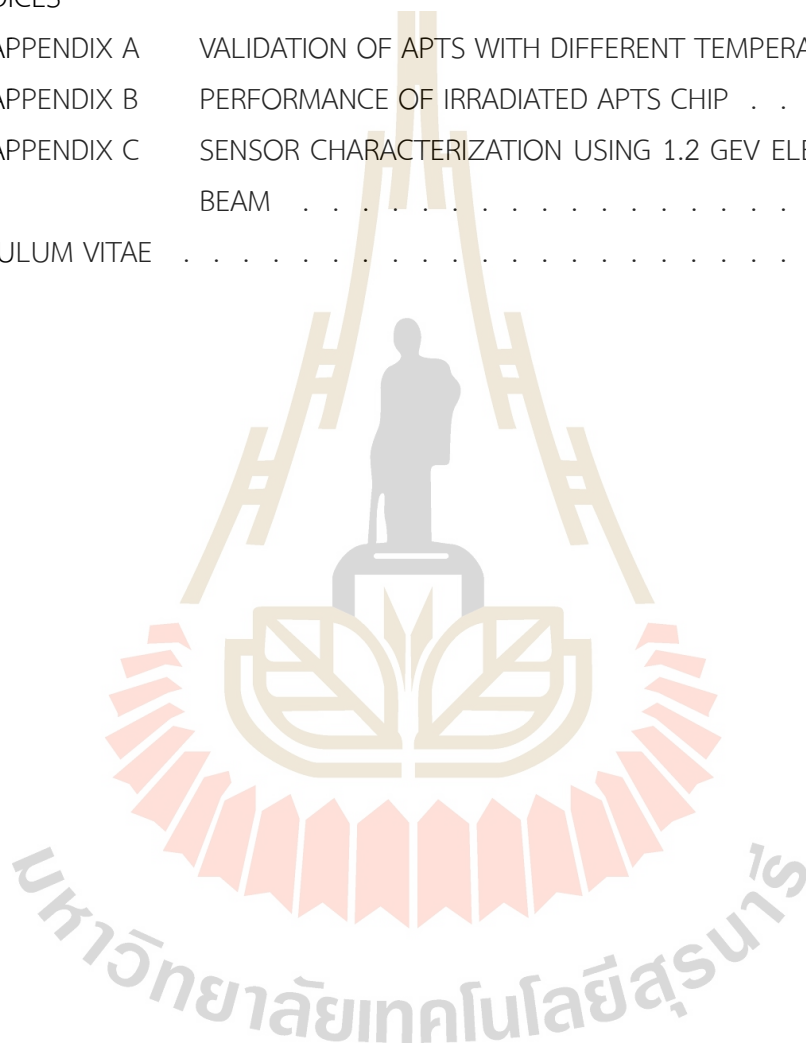
		Page
	2.2.1 Interaction of Charged Particles with Matter	19
	2.2.2 Ionization and Excitation	19
	2.2.3 Bremsstrahlung Radiation	20
	2.2.4 Cherenkov Radiation	21
	2.2.5 Bethe–Bloch Formula for Stopping Power	22
2.3	Radiation damage	23
	2.3.1 Non-ionizing radiation damage	24
	2.3.2 Ionizing radiation damage	24
2.4	Coulomb Scattering of Particles in Matter	25
	2.4.1 Single Scattering	26
	2.4.2 Plural Scattering	26
	2.4.3 Multiple Scattering	27
2.5	Properties of MAPS	28
	2.5.1 Detection efficiency	28
	2.5.2 Spatial resolution	28
	2.5.3 Charge threshold	29
	2.5.4 Fake-hit rate	29
	2.5.5 Noise	29
	2.5.6 Charge collection efficiency	31
	2.5.7 Other sensor parameters	32
	2.5.8 Conclusion	33
III	THE STUDY OF MAPS PARAMETERS FOR ITS3	34
	3.1 Inner Tracking System concept	34
	3.2 Chip architecture	37
	3.2.1 Digital Pixel Test Structure	37
	3.2.2 Analog Pixel Test Structure	38
	3.2.3 Circuit Exploratoire 65 nm (CE65)	39
	3.3 Basic chip tests	40
	3.3.1 Pulsing signal	40
	3.3.2 Trigger threshold	41
	3.4 Performance of the chip	42

CONTENTS (Continued)

		Page
	3.4.1 ^{55}Fe radioactive source	42
	3.4.2 Observable in ^{55}Fe analysis	43
	3.4.3 Performance at different temperatures	45
	3.5 Radiation hardness performance of sensor	48
	3.5.1 The radiation test at HRH Princess Maha Chakri Sirindhorn Proton Center (HRSP)	48
	3.5.2 Conclusion	49
IV	BEAM TEST CHARACTERIZATION USING BEAM AT SLRI-BTF	52
	4.1 SYNCHROTRON LIGHT RESEARCH INSTITUTE (SLRI)	52
	4.1.1 BEAM TEST FACILITY (BTF)	53
	4.1.2 Intensity reduction system	53
	4.1.3 Energy selection for SLRI-BTF	54
	4.2 Pixel sensor telescope setup	55
	4.2.1 Experimental setup	55
	4.2.2 EUDAQ framework	57
	4.3 Testbeam results	58
	4.3.1 Analysis tools and method	59
	4.3.2 Alignment and residual	62
	4.3.3 Detection efficiency	64
	4.3.4 Spatial resolution and average cluster size	65
	4.4 Summary	66
V	SIMULATION OF CHARGE COLLECTION PROCESS IN MAPS	68
	5.1 G4Beamline simulation	68
	5.2 Simulation Process with G4Beamline	69
	5.3 Data Flow for Digitizing and Analyzing Sensor Data	69
	5.4 Results	72
	5.4.1 Hitmap	72
	5.4.2 Energy deposit	72
	5.4.3 Energy to Electron-Hole Pair Conversion	73
	5.4.4 Cluster size	75
	5.4.5 Summary	77

CONTENTS (Continued)

	Page
VI SUMMARY AND CONCLUSION	79
REFERENCES	81
APPENDICES	
APPENDIX A VALIDATION OF APTS WITH DIFFERENT TEMPERATURE .	88
APPENDIX B PERFORMANCE OF IRRADIATED APTS CHIP	98
APPENDIX C SENSOR CHARACTERIZATION USING 1.2 GEV ELECTRON BEAM	102
CURRICULUM VITAE	105



LIST OF TABLES

Table		Page
1.1	The expected particles that can be detected by ITS2.	5
1.2	The geometrical specifications of the ITS2 (Abelev, B., Adam, J., Adamová, D., Aggarwal, M. M., Aglieri Rinella, G., Agnello, M., . . . Zyzak, M., 2014).	9
3.1	Geometrical specifications of ITS3.	37
3.2	Analog Pixel Test Structure main characteristics.	39
3.3	The ⁵⁵ Fe emissions produced (Podgorsak, 2009). The values in parentheses represent inaccuracies in the final digit(s) of the preceding value.	44
3.4	Parameters setting for ⁵⁵ Fe radiation source testing.	44
4.1	Parameters of the electron beam at the High-Energy Beam Transport Line (HBT).	54
4.2	Parameters to extract electron beam at different energies (Kittimanapun et al., 2024).	56
4.3	The detection efficiency value of APTS chip at different charge threshold with variant substrate back bias.	65

LIST OF FIGURES

Figure		Page
1.1	The diagram of quantum chromodynamic phases (Satz, 2011).	2
1.2	Layout of the ALICE detector (Abelev, B., Adam, J., Adamová, D., Aggarwal, M. M., Aglieri Rinella, G., Agnello, M., . . . Zyzak, M., 2014).	6
1.3	ITS2 concept. ITS2 is composed of seven cylindrical silicon detector layers placed coaxially around the beam pipe (Abelev, B., Adam, J., Adamová, D., Aggarwal, M. M., Aglieri Rinella, G., Agnello, M., . . . Zyzak, M., 2014).	7
1.4	ITS2 installation. (collaboration, 2024)	8
2.1	Structure and lattice of pure silicon. (a) A single silicon atom with four valence electrons. (b) These electrons form covalent bonds with neighboring atoms, resulting in a crystal lattice structure.	13
2.2	The drawing schematic of N-type and P-type atomic structures. (Source: http://www.answers.com/topic/N-type-silicon-technology)	14
2.3	The illustration of N-type (left) and P-type (right) doped semiconductor band structures. (Source: http://hyperphysics.phy-astr.gsu.edu)	15
2.4	Potential difference across the junction between P-type and N-type semiconductors. The P-N junction is formed upon contact between the two materials.	16
2.5	A drawing cross section of a MAPS pixel (not scale) (Abelev, B., Adam, J., Adamová, D., Aggarwal, M. M., Aglieri Rinella, G., Agnello, M., . . . Zyzak, M., 2014).	18
2.6	Ionization caused by a charged particle. A secondary electron with sufficient kinetic energy to induce further ionization is known as a delta ray. Secondary electrons represent the negative half of an ion pair.	20
2.7	Excitation by a charged particle. An electron is raised from the K-shell to the L-shell. Upon returning to a lower energy state, a photon is emitted.	21

LIST OF FIGURES (Continued)

Figure		Page
2.8	Layout of multiple Coulomb scattering of charged particles (Meroli, 2015).	25
3.1	Distribution of the material budget of all components of ITS2 (collaboration, 2024).	35
3.2	Distribution of the material budget of all components of ITS3 (collaboration, 2024).	36
3.3	Layout of the ITS3 Inner Barrel (collaboration, 2024).	36
3.4	The MLR1 architecture: APTS prototype including SF (Source Follower) and OA (Operational Amplifier), CE65 and DPTS prototype (collaboration, 2024).	38
3.5	APTS Source Follower (SF) chip in microscope scale (collaboration, 2024).	39
3.6	APTS Operational Amplifier (OA) chip in microscope scale (collaboration, 2024).	40
3.7	Laboratory test setup. Panel (a) shows a schematic diagram of the experimental setup, and panel (b) presents the actual relativistic experimental configuration.	41
3.8	The relation between maximum amplitude of pulsing signal at different pulsing bias voltage (V_H) under various back bias voltage (V_{BB}).	42
3.9	The relationship between noise frequency and trigger threshold.	43
3.10	The relationship between relative frequency and cluster size of APTS sensor at different back-bias voltage.	45
3.11	The plots of APTS sensor performances for detecting the particles from the ^{55}Fe decay.	46
3.12	The experimental setup for testing sensor performance under different temperatures. Panel (a) shows the chip test setup, and panel (b) shows the setup placed inside the temperature-controlled incubator.	47

LIST OF FIGURES (Continued)

Figure		Page
3.13	The relation chip between charge collection efficiency (CCE) and back-bias voltage (V) at different temperatures.	47
3.14	The sensor setup for irradiation with 70 MeV proton beam at HRSP.	49
3.15	The relationship between mean cluster size (left) and noise (right) and back-bias voltage before and after being irradiated by a proton beam.	50
3.16	The relationship between the charge collection efficiency and back-bias voltage before and after being irradiated by a proton beam.	51
4.1	Layout of the Siam Photon Source (SPS) injector consisting of an electron gun, a coupled 40-MeV linacs, a Low-energy Beam-Transport line (LBT), a synchrotron booster, and a high-energy beam-transport line (HBT) (Kittimanapun, K., Chanlek, N., Klysubun, P., Kobdaj, C., Lakrathok, A., Laojamnongwong, N., . . . Musa, L., 2019).	53
4.2	The installation of the tungsten target manipulator. The aim is to reduce the particle intensity of the 40 meV electron beam at the synchrotron booster. (Kittimanapun, K., Chanlek, N., Klysubun, P., Kobdaj, C., Lakrathok, A., Laojamnongwong, N., . . . Musa, L., 2019).	55
4.3	Electron beam profile of the first plane that captured at the SLRI-BTF (Kittimanapun et al., 2024).	56
4.4	The SLRI-BTF pixel sensor telescope experiment (left) and the pixel sensor telescope concept (right) (Kaewjai et al., 2019).	57
4.5	The electron hit position. The upper figure shows the low electron beam intensity (<5 of clusters) and the lower figure shows the high electron beam intensity (>30 of clusters).	58

LIST OF FIGURES (Continued)

Figure		Page
4.6	The EUDAQ network typically consists of several components, including the central command and control server known as Run Control, the Data Collector, which is responsible for creating global events and storing them on disk, the Log Collector, which manages and displays log messages, and the monitor application, which allows for real-time monitoring of data quality (Spannagel, 2016).	59
4.7	The board for data collecting. The external signal from the trigger system is received through the trigger-in port. The same signal is used as an output in the trigger-out. The Alterla FPGA is included in the board and is used to operate the EUDAQv2 firmware.	60
4.8	The scheme of the telescope setup consists of planes 3 and 4, which were made with APTS chips, and all others with ALPIDE chips. The telescope setup is not to scale. The setup was set at the SPS test beams.	60
4.9	Pixel sensor telescope signal chain layout. The figure illustrates the wiring configuration of the ALPIDE sensors within the telescope, showing the paths of the trigger (TRG) chain and busy chain. The trigger chain (red arrows) initiates event acquisition, while the busy chain (blue arrows) manages readout synchronization and prevents overlapping triggers during data acquisition.	61
4.10	Residual distributions in global X (upper row) and global Y (lower row) coordinates at different negative substrate bias voltages (V_{BB}): 0.0 V (left), -1.2 V (middle), and -4.8 V (right). Each histogram illustrates the difference between the measured hit position (x_{hit}, y_{hit}) and the reconstructed track position (x_{track}, y_{track}).	63
4.11	Detection efficiency plot of a 300 Mrad irradiated chip at various reverse substrate voltages as a function of the charge threshold. APTS with $15 \mu\text{m}$ pitch, modified with gap.	64

LIST OF FIGURES (Continued)

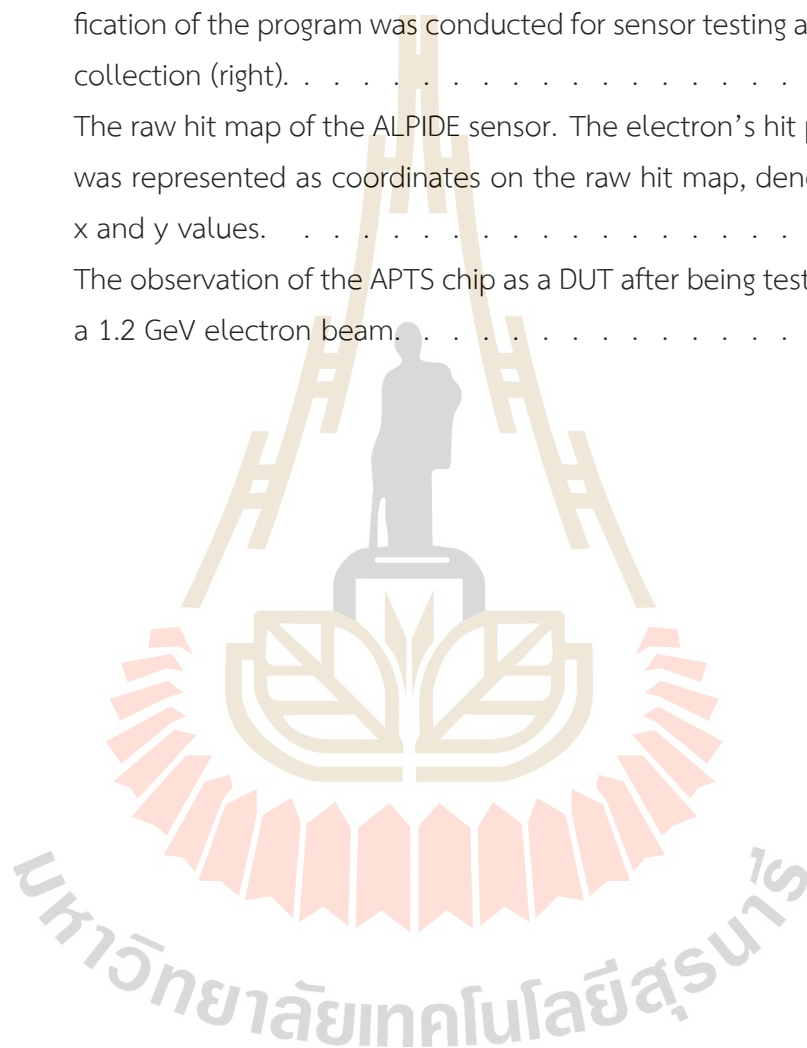
Figure		Page
4.12	The spatial resolution (solid lines) and average cluster size (dashed lines) at different charge threshold with variant substrate back bias.	66
5.1	The simulation of 1.2 GeV electron beam passing through a pixel sensor telescope, and consisting of six silicon sensors as reference planes and one APTS chip as DUT.	70
5.2	Beam profile on ALPIDE sensor in the case of a charge threshold of 100 electrons. The beam profile is performed by using G4beamline software to do a simulation and using ROOT to analyze for analysis process.	73
5.3	Distribution of energy deposit (E_{dep}) of 1.2 GeV electron beam on APTS sensor.	74
5.4	Cluster size distribution for a charge threshold of 80 electrons.	75
5.5	Cluster size distribution for a charge threshold of 100 electrons.	76
5.6	Cluster size distribution for a charge threshold of 250 electrons.	76
5.7	Average cluster size vs. charge threshold. This plot shows how the average cluster size decreases as the charge threshold increases from 80 to 250 electrons, indicating that higher thresholds require more charge to trigger a cluster, demonstrating that as the threshold rises, the number of detected pixels per cluster decreases.	77
A.1	APTS Source scan under low to normal temperature (10 - 35 degrees Celsius) at different substrate bias.	89
A.2	Plusing signal of 16 pixels of APTS chip at substrate bias of 0.0 V under temperature of 60 degree Celsius.	90
A.3	Plusing signal of 16 pixels of APTS chip at substrate bias of -1.2 V under temperature of 60 degree Celsius.	90
A.4	Plusing signal of 16 pixels of APTS chip at substrate bias of -2.4 V under temperature of 60 degree Celsius.	91
A.5	Plusing signal of 16 pixels of APTS chip at substrate bias of -3.6 V under temperature of 60 degree Celsius.	91

LIST OF FIGURES (Continued)

Figure		Page
A.6	Plusing signal of 16 pixels of APTS chip at substrate bias of -4.8 V under temperature of 60 degree Celsius.	92
A.7	Plusing signal of 16 pixels of APTS chip at substrate bias of 0.0 V under temperature of 50 degree Celsius.	92
A.8	Plusing signal of 16 pixels of APTS chip at substrate bias of -1.2 V under temperature of 50 degree Celsius.	93
A.9	Plusing signal of 16 pixels of APTS chip at substrate bias of -2.4 V under temperature of 50 degree Celsius.	93
A.10	Plusing signal of 16 pixels of APTS chip at substrate bias of -3.6 V under temperature of 50 degree Celsius.	94
A.11	Plusing signal of 16 pixels of APTS chip at substrate bias of -4.8 V under temperature of 50 degree Celsius.	94
A.12	Plusing signal of 16 pixels of APTS chip at substrate bias of 0.0 V under temperature of 40 degree Celsius.	95
A.13	Plusing signal of 16 pixels of APTS chip at substrate bias of -1.2 V under temperature of 40 degree Celsius.	95
A.14	Plusing signal of 16 pixels of APTS chip at substrate bias of -2.4 V under temperature of 40 degree Celsius.	96
A.15	Plusing signal of 16 pixels of APTS chip at substrate bias of -3.6 V under temperature of 40 degree Celsius.	96
A.16	Plusing signal of 16 pixels of APTS chip at substrate bias of -4.8 V under temperature of 40 degree Celsius.	97
B.1	Plusing signal of non-irradiated APTS chip at different substrate bias.	99
B.2	Plusing signal of irradiated APTS chip with 100krad TID at different substrate bias.	100
B.3	Plusing signal of irradiated APTS chip with 500krad TID at different substrate bias.	101
C.1	Drawing schematic of the pixel sensor telescope. The APTS serves as the DUT, and the ALPIDE sensors are positioned in front of and behind the DUT as reference planes (left). The trigger signal wire is utilized for signal transmission within the sensor (right).	102

LIST OF FIGURES (Continued)

Figure		Page
C.2	The installation of the pixel sensor telescope. The setup was positioned in front of the electron beam's trajectory (left). A verification of the program was conducted for sensor testing and data collection (right).	103
C.3	The raw hit map of the ALPIDE sensor. The electron's hit position was represented as coordinates on the raw hit map, denoted by x and y values.	104
C.4	The observation of the APTS chip as a DUT after being tested with a 1.2 GeV electron beam.	104



LIST OF ABBREVIATIONS

ALICE	A Large Ion Collider Experiment
ALPIDE	ALICE Pixel Detector
APTS OA	Analog Pixel Test Structure - Operational Amplifier
APTS SF	Analog Pixel Test Structure - Source follower
CCE	Charge Collection Efficiency
CE65	Circuit Exploratoire 65 nm
CMOS	Complementary Metal Oxide Semiconductor
DAQ	Data Acquisition
DPTS	Digital Pixel Test Structure
DUT	Device Under Test
FPGA	Field-programmable gate array
GBL	General Broken Lines
GUI	Graphical User Interface
HBT	High-energy Beam Transport
HRSP	HRH Princess Maha Chakri Sirindhorn Proton Center
IB	Inner Barrel
ITS	Inner Tracking System
KCMH	King Chulalongkorn Memorial Hospital
LBT	Low-energy Beam Transport
LET	Linear Energy Transfer
LINAC	Linear Accelerator
LS	Long Shutdown
MAPS	Monolithic Active Pixel Sensor
MC	Monte Carlo
MeV	Mega Electron Volt
MLR1	Multi Layer Reticle 1
NIEL	Non-Ionizing Energy Loss

CHAPTER I

INTRODUCTION

A Large Hadron Collider (LHC) is provided by the European Organization for Nuclear Research (CERN). The accelerator has been running since 10th September 2008 (Lebrun, 2010). Several collaborations run experiments using the LHC, the most high-energy accelerator in the world. There are nine experiments (Gray, 2024) around the LHC ring, which can be separated by the size of the detector. The biggest of these experiments are the AToroidal LHC ApparatuS (ATLAS) and the Compact Muon Solenoid (CMS), which focus on the investigation of the largest range of physics possible. A Large Ion Collider Experiment (ALICE) and a Large Hadron Collider Beauty (LHCb) have detectors specialized in focusing on specific phenomena.

The two smaller LHC experiments are the Large Hadron Collider forward (LHCf) and the TOTal Elastic and diffractive cross section Measurement (TOTEM). Both aim to study forward particles, heavy ions or protons, that avoid direct collisions by just brushing past one another. Monopole and Exotics Detector at the LHC (MoEDAL) is a detector that was deployed near LHCb and aims to search for a hypothetical particle. The ForwArd Search ExpeRiment (FASER) and the Scattering and Neutrino Detector (SND), the two new detectors at the LHC, are located close to the ATLAS experiment to search for light particles and neutrinos.

ALICE, being one of the four main experimental stations along the LHC at CERN, is devoted to research into the physics of highly interacting nuclear matter and the features of quantum chromodynamics (QCD) (Satz, 2011). Understanding some properties would significantly contribute to a better understanding of quark-gluon plasma (QGP) (Mrowczynski, 1999). One of the primary goals is to investigate the characteristics of charm hadrons. ALICE is particularly interested in the charm and beauty hadrons, which can be determined based on the creation of D mesons and Λ_c in lead-lead collisions. ALICE is also interested in the reconstruction of particles with low momentum (<1 GeV/c) (Abelev, B., Adam, J., Adamová, D., Aggarwal, M. M., Aglieri Rinella, G., Agnello, M., . . . Zyzak, M., 2014).

1.1 Quantum Chromodynamic (QCD)

QCD is a physics theory that can describe the strong nuclear force (Skands, 2013). The strong force is a fundamental interaction that establishes the confinement of quarks within protons, neutrons, and other particles belonging to the hadron group. The atomic nucleus is formed by the binding of protons and neutrons. Quarks are considered elementary particles and are fundamental building blocks of matter that combine to form composite particles such as protons and neutrons. There are six different flavors of quarks (Bai and Long, 2018): up, down, charm, strange, top, and bottom, and three different colors, including red, green, and blue. The phase diagram of QCD (Biesdorf et al., 2023) refers to different states of matter that correspond to different temperatures and density ranges as in Figure 1.1.

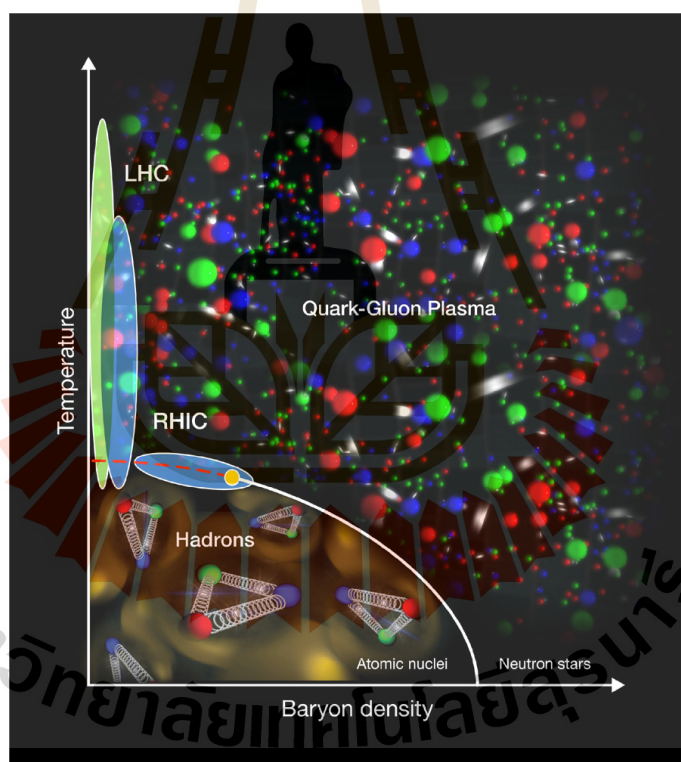


Figure 1.1 The diagram of quantum chromodynamic phases (Satz, 2011).

The QCD phase diagram is a rich tapestry reflecting the behavior of strongly interacting matter under varying temperature (T) and baryon chemical potential (μ_B). Three primary regimes are typically discussed: the hadronic phase, the quark–gluon plasma (QGP), and color superconducting phases. Each of these regimes is characterized by distinct patterns of symmetry breaking and effective degrees of freedom.

1.1.1 Hadronic phase

This state refers to a low-temperature and low-density region where quarks are confined within color-neutral hadrons such as protons and neutrons. During this phase, quarks cannot escape as unbound particles. Due to the low temperature, the strong force is the dominant factor. In this regime, quarks and gluons are confined within hadrons, and the effective degrees of freedom are mesons and baryons. A central feature of this phase is the spontaneous breaking of chiral symmetry. The non-zero chiral condensate $\langle \bar{q}q \rangle$ serves as an order parameter, and its non-vanishing value gives rise to the appearance of (pseudo-)Goldstone bosons, most notably the pions, which dominate the low-energy spectrum. Chiral effective field theories, such as chiral perturbation theory, have been particularly successful in describing interactions in this phase. The dynamics in the hadronic phase are non-perturbative, and techniques such as lattice QCD provide valuable quantitative insights into properties like hadron masses and interaction strengths (Yagi et al., 2005).

1.1.2 Quark-gluon plasma (QGP) phase

At high temperatures and densities, the strong nuclear force diminishes. This condition allows the quarks and gluons to exist independently as free particles. Lattice QCD simulations have identified this transition (or crossover at small μ_B) to occur at temperatures around $T_c \sim 150\text{--}160$ MeV. The study of quark-gluon plasma aims to determine the high energy density conditions that existed in the universe during the matter formed from elementary degrees of freedom (quarks, gluons) at about $20 \mu s$ after the Big Bang. The first observation of quark-gluon plasma occurred in the year 2000 at CERN, a laboratory in Switzerland (Heinz and Jacob, 2000). Additionally, the equation of state derived from lattice QCD calculations plays a crucial role in hydrodynamic models that describe the expansion and cooling of the QGP created in heavy-ion collisions.

ALICE experiment is specifically designed to investigate the phase structure of Quantum Chromodynamics (QCD), particularly the properties of the quark-gluon plasma (QGP). The QGP is a state of deconfined quarks and gluons that is believed to have existed microseconds after the Big Bang and can be recreated in ultra-relativistic heavy-ion collisions, such as those performed by ALICE in lead-lead (Pb-Pb) interactions.

1.1.3 Color superconductivity

Quarks have the potential to transition into a state referred to as color superconductivity in areas characterized by high density, such as the cores of neutron stars (Menezes, 2021). In this particular state, quarks exhibiting contrasting colors and flavors have the propensity to combine, leading to the emergence of a condensed state devoid of any overall color charge. Consequently, this configuration results in the quarks exhibiting behavior similar to particles of negligible mass. The theoretical study of color superconductivity is challenged by the sign problem in lattice QCD at finite baryon chemical potential, making effective models such as the Nambu–Jona-Lasinio (NJL) model indispensable for exploring these phases (Buballa, 2005). Despite these challenges, research into color superconductivity continues to provide promising insights into the behavior of dense quark matter.

1.2 A Large Ion Collider Experiment (ALICE)

ALICE provides an extensive examination of the phenomena of electrons, photons, muons, hadrons, and jets that arise as a result of collisions between heavy ions. The precision of measurements is enhanced by the utilization of p-p and p-Pb collisions, which accelerate the heavy ion and generate a quantitative reference point for comparing with results obtained from Pb-Pb collisions. The primary objective of the ALICE experiment is to investigate the characteristics of quark-gluon plasma, a state of matter that is hypothesized to have existed shortly after the Big Bang (Abelev, B., Adam, J., Adamová, D., Aggarwal, M. M., Aglieri Rinella, G., Agnello, M., . . . Zyzak, M., 2014). ALICE aims to recreate the conditions of the early cosmos and investigate the behavior of matter at exceedingly high temperatures and densities by using heavy ions in high-energy collisions. The experiment additionally investigates the strong force that holds quarks and gluons together within protons and neutrons.

1.2.1 The ALICE motivations

The interaction between nuclei can be studied to understand a strong nuclear force. Neutrons and protons are the two distinctive types of particles that comprise the nuclei. Protons are defined by their positive electric charge, while neutrons are electrically neutral. The particles are bound together by the strong nuclear force. Up quarks and down quarks constitute the fundamental building blocks of protons and

neutrons. A low-energy accelerator can generate collisions that produce quarks with low mass. In order to investigate strange and charm quarks, it is necessary to generate them using a high-energy accelerator, as their masses are higher than those of up and down quarks.

The ALICE experiment aims to investigate the production of hypertriton and charm lambda baryon (Λ_c) particles in order to gain insights into the strong nuclear force and the characteristics of strange and charm quarks. The detection performance of the current ITS is presented in Table 1.1. This table demonstrates the ability of the ITS to identify lambda particles, such as Λ_c and D mesons. This further validates the capability of detectors to detect particles with a high mass at low transverse momentum.

1.2.2 ALICE apparatus

The ALICE apparatus, as depicted in Figure 1.2, comprises a center barrel. The aforementioned component serves the purpose of measuring the direction and energy of hadrons, electrons, and photons. The center barrel is designed to accommodate polar angles ranging from 45 degrees to 135 degrees. It is implanted in a large solenoid magnet by moving from the center to the periphery. This particular compo-

Table 1.1 The expected particles that can be detected by ITS2.

Observable	ITS2
D meson R_{AA}	$p_T > 0$, 0.3%
D_s meson R_{AA}	$p_T > 1$, 1%
D meson from B R_{AA}	$p_T > 0$, 2.5%
D meson elliptic flow (for $\nu_2 = 0.2$)	$p_T > 0$, 2.5%
D from B elliptic flow (for $\nu_2 = 0.1$)	$p_T > 2$, 20%
Charm baryon/meson ratio (Λ_c/D)	$p_T > 2$, 15%
J/Ψ R_{AA} (forward y)	$p_T > 0$, 0.3%
J/Ψ R_{AA} (central y)	$p_T > 0$, 0.5%
J/Ψ elliptic/flow (forward y, for $\nu_2 = 0.1$)	$p_T > 0$, 0.5%
Ψ	$p_T > 0$, 10%
Temperature IMR	20% on T
Elliptic flow IMR (for $\nu_2 = 0.1$)	20%
Low-mass vector spectral function	$p_T > 0.3$, 20%

ment comprises many detectors. A detailed explanation of the Inner Tracking System (ITS) will be presented in the next part. In order to track and identify charged particles, a cylindrical Time-Projection Chamber (TPC) is used. In addition, Time-of-Flight (TOF) is used to measure the arrival time of the particle. Furthermore, Transition Radiation (TRD) is used to perform electron identification and triggering on electrons and jets. Both PHOS and EMCAL are electromagnetic calorimeters. The forward muon arm (2 degrees to 9 degrees) consists of a complex system of absorbers. They are composed of three components: a large dipole magnet, a tracking system that has fourteen layers, and triggering chambers. ALICE also has a number of smaller detectors, including the zero-degree calorimeter (ZDC), photon multiplicity detector (PMD), forward multiplicity detector (FMD), and fast timing and trigger detector (T0 and V0). These are used to characterize global events and find the angles of small particles. ACORDE is a cosmic ray detector that uses three top faces of the ALICE magnet to hold an array of plastic scintillator counters. Triggering cosmic rays was the primary goal.

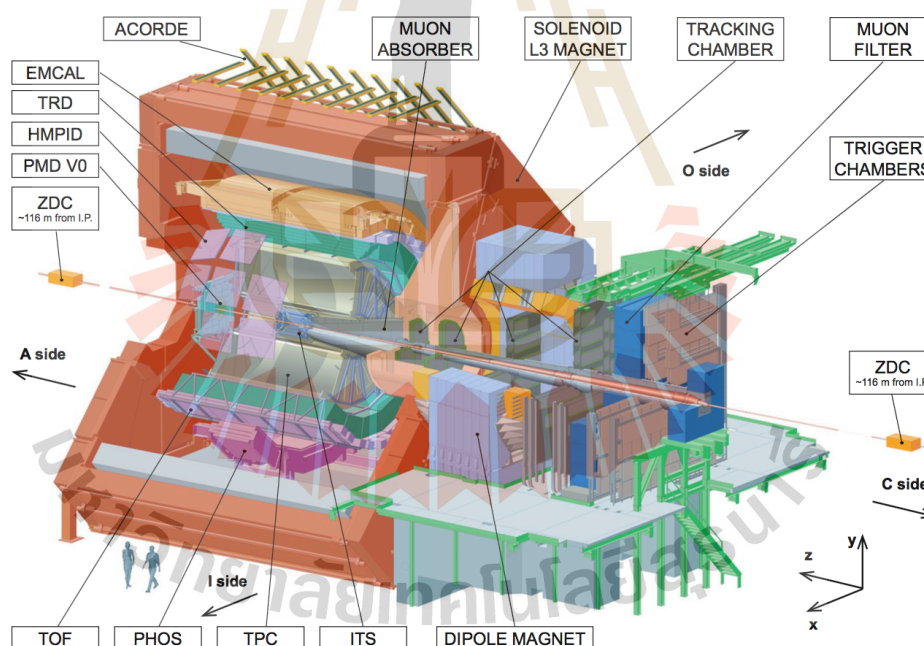


Figure 1.2 Layout of the ALICE detector (Abelev, B., Adam, J., Adamová, D., Aggarwal, M. M., Aglieri Rinella, G., Agnello, M., . . . Zyzak, M., 2014).

1.2.3 Present Inner Tracking System (ITS2)

The present version of the ITS is referred to as “ITS2” (see Figure 1.3). Seven cylinders of silicon layers are arranged in a coaxial design surrounding the beam pipe. For vertices that are within $z = \pm 60$ mm of the nominal interaction point, their pseudo-rapidity range is $|\eta| < 0.9$, and the distance between the first and last layers of the ITS is 39 mm and 430 mm, respectively.

ITS that is an innermost system of ALICE is dedicated to track particles. The ITS is a key part of track reconstruction, and its goal is to improve the position, angle, and momentum resolution of reconstructed tracks. The ITS detects particles according to their particular energy loss per unit length, which is dependent only on their charge and rest mass for a given momentum.

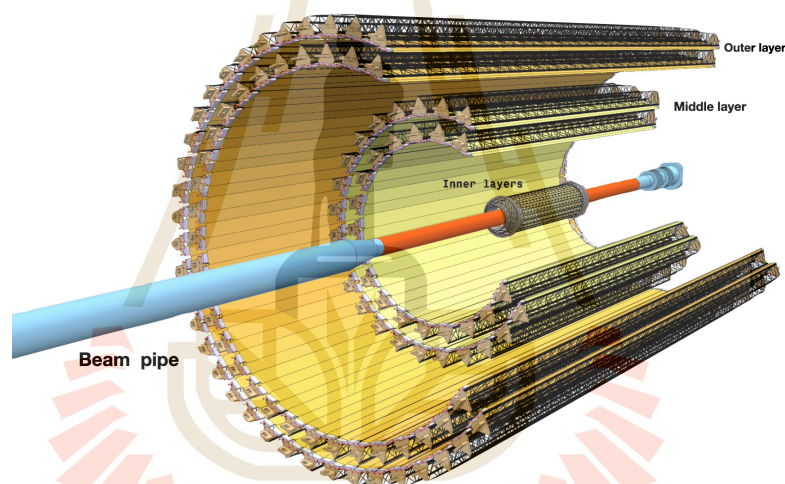


Figure 1.3 ITS2 concept. ITS2 is composed of seven cylindrical silicon detector layers placed coaxially around the beam pipe (Abelev, B., Adam, J., Adamová, D., Aggarwal, M. M., Aglieri Rinella, G., Agnello, M., . . . Zyzak, M., 2014).

The installation of ITS2 in 2021 marked a significant upgrade for ALICE. Figure 1.4 shows the installation of ITS2. It represents a major technological advancement over the previous ITS and is designed to significantly enhance the experiment’s tracking and vertexing capabilities. Extensive commissioning and integration efforts ensured that the new system would interface seamlessly with the rest of the ALICE detector subsystems, such as the Time Projection Chamber (TPC), to provide improved overall tracking performance and data quality for upcoming LHC runs. Table 1.2 provides a

natural grouping of the seven layers in two separate barrels (Inner Barrel and Outer Barrel).

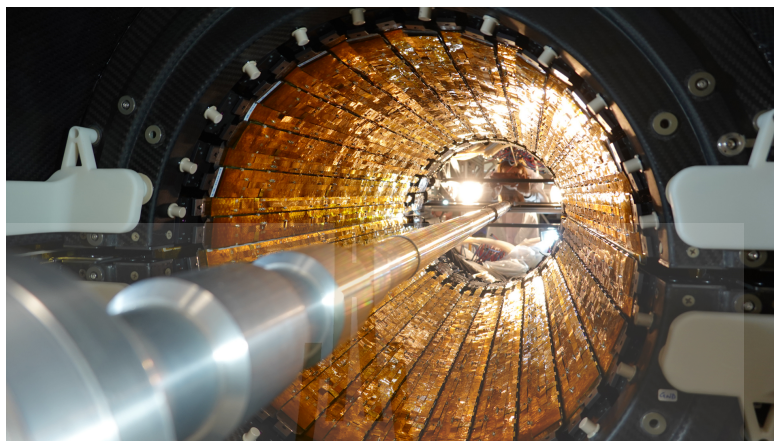


Figure 1.4 ITS2 installation. (collaboration, 2024)

1.2.4 ALICE upgrade plan

ALICE had prepared a significant upgrade of its detector for installation during the second long shutdown (LS2) (Antonioli et al., 2013) (Collaboration, 2015) (Buncic et al., 2015). The goal is to achieve Pb–Pb interaction readout speeds faster than 50 kHz. For particles with low transverse momentum ($p_T < 1$ GeV/c), a new ITS3 was installed to improve vertexing and tracking performance.

ALICE intended to replace new sensors on the ITS2 in order to improve the efficiency of the ITS3 by reducing the material budget of the sensor. This new vertex detector, which will be implemented during LS3, will replace the three innermost layers of the ITS2. The goal is to quantify low transverse momentum charmed hadrons, as well as low mass and low transverse momentum dielectrons by reducing the radius of the innermost layer to 18 mm from the interaction point (Musa, 2019). By reducing layers of different material and changing sensor technology, a material budget of 0.05% X_0 per layer can be achieved. The installation of a new beam pipe with a thinner profile (500 μm) and a lower inner radius (16 mm) is required for the upgrade project. A Monolithic Active Pixel Sensor (MAPS) (Mager, 2016) is the most significant sensor of the ITS upgrade. One new feature of the CMOS image sensor technology, known as stitching, will pave the way for the creation of next-gen large-size MAPS with a surface area of up to 14 x 14 cm^2 .

Table 1.2 The geometrical specifications of the ITS2 (Abelev, B., Adam, J., Adamová, D., Aggarwal, M. M., Aglieri Rinella, G., Agnello, M., . . . Zyzak, M., 2014).

	Inner Barrel			Outer Barrel			
	Inner Layers		2	Middle Layers		Outer Layers	
	0	1		3	4	5	6
Radial position (mm)	22.4	30.1	37.8	194.4	243.9	342.3	391.8
Length (sensitive area) (mm)	271	271	271	843	843	1475	1475
Pseudo-rapidity coverage	± 2.5	± 2.3	± 2.0	± 1.5	± 1.4	± 1.4	± 1.3
Active area (cm ²)	421	562	702	10 483	13 104	32 105	36 691
Pixel sensor dimension (mm ²)				15×30			
Number of pixel sensors / layer	108	144	180	2688	3360	8232	9408
Pixel size (μm^2)	(20–30)×(20–30)			(20–50)×(20–50)			

Beam testing serves as a central method for sensor characterization, wherein an accelerated particle beam is directed through the sensor to evaluate its detection performance under controlled conditions. The Synchrotron Light Research Institute (SLRI) operates an electron beam facility for multiple applications, including the generation of synchrotron radiation and the development of accelerator components. Among its experimental setups, the SLRI Beam Test Facility (SLRI-BTF) is specifically dedicated to the characterization of Monolithic Active Pixel Sensors (MAPS) using a 1.2 GeV electron beam. Additionally, SLRI has collaborated with Suranaree University of Technology (SUT) to investigate sensor performance through systematic studies employing this electron test beam.

1.3 Thesis outline

The introduction provides an overview of the LHC, which is a facility that provides heavy-ion collisions for the purpose of studying the characteristics of matter. The introduction also presents a fundamental description of the Quantum Chromodynamics (QCD), with particular focus on the QCD phase, which is similar to the early stages of the universe. The ALICE experiment, one of nine experiments at the LHC, intends to study the QCD phase by detecting the production of the collision.

The next chapter will cover physics properties of matter, pulsing signal properties, and sensor electronic properties. This chapter also explores the physics properties of the materials used in MAPS, including their interaction with charged particles and their ability to efficiently record particle hits. A discussion on the potential benefits of MAPS in high-energy physics experiments is provided, with a particular emphasis on their application to the ALICE experiment.

In Chapter III, the thesis investigates the parameters of MAPS within the context of the ITS3 upgrade project. The chapter examines the role of MAPS in enhancing the performance of the Inner Tracking System (ITS) at the ALICE experiment, focusing on key aspects such as spatial resolution, detection efficiency, and radiation tolerance. The study includes an analysis of the specific MAPS parameters that need to be optimized to meet the requirements of the ITS3 upgrade and explores the challenges associated with implementing these sensors in a high-radiation environment.

Chapter IV is dedicated to the test beam studies of a pixel sensor telescope. This chapter describes the experimental setup used to evaluate the performance of MAPS in a controlled environment. The test beam analysis focuses on key metrics such as detection efficiency and spatial resolution, providing valuable insights into the performance of MAPS in real-world conditions. The results of the test beam studies are analyzed in detail, and the findings are used to guide the development of more efficient MAPS for particle tracking applications.

Chapter V shifts to the simulation of charge collection in basic MAPS. This chapter discusses the use of computational models to simulate the behavior of charge carriers within MAPS under different conditions. The simulation results provide a deeper understanding of the factors that influence the charge collection process, such as sensor geometry, material properties, and the incident angle of particles. The chapter highlights the importance of simulations in optimizing the design and performance of MAPS and explores how these simulations can be used to predict the behavior of sensors in

experimental settings.

Finally, Chapter VI provides a summary of the findings presented throughout the thesis, offering a comprehensive overview of the research outcomes. The chapter also discusses the implications of the results for the future of MAPS technology, particularly in the context of high-energy physics experiments such as ALICE at the LHC. The conclusion emphasizes the potential for MAPS to revolutionize particle tracking and detection, and outlines directions for future research to further improve their performance and broaden their applications.



CHAPTER II

MONOLITHIC ACTIVE PIXEL SENSOR FUNDAMENTALS

The Monolithic Active Pixel Sensor (MAPS) is an image sensor utilized in vertexing and tracking detector systems for modern high-energy and particle physics. MAPS is a sensor that is based on CMOS technology. Most particle detectors use a silicon sensor for innermost layers such as ATLAS, CMS, LHCb, and ALICE.

This chapter will provide an overview of the silicon sensor. Part one explains particle physics, the interaction of particles. Next, we define the sensor parameters. The characteristics of silicon sensors and the MAPS working concept are also thoroughly explained in this chapter.

2.1 Monolithic Active Pixel Sensor (MAPS)

MAPS is an image sensor that integrates both the read-out circuitry and the silicon sensors into one single silicon substrate. MAPS has been used as part of an upgrade to the inner detector of the Solenoidal Tracker (STAR) at the Relativistic Heavy Ion Collider (RHIC). The advantage of MAPS is a high vertex resolution accuracy (Dorokhov, A., Bertolone, G., Baudot, J., Colledani, C., Claus, G., Degerli, Y., . . . Winter, M., 2011; Schambach, J., Anderssen, E., Contin, G., Greiner, L., Silber, J., Stezelberger, T., . . . Woodmansee, S., 2015; Kittimanapun et al., 2017). ALICE also choose MAPS for an upgrade of their detector. ALice Pixel DETector (ALPIDE) was developed for the ITS2 upgrade project.

2.1.1 Semiconductor Physics

A semiconductor is a material whose electrical conductivity lies between that of a conductor and an insulator. Its conductivity can be significantly enhanced by the introduction of specific donor or acceptor atoms. This process increases the number of free charge carriers—either electrons or holes—depending on the type of atoms introduced. When an additional element is introduced into a base material such as silicon or germanium, the electrical properties of the material change accordingly. This technique is known as doping; it involves the deliberate introduction of impurities into

a semiconductor crystal. These impurities lead to the formation of either N-type or P-type semiconductor materials.

Silicon (symbol Si) is a group IV element with an atomic number of 14. Each silicon atom consists of 14 protons and 14 electrons, arranged into four distinct energy levels. These energy levels are denoted as $1s^2$, $2s^2$, $2p^6$, and $3p^2$, indicating two electrons in the ground state, eight in the second shell, and four in the third shell.

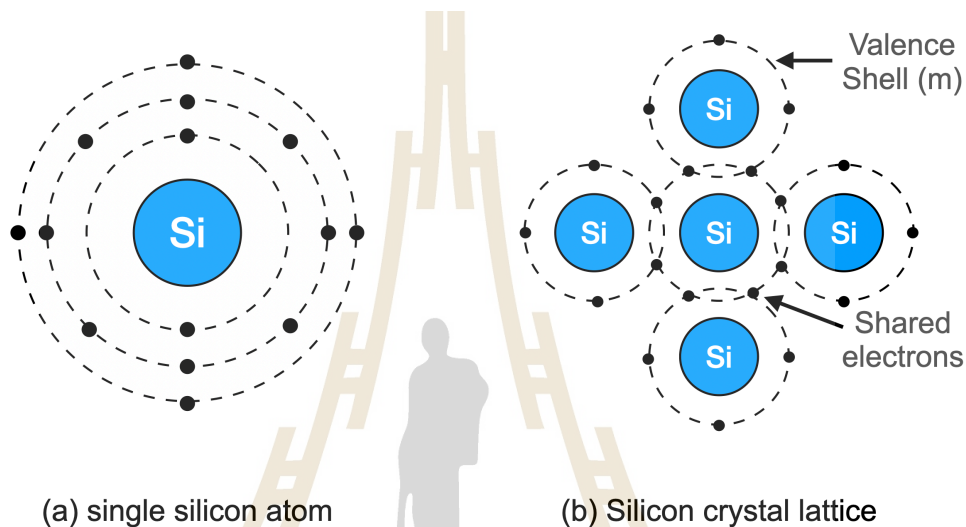


Figure 2.1 Structure and lattice of pure silicon. (a) A single silicon atom with four valence electrons. (b) These electrons form covalent bonds with neighboring atoms, resulting in a crystal lattice structure.

In its pure form, a silicon crystal has limited conductivity. However, by doping it with impurity atoms such as arsenic, antimony, or phosphorus—known as pentavalent elements—its conductivity can be enhanced. These atoms have five valence electrons. When introduced into the silicon lattice, they share four electrons with neighboring silicon atoms, leaving one electron free. This free electron can move easily when an electric voltage is applied, resulting in current flow. Pentavalent atoms are therefore referred to as *donors*, as they donate free electrons. The resulting material is known as N-type silicon.

Alternatively, doping silicon with trivalent atoms such as aluminum, boron, or indium introduces only three valence electrons. These atoms cannot complete the four covalent bonds needed for the silicon lattice, resulting in a deficiency of electrons, or *holes*. These holes behave as positively charged carriers. When an electric field

is applied, holes appear to move through the lattice as electrons fill adjacent gaps. Trivalent atoms are called *acceptors* because they can accept electrons to complete bonding. The resulting material is referred to as P-type silicon.

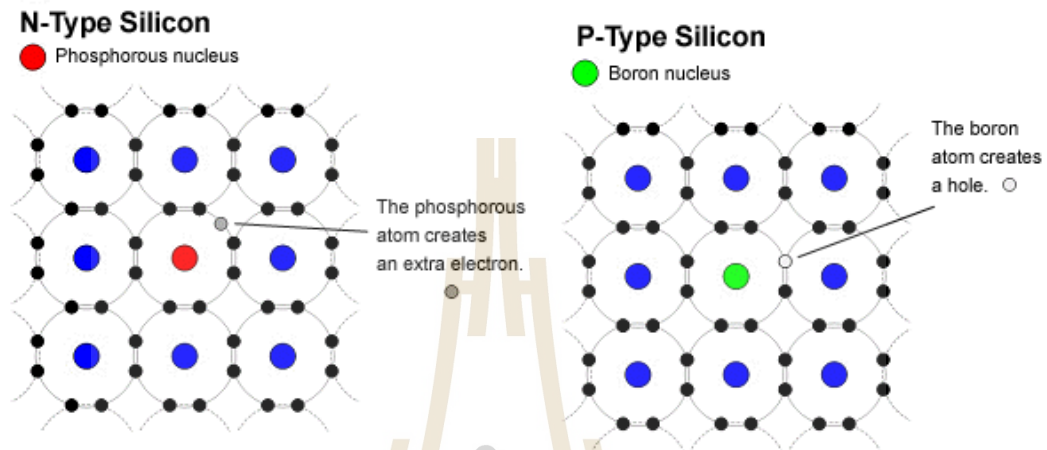


Figure 2.2 The drawing schematic of N-type and P-type atomic structures. (Source: <http://www.answers.com/topic/N-type-silicon-technology>)

2.1.2 Electronic band structure

A crucial concept describes the distribution of energy levels (bands) that electrons can occupy within a semiconductor material. The band structure includes three structures. The conduction band is the energy band with the highest energy level in a semiconductor material. Electrons remain unbound to any specific atom. They can also move freely throughout the material in response to an electric field. The valence band is the highest energy band that contains electrons at absolute zero temperature ($T=0$ K). Electrons tightly bind to their parent atoms in this band. The band gap is the energy difference between the valence band and the conduction band. The gap signifies the energy threshold necessary for the transition of an electron from the valence band to the conduction band.

Applying band theory to impurity-doped semiconductors reveals the introduction of extra energy levels. Electrons in an N-type semiconductor can freely move to the conduction band because their energy levels are close to the top of the band gap. In the P-type case, extra holes in the band gap can help valence band electrons move around, causing holes to move in the valence band (Turchetta, R., Fant, A., Gasiorok, P., Esbrand, C., Griffiths, J.A., Metaxas, M.G., . . . Bergamaschi, A., 2007;

Apadula, N., Armstrong, W., Brau, J., Breidenbach, M., Caputo, R., Carinii, G., . . . Zurek, Z., 2022).

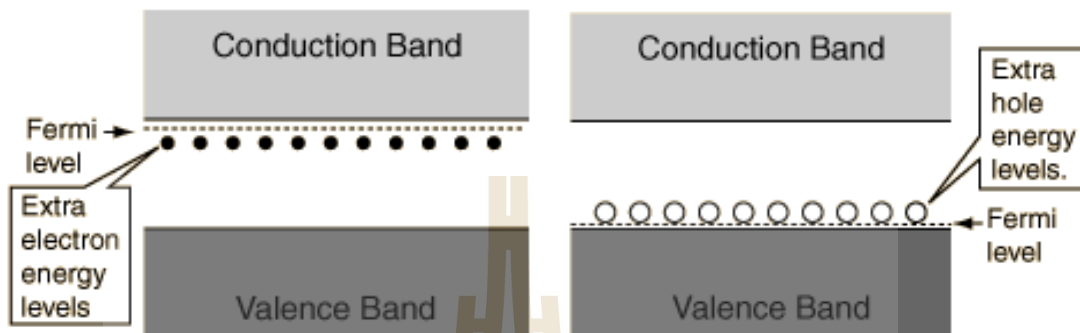


Figure 2.3 The illustration of N-type (left) and P-type (right) doped semiconductor band structures. (Source: <http://hyperphysics.phy-astr.gsu.edu>)

2.1.3 P-N Junction

When a P-type and an N-type semiconductor are brought into contact, they form a P-N junction. At the interface, a thin region known as the *depletion region* is created. This region is depleted of mobile charge carriers because electrons from the N-side and holes from the P-side diffuse across the junction and recombine. As a result, immobile ionized donor and acceptor atoms are left behind, creating an internal electric field that opposes further diffusion. The depletion zone behaves like an insulator, forming a potential barrier to current flow. The width of the depletion region depends on both the doping concentrations and the external voltage applied to the junction.

Figure 2.4 shows the charge distribution at the P-N junction. To maintain overall charge neutrality across the junction, the charge on each side must be equal and opposite. This equilibrium condition is expressed as:

$$D_p N_A = D_n N_D, \quad (2.1)$$

where D_p and D_n represent the depletion widths on the P-type and N-type sides, respectively, and N_A and N_D are the corresponding doping concentrations.

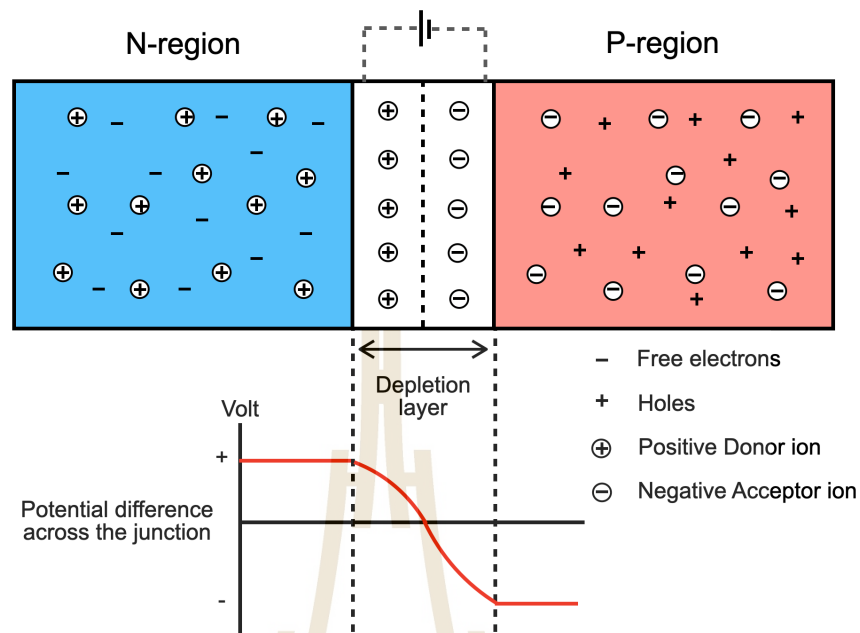


Figure 2.4 Potential difference across the junction between P-type and N-type semiconductors. The P-N junction is formed upon contact between the two materials.

2.1.4 Electric Field in the Depletion Region

The fixed charges left behind in the depletion region generate an internal electric field that points from the positively charged N-side to the negatively charged P-side. This electric field forms a built-in potential across the junction, which prevents further diffusion of charge carriers.

The built-in voltage under thermal equilibrium conditions is given by:

$$\mathcal{E}_0 = v_T \ln \left(\frac{N_D N_A}{n_i^2} \right), \quad (2.2)$$

where \mathcal{E}_0 is the built-in potential, v_T is the thermal voltage, N_D and N_A are the donor and acceptor concentrations, respectively, and n_i is the intrinsic carrier concentration of the semiconductor.

2.1.5 Effect of Magnetic Field

The presence of a magnetic field alters the behavior of charge carriers within the semiconductor. As electrons or holes move under an electric field, they are influ-

enced by the Lorentz force due to the magnetic field. This force causes their trajectories to deviate, which is especially important in sensor applications exposed to magnetic environments.

The Lorentz force acting on a charged particle is expressed as:

$$\mathbf{F} = \pm e (\mathbf{E} + \mathbf{v} \times \mathbf{B}), \quad (2.3)$$

where e is the elementary charge, \mathbf{E} is the electric field, \mathbf{v} is the drift velocity, and \mathbf{B} is the magnetic field.

This deflection results in a deviation angle known as the *Lorentz angle*, θ_L , defined as:

$$\tan \theta_{L,n} = \mu_{\text{Hall},n} \beta_{\perp} \cdot x_s \quad \text{and} \quad \tan \theta_{L,p} = \mu_{\text{Hall},p} \beta_{\perp}, \quad (2.4)$$

where β_{\perp} is the component of the magnetic field perpendicular to the drift direction, and μ_{Hall} is the Hall mobility, which differs from drift mobility and reflects the magnetic influence on charge transport.

2.1.6 Reverse Bias in a P-N Junction

When an external voltage is applied in the same direction as the built-in potential (i.e., reverse bias), it widens the depletion region and strengthens the internal electric field. This configuration is widely used in semiconductor detectors to reduce thermal noise and enhance signal resolution.

The total width W of the depletion region under reverse bias is determined using the Poisson equation and is given by:

$$W = x_n + x_p = \sqrt{\frac{2\epsilon_0\epsilon_{\text{Si}}}{e} \left(\frac{1}{N_A} + \frac{1}{N_D} \right) (V + V_{\text{bi}})}, \quad (2.5)$$

where x_n and x_p are the depletion widths on the N-side and P-side, respectively, ϵ_0 is the vacuum permittivity, ϵ_{Si} is the relative permittivity of silicon, e is the elementary charge, N_A and N_D are the doping concentrations, V_{bi} is the built-in voltage, and V is the applied reverse voltage.

2.1.7 Operation principles of MAPS

The MAPS commonly employed in high-energy physics experiments comprise three distinct levels, as depicted in Figure 2.5. A very p-doped (P++) base supports a very thin (P- epitaxial layer) that is used as a sensitive volume. N-type and P-type implants, also known as wells, sit on top of the epitaxial layer. N-type implants act as collecting diodes and collect a signal. P-wells host the circuitry. In addition to the implants, the in-pixel circuitry is composed of metal layers. Modern MAPS are typically manufactured using a high-resistivity epitaxial layer with a resistivity of $\rho > 1 \text{ k}\Omega \text{ cm}$. The composition of MAPS consists:

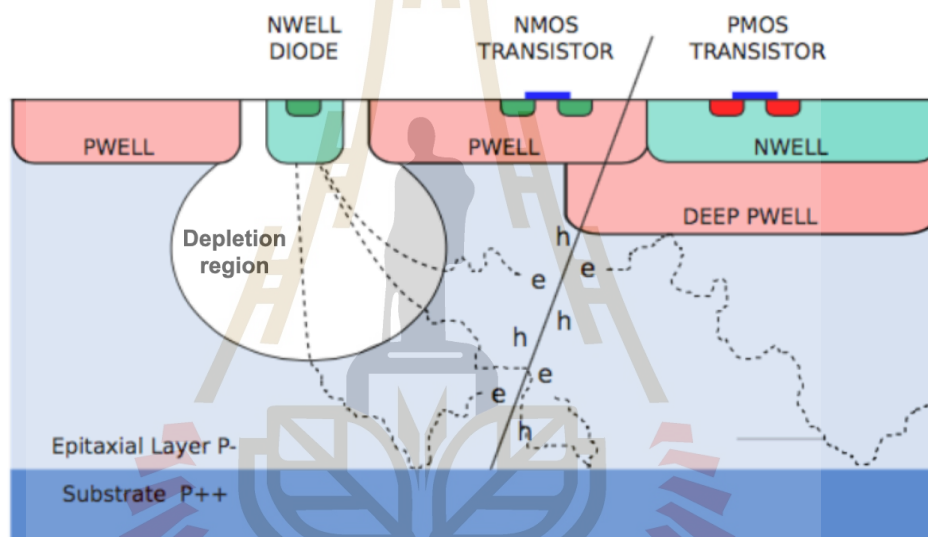


Figure 2.5 A drawing cross section of a MAPS pixel (not scale) (Abelev, B., Adam, J., Adamová, D., Aggarwal, M. M., Aglieri Rinella, G., Agnello, M., . . . Zyzak, M., 2014).

- A SiO_2 layer is a top layer of the sensor. Electronic circuits is located on this layer. The electronic circuits consist of gates and drains, together with a passivation layer designed to prevent damage to the sensor's surface.
- An epitaxial layer is a middle layer. The epitaxial layer creates a depletion region underneath the n-well diode layer. Electron-hole pairs will form after charged particles pass through the sensor. The electric field inside the depletion region will diffuse the generated electrons to the collection diode. Furthermore, applying a reverse bias to the sensor creates an expanded depletion region.

- The substrate is a silicon layer with a high concentration of p-doping (P++) situated at the lower part of the sensor. The built-in voltage will reflect the generated electrons at the junction between the substrate and epitaxial layer. The primary purpose of the substrate is to prevent the diffusion of electrons outside the pixel.

2.2 Silicon properties of MAPS

The interaction of charged particles with matter is a fundamental aspect of particle detection in MAPS. When charged particles pass through silicon, they lose energy through various processes such as ionization, electromagnetic interactions, and bremsstrahlung. These interactions directly affect the sensor's ability to detect and track particles with high precision. Understanding these interactions is crucial for optimizing the design and functionality of MAPS in high-energy physics experiments.

2.2.1 Interaction of Charged Particles with Matter

The performance of Monolithic Active Pixel Sensors (MAPS) relies heavily on how charged particles interact with silicon. These interactions determine the fundamental signal generation mechanisms within the detector. When a charged particle traverses a silicon layer, it transfers energy to the medium via several physical processes, primarily ionization, excitation, bremsstrahlung, and Cherenkov radiation. These mechanisms are crucial in generating measurable charge carriers—electrons and holes—that are ultimately collected and processed by the MAPS electronics.

In high-energy physics applications, understanding the detailed nature of these interactions is essential for designing highly sensitive detectors capable of precise spatial and temporal resolution. The interaction cross-sections, energy loss profiles, and secondary particle production all influence the signal quality, detection efficiency, and spatial resolution of MAPS devices. The following subsections provide a detailed explanation of the main mechanisms through which energy is deposited in silicon by charged particles.

2.2.2 Ionization and Excitation

Ionization and excitation (Bartschat, 1989; Essig et al., 2024) are fundamental processes by which charged particles lose energy as they traverse matter. These processes involve energy transfer to atoms or molecules in the medium, leading to the

removal or excitation of electrons.

When charged particles such as alpha or beta particles pass close to atoms, they can exert forces strong enough to remove one or more electrons. If the particle's energy exceeds the electron's binding energy, it can ionize the atom by releasing an electron from its orbital, transforming the neutral atom into an ion pair. The ejected electron is called a *secondary electron*, typically having an energy below 100 eV. This process reduces the particle's kinetic energy and slows its motion. Figure 2.6 illustrates ionization caused by an incoming alpha particle, resulting in a positively charged ion and a liberated electron (sometimes called a *delta ray* if it has sufficient energy to induce further ionization).

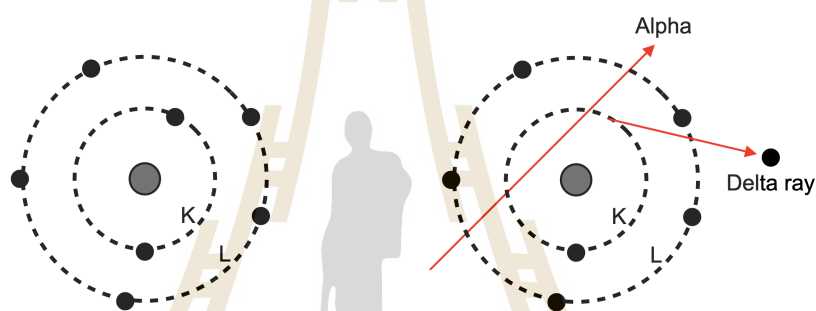


Figure 2.6 Ionization caused by a charged particle. A secondary electron with sufficient kinetic energy to induce further ionization is known as a delta ray. Secondary electrons represent the negative half of an ion pair.

In addition to ionization, charged particles can also excite atoms. In this case, an electron is elevated to a higher energy level but is not ejected from the atom. This process, known as *excitation*, typically occurs further from the particle's trajectory than ionization. The excited atom eventually returns to its ground state through de-excitation, emitting a photon in the process. This mechanism is illustrated in Figure 2.7.

2.2.3 Bremsstrahlung Radiation

Bremsstrahlung or “braking radiation” (Jakubassa-Amundsen, 2021), occurs when high-energy charged particles are decelerated by the electric fields of atomic nuclei. This interaction results in the emission of electromagnetic radiation in the form of photons. Electrons (beta particles) are particularly prone to this effect due to their low mass and ease of deflection.

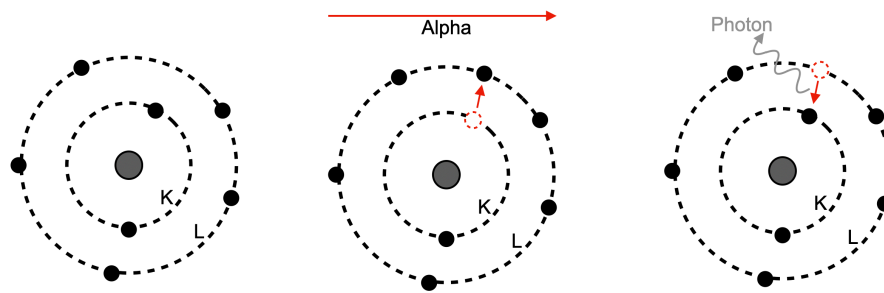


Figure 2.7 Excitation by a charged particle. An electron is raised from the K-shell to the L-shell. Upon returning to a lower energy state, a photon is emitted.

Bremsstrahlung is especially significant under two conditions: when the charged particle has high energy and when it passes through materials with high atomic numbers. For example, P-32 beta particles can produce bremsstrahlung photons with energies up to 1.7 MeV.

The energy loss due to bremsstrahlung is described by:

$$E = \frac{dE}{dx} = \frac{e^2}{4\pi\epsilon_0} \frac{1}{\beta^2} \left[\frac{1 - \beta^2}{2} \ln \frac{1 + \beta}{1 - \beta} - \beta \right], \quad (2.6)$$

where:

- E is the emitted radiation energy,
- $\frac{dE}{dx}$ is the energy loss per unit path length,
- e is the elementary charge,
- ϵ_0 is the vacuum permittivity,
- β is the particle's velocity relative to the speed of light.

This equation quantifies the energy lost through bremsstrahlung as a function of the particle's speed and the medium's properties.

2.2.4 Cherenkov Radiation

Cherenkov radiation arises when a charged particle moves through a dielectric medium at a speed greater than the phase velocity of light in that medium. This

causes transient polarization of nearby atoms, which, upon returning to equilibrium, emit coherent electromagnetic radiation along a conical path (Carnesecchi, F., Sabiu, B., Strazzi, S., Vignola, G., Agrawal, N., Alici, A., . . . Zichichi, A., 2023).

The coherent emission leads to a characteristic blue glow, commonly observed in nuclear reactors submerged in water. The intensity and distribution of this radiation are given by the Frank–Tamm formula:

$$\frac{dN}{d\lambda dx} = \frac{2\pi\alpha z^2}{\lambda^2} \left[1 - \frac{1}{\beta^2 n^2(\lambda)} \right], \quad (2.7)$$

where:

- α is the fine-structure constant,
- z is the charge of the particle,
- λ is the wavelength of the emitted radiation,
- β is the velocity of the particle relative to the speed of light,
- $n(\lambda)$ is the refractive index of the medium as a function of wavelength.

This equation describes the number of Cherenkov photons emitted per unit wavelength per unit path length of the particle.

2.2.5 Bethe–Bloch Formula for Stopping Power

The Bethe–Bloch formula describes the average energy loss per unit path length (dE/dx) of a charged particle as it travels through matter. This energy loss, known as the *stopping power*, results from inelastic collisions between the charged particle and atomic electrons (Medenwaldt, R., Møller, S.P., Uggerhøj, E., Worm, T., Hvelplund, P., Knudsen, H., . . . Morenzoni, E., 1991; Salvat, 2022).

$$\frac{dE}{dx} = K z^2 \frac{Z}{A} \frac{1}{\beta} \left[\frac{1}{2} \frac{2m_e c^2 \beta^2 \gamma^2 T_{\max}}{I^2} - \beta^2 - \frac{\delta(\beta\gamma)}{2} \right], \quad (2.8)$$

where:

- dE/dx is the average rate of energy loss of the charged particle per unit path length (MeV/cm),
- K is a constant ($0.307 \text{ MeVcm}^2/\text{g}$ for Si),
- z is the charge of the particle,
- Z is the atomic number of the material,
- A is the atomic mass of the material (in g/mol),
- γ is the Lorentz factor ($\gamma = \frac{1}{\sqrt{1-\beta^2}}$),
- m_e is the rest mass of the electron (in MeV/c^2),
- c is the speed of light in vacuum (in cm/s),
- β is the velocity of the particle relative to the speed of light in vacuum,
- T_{max} is the maximum kinetic energy that can be transferred to an electron in a single collision (in eV),
- I is the mean excitation energy of the material, the average energy required to create an electron-hole pair (in eV).

Equation 2.8 describes the energy loss of charged particles as they move through a material, resulting from their interactions with the electrons within the material. The term $(1/\beta)$ accounts for the relativistic effects when the particle travels at speeds close to the speed of light. The natural logarithmic term $\ln\left[\frac{(2m_e c^2 \beta^2)}{(I_2)}\right]$ represents the energy lost through collisions with the material's electrons.

2.3 Radiation damage

Radiation damage in terms of semiconductors refers to the degradation of semiconductor material and devices caused by exposure to ionizing radiation such as high-energy particles or electromagnetic radiation. LHC produces intense beams of charged particles, secondary particles including neutrons, gamma rays, etc. Those particles can interact with materials and electronic devices, leading to various forms of radiation damage.

2.3.1 Non-ionizing radiation damage

Charged particles lose energy as they pass through a material without causing ionization, a phenomenon known as non-ionizing energy loss (NIEL). Charged particles dissipate NIEL as they interact with the silicon lattice through processes like phonon scattering and displacement damage. Charged particles can cause atoms in the silicon lattice to move from their original locations. Displacement damage can result in the formation of defects and vacancies within the crystal structure of the silicon detector. NIEL is usually expressed as an equivalent to NIEL of 1 MeV neutrons per square centimetre ($1 \text{ MeVn}_{\text{eq}}\text{cm}^{-2}$).

$$\text{NIEL}(E) = \frac{N_A}{A} \sum_i \int_{E_{\min}}^{E_{\max}} Q(E) E \left(\frac{d\sigma}{dT} \right)_i dE, \quad (2.9)$$

where

- E_0 is the energy of incident particle,
- T is the the energy transferred to the recoil atom,
- $(d\sigma/dE)$ is the differential partial cross section for a particle with energy T_0 to create a recoil atom with energy T in the i -th reaction,
- $Q(E)$ is a partition factor giving the fraction of T that going into further displacements,
- N_A is an Avogadro number,
- A is an atomic mass of target atom.

2.3.2 Ionizing radiation damage

Ionizing radiation can interact with materials and electronic devices by knocking electrons out of their atomic orbits, creating electron-hole pairs. This process can lead to the formation of defects in the crystal lattice of materials and alter the electrical properties of semiconductors and insulators.

Total Ionizing Dose (TID) refers to the particles that deposit the ionization dose when they pass through the materials that make up electronics. TID is a way to estimate the amount of energy, or dosage, that radiation, in its ionization state, deposits into a

substance. Although the TID unit is Gray, Rad, which is the old unit of the radiation effects community, is still commonly used (1 Gray = 100 rad). Displacement damage can be expressed in terms of the particle fluence (particles/cm²). The TID absorbed by the silicon detector can be quantified using the equation:

$$\text{TID} = \int_0^t \Phi(E, t) \times dt, \quad (2.10)$$

where

- TID is the total ionizing dose absorbed by the devices (in Gray),
- $\Phi(E, t)$ is the flux of ionizing radiation as a function of energy (E) and time (t),
- dt represents an infinitesimal time interval over which the ionizing radiation flux is integrated.

2.4 Coulomb Scattering of Particles in Matter

As charged particles traverse a medium, they experience interactions with both the electrons and the nuclei of atoms. While inelastic collisions with atomic electrons lead to ionization and excitation, elastic Coulomb scattering with nuclei causes deflections in the trajectory of the particles. This elastic scattering is a crucial process in particle tracking and detector resolution, particularly for materials like silicon used in Monolithic Active Pixel Sensors (MAPS). Figure 2.8 illustrates the concept of multiple Coulomb scattering occurring within a medium.

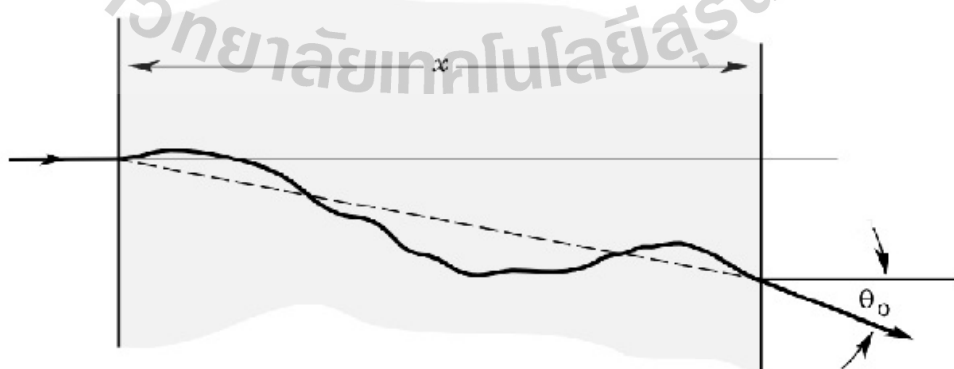


Figure 2.8 Layout of multiple Coulomb scattering of charged particles (Meroli, 2015).

Coulomb scattering is typically categorized into three regimes, depending on the material thickness and the number of scattering events: single scattering, plural scattering, and multiple scattering. Each regime affects the angular distribution and trajectory of particles in distinct ways, which must be considered for accurate simulation and detector design.

2.4.1 Single Scattering

Single scattering occurs when the thickness of the material is extremely small, such that the probability of more than one scattering event is negligible. In this regime, the angular deflection of the particle can be accurately described by the classical Rutherford scattering formula:

$$\frac{d\sigma}{d\Omega} = \left(\frac{Z_1 Z_2 e^2}{16\pi\epsilon_0 E} \right)^2 \frac{1}{\sin^4\left(\frac{\theta}{2}\right)}, \quad (2.11)$$

where:

- Z_1 and Z_2 are the atomic numbers of the incident particle and the target nucleus, respectively,
- e is the elementary charge,
- ϵ_0 is the vacuum permittivity,
- E is the kinetic energy of the incident particle,
- θ is the scattering angle in the laboratory frame.

This formula describes the differential cross-section for scattering and reveals that large-angle deflections are significantly less probable than small-angle ones. The Rutherford scattering model is essential for understanding isolated, high-energy collisions with atomic nuclei.

2.4.2 Plural Scattering

Plural scattering represents an intermediate regime where the particle undergoes a small number of (typically between 2 and 10) elastic scatterings as it traverses a thin layer of material. In this regime, the superposition of individual scattering angles

cannot yet be approximated as a Gaussian distribution, as in multiple scattering, but the interactions are also no longer independent as in the single-scattering case.

Theoretical treatments of plural scattering are more complex and often rely on numerical methods or Monte Carlo simulations to estimate the angular distributions. This regime is especially relevant in thin detector layers where spatial resolution is critical, and small cumulative deviations can significantly affect tracking performance (Meroli, 2015).

2.4.3 Multiple Scattering

When a charged particle passes through a thicker material, it experiences many small-angle deflections due to repeated Coulomb interactions with nuclei. This is the regime of multiple scattering, where the net angular deviation follows an approximately Gaussian distribution centered around the initial direction of motion.

The root mean square (RMS) projection of the angular distribution, denoted as θ_0 , is given by the Highland formula:

$$\theta_0 = \frac{13.6 \text{ MeV}}{\beta_{cp}} \cdot z \cdot \sqrt{\frac{x}{X_0}} \left[1 + 0.038 \ln \left(\frac{x}{X_0} \right) \right], \quad (2.12)$$

where:

- θ_0 is the RMS scattering angle (projected in one plane),
- z is the charge number of the incident particle,
- β is the velocity of the particle relative to the speed of light,
- p is the momentum of the particle,
- x is the thickness of the material traversed,
- X_0 is the radiation length of the material.

The radiation length X_0 is a material-dependent property that characterizes the mean distance over which a high-energy electron loses all but $1/e$ of its energy via bremsstrahlung, and it also serves as a scaling parameter in multiple scattering. It can be approximated by:

$$X_0 = \frac{716.4 \cdot A}{z(z + 1) \ln(287/\sqrt{z})}, \quad (2.13)$$

where:

- Z is the atomic number of the scattering material,
- A is the atomic mass number of the material.

Understanding multiple scattering is critical for reconstructing particle trajectories in high-energy physics experiments, as it directly impacts the resolution of position-sensitive detectors like MAPS. In practice, the cumulative scattering angle is used in detector simulations to model the spread of the particle track and optimize sensor design and placement.

2.5 Properties of MAPS

Detection efficiency and spatial resolution are the main characteristics for the test beam measurement. Some parameters can be offered to help with the function of sensors. In this section, the key parameters will be shown.

2.5.1 Detection efficiency

The detection efficiency of a tested sensor is expressed as the ratio of related hits to all particle tracks and all particle tracks.

$$\text{Detection efficiency} = \frac{\text{An associated tracks with hit on DUT}}{\text{All tracks on DUT}}. \quad (2.14)$$

The detection efficiency for tracking particles must be more than 99% for the ITS upgrade project. The ratio of tracks hitting on DUT to all tracks on DUT is taken into account while calculating detection efficiency.

2.5.2 Spatial resolution

The spatial resolution is found by calculating the variance of the residual spatial resolution distribution σ_{res} , which is made up of the discrepancies between the

reconstructed hit position and the extrapolated track intersection point at the DUT. The spatial resolution is given by

$$\sigma^2 = \sigma_{\text{res}}^2 - \sigma_{\text{track}}^2, \quad (2.15)$$

where the track resolution σ_{track} depends on the inherent resolution of the tracking planes as well as physical uncertainties such as multiple scattering, and is consequently dependent on the experimental setup.

2.5.3 Charge threshold

The in-pixel discriminator charge threshold is set by three front-end biasing parameters: I_{THR} , V_{CASN} , and I_{DB} . The measurement is done by sending N_{inj} times a range of test charges Q_{inj} through a pulsing capacitance C_{inj} so that

$$Q_{\text{inj}} = C_{\text{inj}}(V_{\text{PLSE}}) \quad (2.16)$$

The charge threshold is defined by I_{THR} , V_{CASN} , and I_{DB} . Increasing the charge threshold can be done by adjusting I_{THR} or I_{DB} . On the other hand, reducing the threshold can be achieved by augmenting V_{CASN} .

2.5.4 Fake-hit rate

Fake-hit rate (FHR) is determined by the number of particle collisions that take place on a per-pixel basis during each event that is unaffected by outside influence. This also evaluates the amount of background noise produced by the detector.

FHR is assessed by delivering a number of triggers (N_{trg}) to the chip without providing any external stimulation and measuring the number of hits N_{hit} .

$$\text{FHR}_{\text{meas}} = \frac{N_{\text{hit}}}{N_{\text{pix}}N_{\text{trg}}} \quad (2.17)$$

where N_{pix} is the number of pixels in the sensor.

2.5.5 Noise

The noise signal depends upon several factors, including sensor type, geometry, biasing, and readout. Noise is generally expressed as Equivalent Noise Charge (ENC), which corresponds to the noise at the amplifier's input in terms of elementary charges.

The noise contributions include detector capacitance (ENC_C), leakage current (ENC_I), detector parallel resistor (ENC_{R_p}), and detector series resistor (ENC_{R_s}). The overall noise is the quadratic sum of all contributions as the equation:

$$ENC = \sqrt{ENC_C^2 + ENC_I^2 + ENC_{R_p}^2 + ENC_{R_s}^2} \quad (2.18)$$

Detector capacitance (ENC_C) is an input of a charge-sensitive amplifier that typically serves as the primary noise source within the detector system.

$$ENC_C = a + b \cdot C, \quad (2.19)$$

where the preamplifier design determines a and b , and C is the detector capacitance at the channel's input. The ENC_C is dependent on the integration time t_p ; a short integration time can lead to higher a and b values. The integration time depends on the accelerator time structure.

Leakage current (ENC_I) is a leakage current in the detector that arises from electron-hole pairs generated thermally within the depletion region. These pairs are separated by the electric field, which causes the leakage current. The fluctuations in this leakage current contribute to the noise. For an amplifier with an integration time t_p followed by a CR-RC filter, the noise contribution due to the leakage current, denoted as I , can be expressed as

$$ENC_I = \frac{e}{2} \sqrt{\frac{I t_p}{E}}, \quad (2.20)$$

where e represents the Euler number (2.718) and E is the electron charge.

Parallel resistor (ENC_{R_p}) is a bias resistor represented by the parallel resistor R_p in the alternative circuit diagram. The noise component may be articulated as

$$ENC_{R_p} = \frac{e}{E} \sqrt{\frac{kT t_p}{2R_p}}. \quad (2.21)$$

The parallel resistor (ENC_I) is an electric field that separates pairs of electrons and holes created by heat in the depletion zone. This separation leads to current leakage in the detector. Variations in the leakage current cause background noise. If we take an amplifier with an integration time t_p and then a CR-RC filter, we can express

the noise contribution from the leaking current as the parallel resistor (ENC_{R_p}) is a bias resistor that can be shown by the parallel resistor R_p in the alternative circuit schematic. We may express the noise term as

$$ENC_I = \frac{e}{2} \sqrt{\frac{It_p}{e}}. \quad (2.22)$$

Parallel resistor (ENC_{R_s}) is a resistance of the connection between the sensors and the amplifier input that determines the series resistor R_s in the alternative circuit layout. R_s can be expressed as the following equation:

$$ENC_{R_s} = 0.395C \sqrt{\frac{R_s}{t_p}}, \quad (2.23)$$

where C is the detector capacitance in pF, t_p is the integration time in μs , and R_s is the series resistor in Ω .

2.5.6 Charge collection efficiency

Charge Collection Efficiency (CCE) is a fundamental parameter characterizing the performance of semiconductor pixel sensors. It quantifies the proportion of charge generated by incident radiation that is subsequently collected by the sensor electrodes. Precise determination of CCE is crucial, particularly for evaluating radiation damage and optimizing sensor designs for particle physics and radiation detection applications.

$$\eta = \frac{Q_{\text{collected}}}{Q_{\text{generated,max}}}, \quad (2.24)$$

where $Q_{\text{collected}}$ represents the total charge collected by the sensor, and $Q_{\text{generated,max}}$ denotes the theoretical maximum charge generated. The CCE for the entire active volume is approximately 100% for a totally depleted detector with a strong electric field. Charge recombination may result in the CCE being less than 100% in detector areas with a lower electric field.

In practical measurement contexts, particularly when analyzing pixel sensors, another operational definition is often used:

$$\text{CCE (\%)} = 100 \times \frac{Q_{\text{matrix}}}{Q_{\text{seed}}}. \quad (2.25)$$

Here, Q_{matrix} denotes the total collected charge within a pixel cluster (matrix), and Q_{seed} refers specifically to the pixel with the highest individual charge (seed pixel). This definition is useful for evaluating how charges spread across multiple pixels within the sensor, which is crucial for position-sensitive particle detectors. However, due to this definition, the calculated CCE can exceed 100%, since the matrix charge aggregates signals from multiple pixels, while the seed signal represents only one pixel.

2.5.7 Other sensor parameters

There are some variables that determine the amount of the MAPS charge collected. The subsequent section provides a summary of the typical variables utilized in the next chapter for analyzing MAPS responses.

- A cluster refers to a group of adjacent pixels that have collected a charge exceeding a certain threshold.
 - For analog sensors, this threshold is set during data analysis and applies uniformly across all pixels (in this work, the threshold is $100 e^-$ unless specified otherwise).
 - For binary sensors, the threshold is applied online during data acquisition, with the comparator being either on-chip or in-pixel, and it varies from pixel to pixel.
- Cluster size (or multiplicity) is the total number of pixels within a cluster.
- Cluster shape is a numerical identifier assigned to each unique cluster configuration.
- Center of mass of a cluster is defined as:

$$(x_{\text{CM}}, y_{\text{CM}}) = \frac{\sum_i s_i(x_i, y_i)}{\sum_i s_i} \quad (2.26)$$

where x_i and y_i represent the positions of the i -th pixel in the cluster, and s_i is the signal of the i -th pixel (for binary sensors, $s_i = 1$).

- The seed pixel is the pixel within a cluster that has accumulated the largest charge.

- The seed signal is the amount of charge collected by the seed pixel.
- The cluster signal is the total charge collected by all pixels in the cluster.
- The matrix signal is the sum of the charges collected by all pixels in an $N \times N$ matrix centered on the seed pixel. Unlike the cluster signal, the matrix signal includes charge contributions from pixels with signals below the threshold. However, it also incorporates noise from all $N \times N$ pixels.

2.5.8 Conclusion

In this chapter, the fundamental concepts underlying Monolithic Active Pixel Sensors (MAPS) have been presented, with emphasis on the semiconductor physics relevant to their operation, including doping, band structure, and the P–N junction. The interactions of charged particles with matter—such as ionization, excitation, bremsstrahlung, Cherenkov radiation, and Coulomb scattering—were described, as well as the effects of radiation damage on silicon sensors. Key performance parameters of MAPS, including detection efficiency, spatial resolution, charge threshold, fake-hit rate, noise, and charge collection efficiency, were also introduced. These physical principles and performance metrics provide the foundation for understanding MAPS behavior in particle detection. In the following chapter, the focus will shift to the specific implementation of MAPS in the ALICE ITS3 upgrade, including the sensor architecture, laboratory characterization, and performance evaluation under various operating conditions.

CHAPTER III

THE STUDY OF MAPS PARAMETERS FOR ITS3

In this chapter, the implementation and evaluation of Monolithic Active Pixel Sensors (MAPS) for the ALICE Inner Tracking System 3 (ITS3) upgrade are presented. The chapter begins by outlining the ITS3 design concept, including the material budget considerations and the motivation for reducing non-sensitive components to achieve minimal material thickness. The architecture of the prototype chips, such as the Analog Pixel Test Structure (APTS), Digital Pixel Test Structure (DPTS), and Circuit Exploratoire 65 nm (CE65), is then described, highlighting their design features and intended functions. Laboratory test setups and measurement procedures are detailed, followed by performance characterization using pulsing tests, threshold optimization, and radioactive source measurements. Additional studies investigate the effects of operating temperature and radiation exposure on sensor behavior. The results provide a comprehensive assessment of sensor performance under different conditions, serving as a basis for further optimization of the ITS3 detector design.

3.1 Inner Tracking System concept

The material budget breakdown of the Inner Tracking System 2 (ITS2) clearly shows that the silicon sensor contributes only a small fraction of the total material. The sensor thickness is $50 \mu\text{m}$, and ideally, as the only required component for the detector array, it contributes just 15% of the total. The remainder is attributed to the material of the electrical substrate (FPC), which constitutes the largest contribution (50%) including passive components and glue, to the cooling circuit (20%) and to the carbon spaceframe (15%). To achieve the lower material budget, the cooling part will be removed, with a possible power consumption lower than $20 \text{ mW}/\text{cm}^2$. The circuit board (power and data) will be removed as it may be integrated onboard. The mechanical support will also be removed. With all removals, the remaining material budget can reach 0.05% (see Figure 3.1). A new vertex detector is being constructed for the ITS upgrade (Collaboration, 2018). The ITS3 will have two distinct barrels. The outer ITS3 barrel will be identical to the outermost four ITS2 layers (Layers 3 through

6). The current Inner Barrel (IB) of the ITS2 will be replaced with a new IB consisting of two halves. Each half-barrel will consist of three half-layers. Each half-layer along the longitudinal axis (at $z = 0$) is subdivided into quarter-layers, giving the half-barrel a fully half-cylindrical shape. Each quarter-layer comprises a single large pixel chip that is cylindrical shaped (see Figure 3.2). Stitching is a relatively new feature of the CMOS imaging sensor technology. This method can produce sensors of any size, even a complete stave. The specific parameters for ITS3 are shown in Table 3.1.

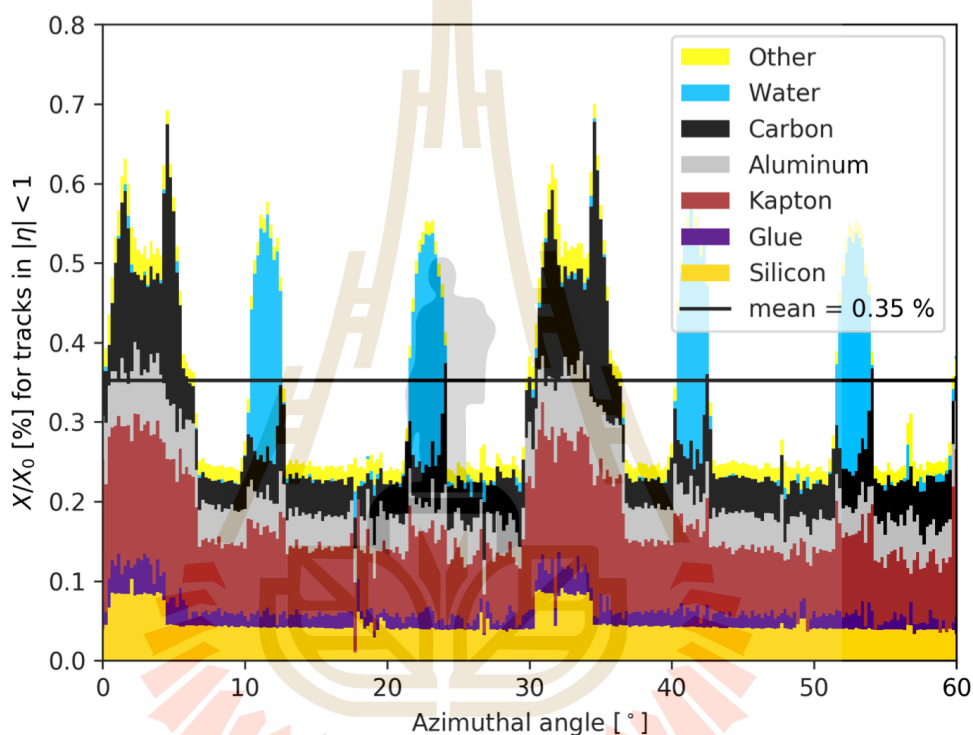


Figure 3.1 Distribution of the material budget of all components of ITS2 (collaboration, 2024).

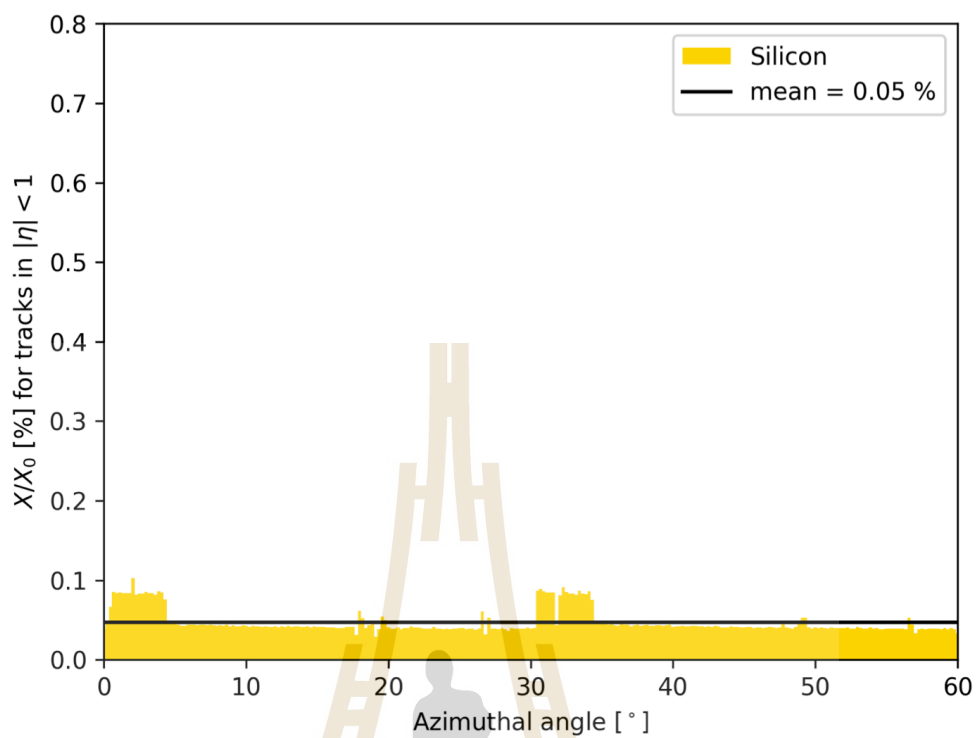


Figure 3.2 Distribution of the material budget of all components of ITS3 (collaboration, 2024).

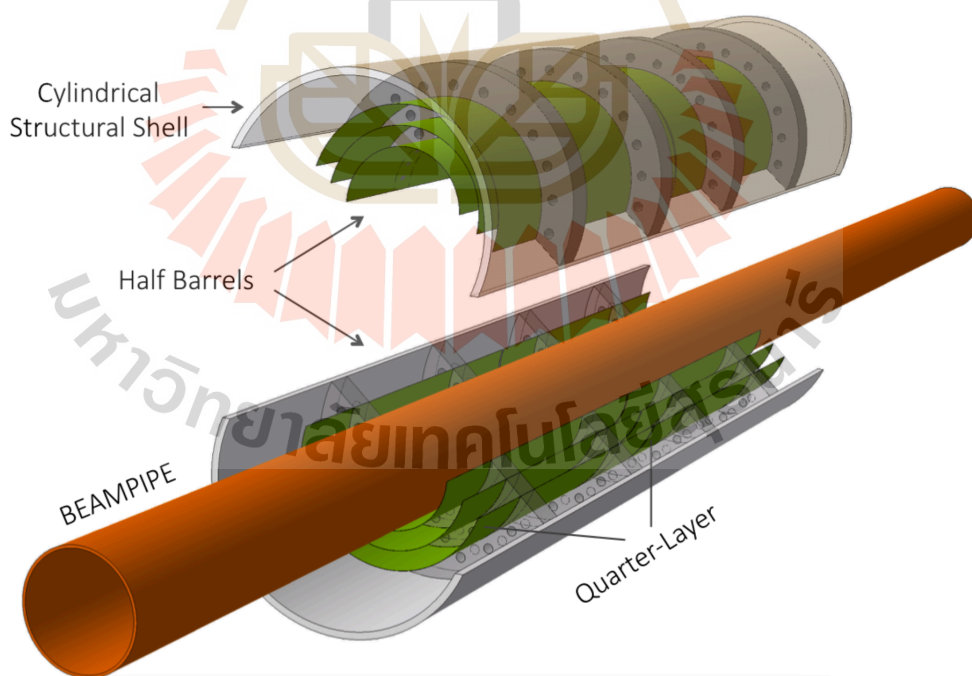


Figure 3.3 Layout of the ITS3 Inner Barrel (collaboration, 2024).

Table 3.1 Geometrical specifications of ITS3.

Beam pipe inner/outer radius (mm)	16.0/16.5		
IB layer parameters	Layer 0	Layer 1	Layer 2
Radial position (mm)	18.0	24.0	30.0
Length (sensitive area) (mm)	270	270	270
Pseudo-rapidity coverage	2.5	2.3	2.0
Active area (cm ²)	305	408	508
Pixel sensor dimension (mm ²)	280 × 56.5	280 × 75.5	280 × 94
Number of pixel sensors / layer	2		
Pixel size (μm ²)	O (15 × 15)		

3.2 Chip architecture

The TowerJazz 65 nm CMOS imaging technology is currently under evaluation for use in the ITS3 upgrade project. The first prototype developed using this technology is known as Multi-Layer Reticle 1 (MLR1), which integrates several test structures, including the Analog Pixel Test Structure (APTS), Digital Pixel Test Structure (DPTS), and CE65. The MLR1 chip incorporates a variety of devices aimed at exploring new sensor technologies. These include radiation-hard transistor test structures, charge-collection diode matrices, and both digital and analog pixel prototypes. Figure 3.4 shows examples of the pixel sensor test chips implemented in the MLR1. Each of these prototype structures has physical dimensions of 1.5 mm × 1.5 mm.

3.2.1 Digital Pixel Test Structure

Digital Pixel Test Structure (DPTS) consists of a 32 × 32 matrix of 15 × 15 μm² pixels. The main features of DPTS are time-based encoding of hit position and time over threshold (ToT) and a single digital current-mode logic (CML) output. It also has single and multiple pixel selection and pulsing. A dual pixel selection system is one of the features that includes direct decoder access and shift register slow control access. This test structure is intended to evaluate the dependability and efficiency of a distributed, asynchronous, time-based encoding and readout technique. A chip evaluation will also reveal information on the applicability of the custom digital cells that were used to build the architecture. The analog front end, which consists of an

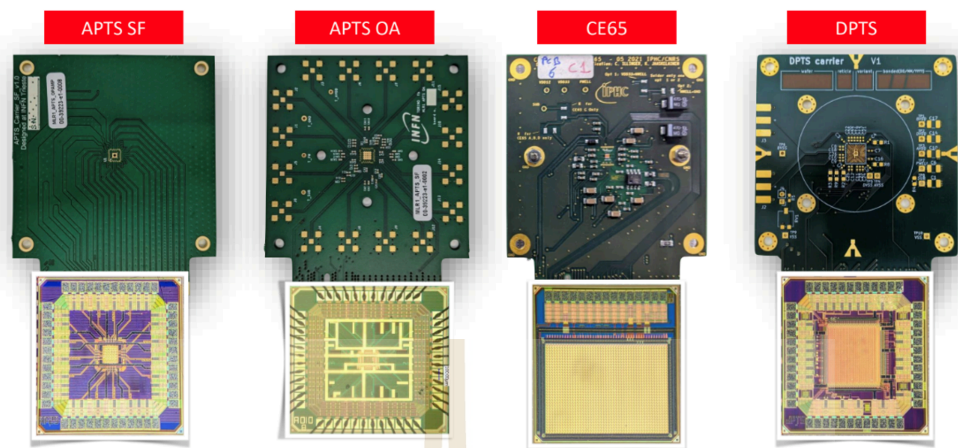


Figure 3.4 The MLR1 architecture: APTS prototype including SF (Source Follower) and OA (Operational Amplifier), CE65 and DPTS prototype (collaboration, 2024).

amplifier and a discriminator, is responsible for activating the digital encoder. The digital readout digitizes and transmits all of the pixel hits as a single digital output.

3.2.2 Analog Pixel Test Structure

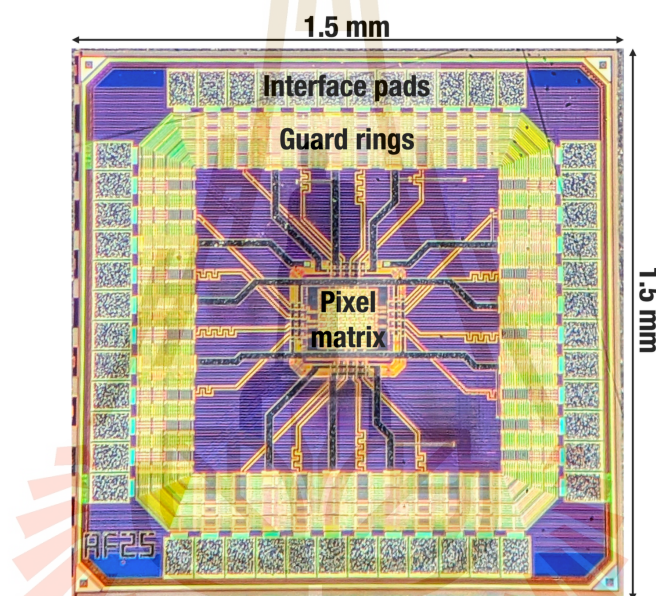
APTS is a sensor that has a high-speed analog readout, is intended to be used for sensor characterization, and has a variety of sensor types. APTS has two prototypes: a source follower (SF) and an operational amplifier (OA). The source follower is a fundamental source follower structure with a high-rate analog output. With a termination resistance of 50 ohms and a high-speed OPAMP buffering the front-end output, the board demonstrates enhanced timing performance. Front-end structures resemble basic source-follower architectures. The APTS allows for reverse substrate voltages ranging from 0 to -5 V. Figure 3.5 and 3.6 provide microscopic images of the APTS chips, while Table 3.2 outlines its major properties and several variants.

Analog pixel test structure - source follower (APTS SF) is a 1.5 mm \times 1.5 mm prototype chip, containing a 4 \times 4 pixel matrix. The chip has four different pixel pitches following 10, 15, 20, and 25 μm .

Analog pixel test structure - operational amplifier (APTS-OA) has dimensions of 1.5 \times 1.5 mm², including a 4 \times 4 pixel matrix with a 10 μm pitch.

Table 3.2 Analog Pixel Test Structure main characteristics.

	APTS
Die size	1.5 mm × 1.5 mm
Matrix	6 × 6 pixels
Readout	Direct analogue of central 4 × 4 pixels
Pitch	10, 15, 20 or 25 μm
Design	Standard, mod., mod. with gap
Split	1, 2, 3, 4
Variant	Reference, larger n-well, smaller p-well, finger p-well

**Figure 3.5** APTS Source Follower (SF) chip in microscope scale (collaboration, 2024).

3.2.3 Circuit Exploratoire 65 nm (CE65)

The whole CE65 architecture can be divided mainly into four parts: a pixel matrix, column and row selectors, column buffers, and an output buffer. The CE65 contains a pixel matrix with analogue readout in a rolling shutter configuration. A common pixel matrix layout has 64 by 32 pixels, with a pixel pitch of 15 μm , and three versions distinguished by the type of amplifier housed within each pixel: alternating current (AC), direct current (DC), and synchronous feedback (SF).

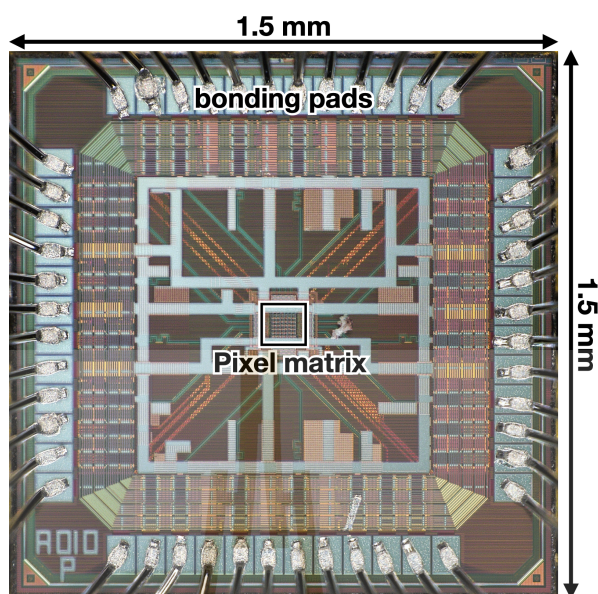


Figure 3.6 APTS Operational Amplifier (OA) chip in microscope scale (collaboration, 2024).

3.3 Basic chip tests

This section provides a fundamental understanding of the functionality of the sensor under the laboratory test. This section measures the electronic parameters of the APTS-SF chip such as the pulsing signal, threshold value, and noise level.

Our experimental setup is shown in Figure 3.7. The radioactive source holder, which is constructed from 6061 aluminum, fastens the ^{55}Fe at the top with an aperture to allow the radioactive decay of beta particles to pass through. A proximity card is linked to the MAPS, which is then attached to the carrier card. The DAQ board was driven by a 5 V power supply and linked to a proximity card. The ^{55}Fe is positioned in front of the MAPS sensor at a fixed distance of 1 cm. To operate the sensor and testing, EUDAQ software is used to collect data by controlling both the sensor's current and voltage. The sensors were tested at different back bias voltages, ranging from -0.0 to -4.8 V.

3.3.1 Pulsing signal

The objective of the pulsing test is to investigate the relationship between the sensor and the external trigger signal, particularly focusing on the variations in the

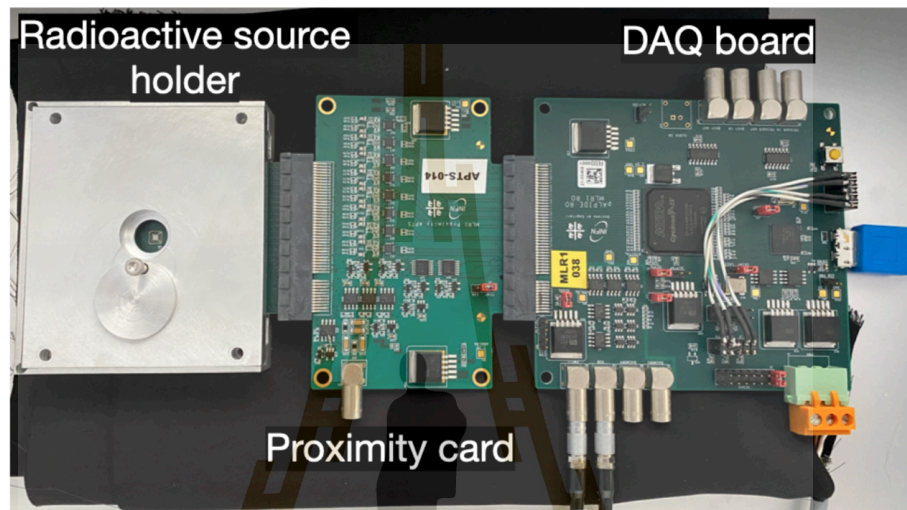
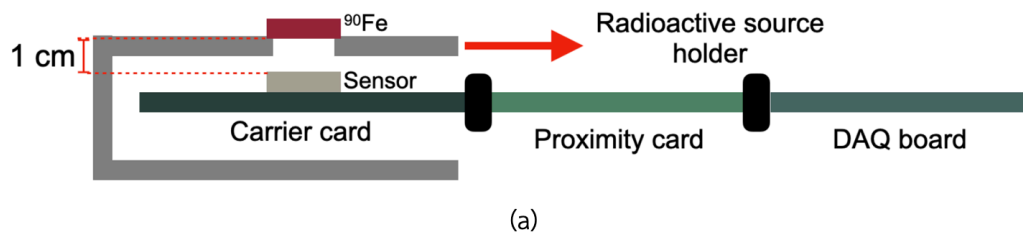


Figure 3.7 Laboratory test setup. Panel (a) shows a schematic diagram of the experimental setup, and panel (b) presents the actual relativistic experimental configuration.

signal's rise or fall. The study of the pulsing signal was divided into two processes. The first process is to observe the sensor behavior by controlling a pulsing bias voltage (V_H) to adjust the amplitude of the pulsing signal. The other aims to study the pulsing signal when the back bias voltage (V_{BB}) is applied to the sensor. Figure 3.8 shows the relationship between the maximum amplitude of the pulsing signal at different V_H under various bias voltages. Applying V_H of 1200 mV and V_{BB} of -4.8 V, the pulsing signal rises to its maximum amplitude. By raising both the injection voltage and the back-bias voltage at the same time, the sensor's signal responsiveness is improved. This makes charge collection more efficient and signals stronger.

3.3.2 Trigger threshold

Operating a sensor always generates background noise. The optimization of the threshold value was required to achieve the balance between data readout speed

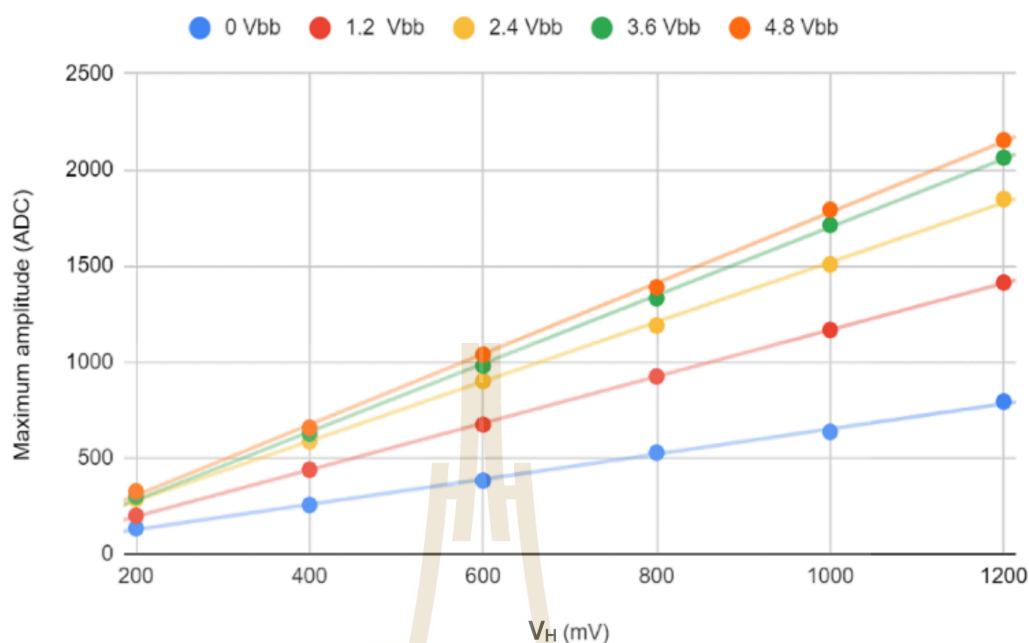


Figure 3.8 The relation between maximum amplitude of pulsing signal at different pulsing bias voltage (V_H) under various back bias voltage (V_{BB}).

and background noise levels. A higher threshold value results in a longer data-collecting time while lowering the noise. Faster operation is possible with a lower threshold value, but the trade-off is more noise. Appropriate threshold settings are crucial for sensors to operate accurately and efficiently. Figure 3.9 shows that the noise frequency was less than 0.1 Hz when the threshold value for each V_{BB} was chosen.

3.4 Performance of the chip

This section shows the details of the sensor measurement by using the radioactive source. The goal of this measurement is to ensure that the sensor accurately detects particles and provides reliable data.

3.4.1 ^{55}Fe radioactive source

Iron-55 (^{55}Fe) is a radioactive element that has a half-life of 2.73 years. It decays into manganese-54 (Mn-54) by releasing a low-energy gamma ray and capturing an electron in the inner orbit. This can be used to test and calibrate the detector (Sadeghi et al., 2012). The decaying production can be identified by its energies and

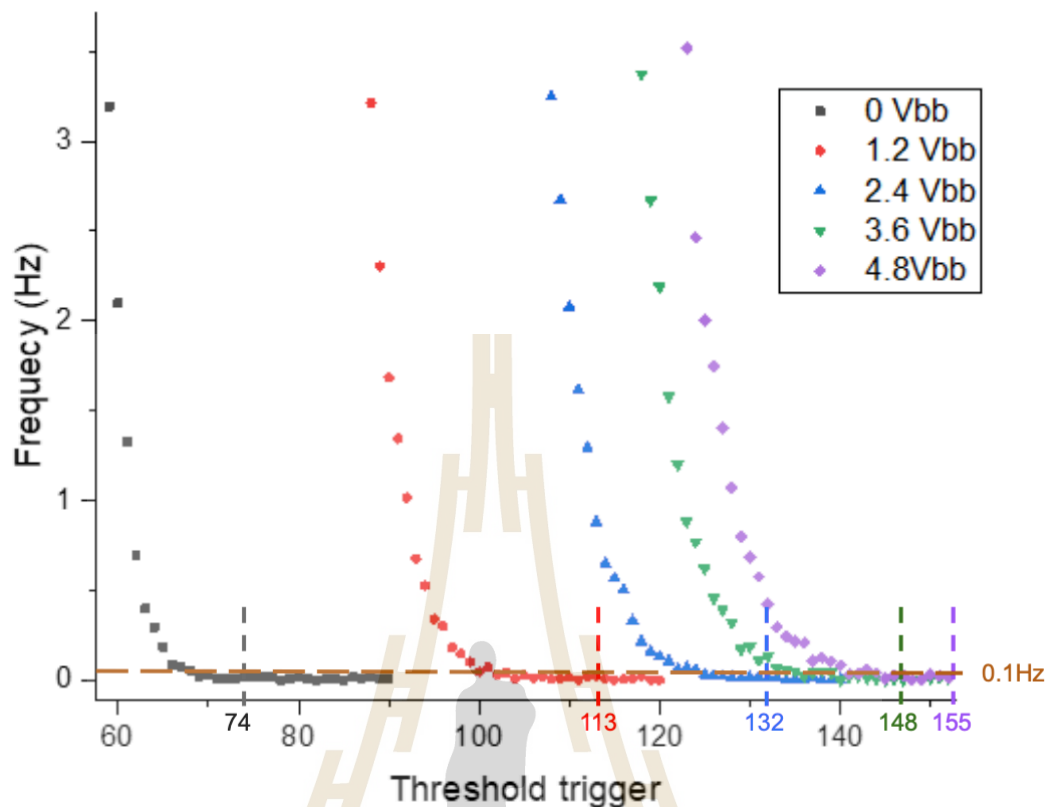


Figure 3.9 The relationship between noise frequency and trigger threshold.

rates normalized to 100 disintegrations, as shown in Table 3.3.

^{55}Fe emits 5-6 keV electrons, having an amount of 2.9 g/cm^2 in air. The range of this emission is 2.4 mm, which is smaller than the distance between ^{55}Fe and the sensor.

3.4.2 Observable in ^{55}Fe analysis

This part shows the activity for testing the sensor by using the radiation source. The aim of this test is to measure the decayed particles at different back-bias voltages. The setup was similar to the basic chip test. This work uses a ^{55}Fe radiation source for testing the sensor by replacing it on the radiation source holder. The main parameter for this test is the trigger threshold. This parameter will set the threshold for selecting the signal and noise. The trigger threshold was tested and selected as mentioned in Section 3.3.2. The setup parameters were shown in Table 3.4. During the analysis, the threshold value will be set for the analysis results. This parameter is the threshold of the minimum signal, which is defined as a real signal.

Table 3.3 The ^{55}Fe emissions produced (Podgorsak, 2009). The values in parentheses represent inaccuracies in the final digit(s) of the preceding value.

	Energy (keV)	Emission per 100 disintegration
Auger electrons	0.47 - 0.67	140.2 (8)
	4.95 - 6.53	60.1 (5)
	0.56 - 0.72	0.524 (21)
	5.888	8.45 (14)
X-rays	5.899	16.57 (27)
	6.490	3.40 (7)
	6.535	
γ	125.959	$1.3 (1) \times 10^{-7}$

Table 3.4 Parameters setting for ^{55}Fe radiation source testing.

Trigger threshold (ADC)	V _{bb} (V)	Number of events	Threshold value (mv)
75	-0.0	100,000	5
115	-1.2	100,000	5
140	-2.4	100,000	5
155	-3.6	100,000	5
160	-4.8	100,000	

Figure 3.10 shows the distribution of cluster size of the APTS sensor. This distribution is the number of pixels that were activated by each particle that hits the sensor. The highest distribution is 1 pixel, and the largest cluster size is 6 pixels. The highest signal that is generated by the pixel is called the seed signal, and the signal around the seed signal is called the neighbor signal. The sum of all signals is called a matrix signal.

The performance of the sensor can be investigated by using the ^{55}Fe radiation source. The CERN's results were used as reference results. Figure 3.11 shows the result of the source scan with three APTS sensors: AF15P_W22B4 was tested at Catania, AF15P_W22B2 was tested at CERN, and AF15P_W22B33 was tested at SLRI in Thailand. All chips have the same trend of all results. Seed signal, mean cluster size, and noise rise when V_{BB} was applied to the sensor, whose seed signal value is between 40 and 120 mV, mean cluster size is between 1.4 and 1.6 pixels, and noise value is between 0.9

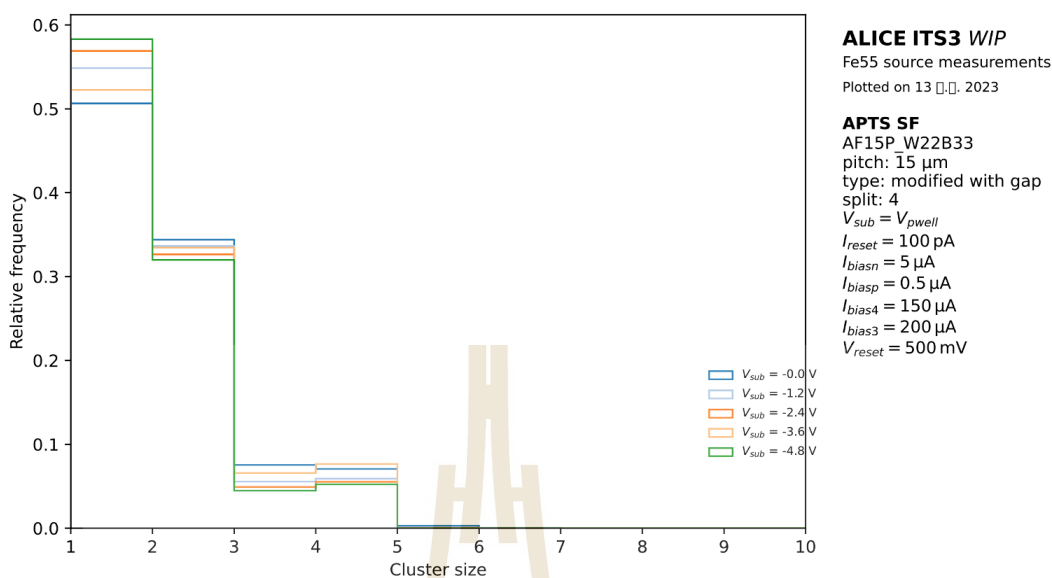


Figure 3.10 The relationship between relative frequency and cluster size of APTS sensor at different back-bias voltage.

and 1.7 mV. The capacitance of the sensor decreased when V_{BB} was applied; the value is between 6 and 2.6 fF. The main parameter is the charge collection efficiency (CCE). This parameter slightly decreased when V_{BB} was applied. However, the requirement of sensor efficiency is above 99%. This result shows that the CCE is still more than 99% when operated with the V_{BB} at -4.8 V.

3.4.3 Performance at different temperatures

This experiment aims to check the performance of the sensor under different temperatures. The setup was placed inside the incubator, which has a controlled temperature of 5 degrees Celsius to 60 degrees Celsius. The setup included an APTS chip with a radiation source holder, which connects to the proximity card and DAQ board. Power cables and all connections were connected to the power supply and computer that are located outside of the incubator (see Figure 3.12).

The experiments were tested under nine temperatures, starting at 10, 15, 20, 25, 30, 35, 40, 50, and 60 degrees Celsius. The sensor was also tested with different back-bias voltages at -0.0, -1.2, 2.4, -3.6, and -4.8 V at each temperature. The test began after heating the sensor to the expected temperature and placing the ^{55}Fe radiation source in the radiation source holder. Figure 3.13 depicts the charge collection efficiency (CCE) at various V_{BB} : -0.0, -1.2, 2.4, -3.6, and -4.8 V. The CCE reduced when V_{BB}

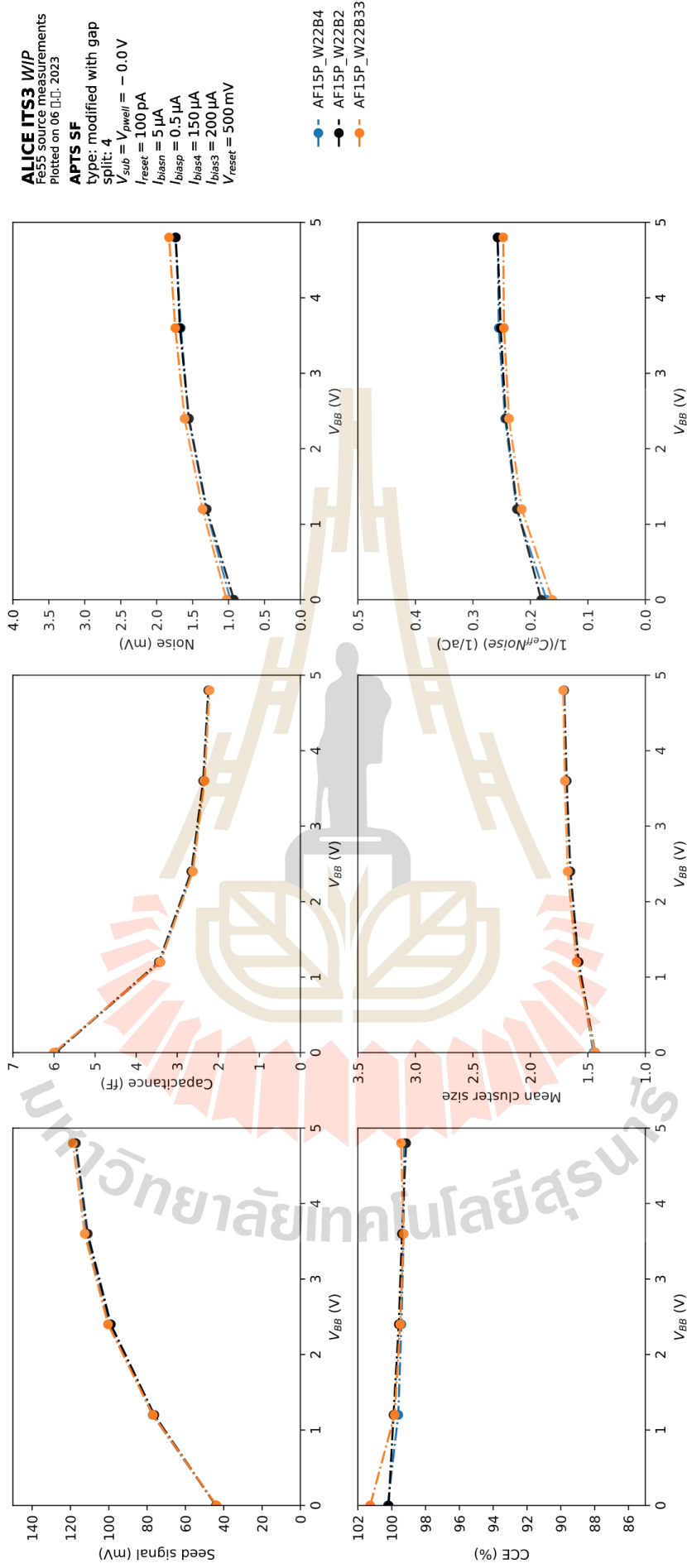


Figure 3.11 The plots of APTS sensor performances for detecting the particles from the ^{55}Fe decay.

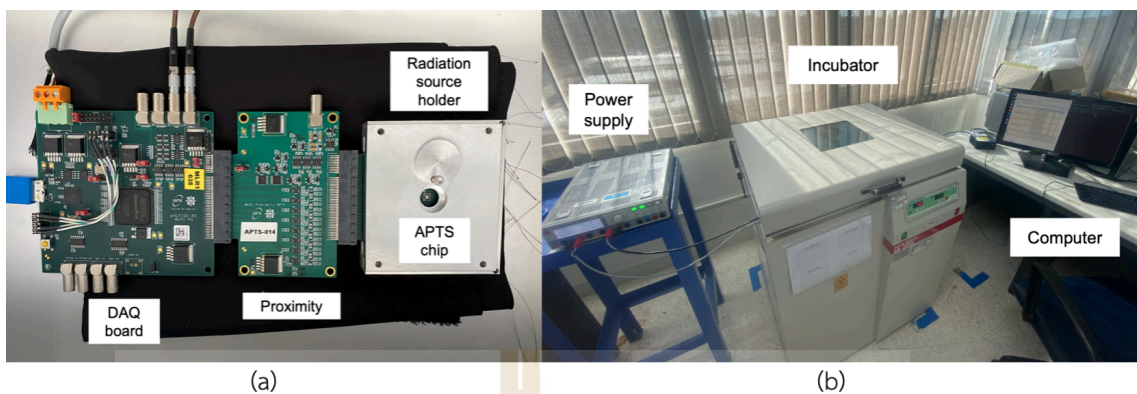


Figure 3.12 The experimental setup for testing sensor performance under different temperatures. Panel (a) shows the chip test setup, and panel (b) shows the setup placed inside the temperature-controlled incubator.

was applied to the sensor. There are similar results for all temperatures; the sensor can operate normally without being affected by temperature changes.

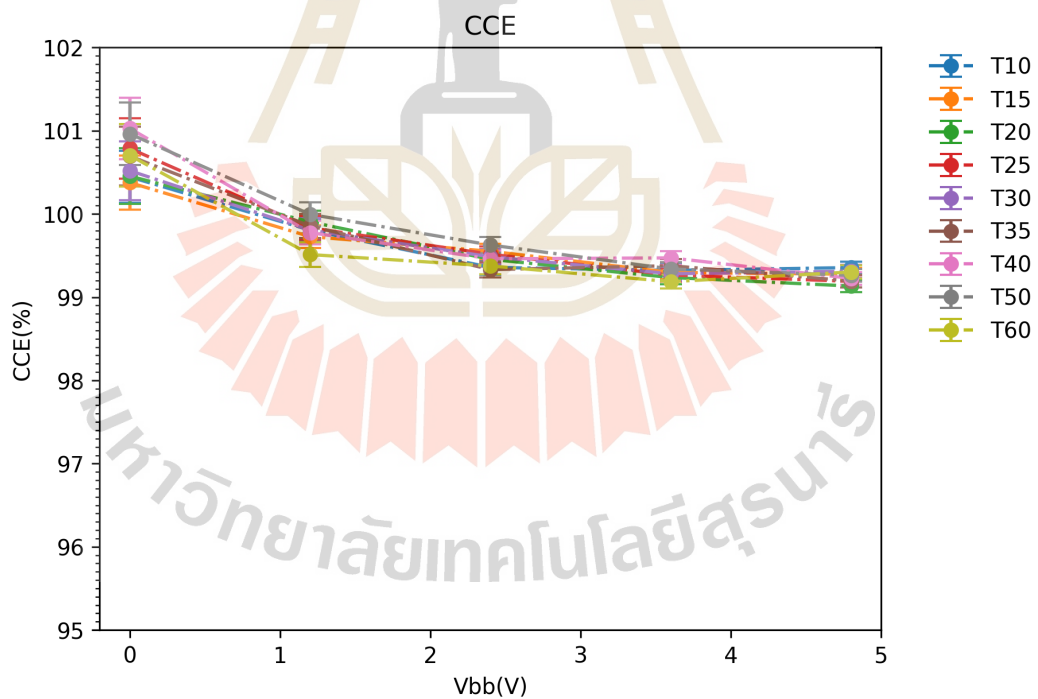


Figure 3.13 The relation chip between charge collection efficiency (CCE) and back-bias voltage (V) at different temperatures.

3.5 Radiation hardness performance of sensor

The APTS sensor was tested for performance under the specific conditions, with normal operation and operation after being irradiated with the high-dose particle.

3.5.1 The radiation test at HRH Princess Maha Chakri Sirindhorn Proton Center (HRSP)

The APTS sensor was placed in front of the 70 MeV proton beam provided by the radiation test at HRH Princess Maha Chakri Sirindhorn Proton Center (HRSP). The aim is to characterize the APTS sensor after it was irradiated with two TID dose steps: 100 krad and 500 krad. The proton beam can be described by a Gaussian with a deviation of about 5.95 mm in diameter at the zero isocenter. The single APTS was tested with a ^{55}Fe radiation source, using five different back-bias voltages for each TID dose. Figure 3.14 shows the experimental setup for the sensor irradiation at HRSP. The APTS chip was placed in front of the proton beam. After the sensor was irradiated, the pulsing signal was measured.

To obtain the number of fluence, it can be calculated based on the following equation,

$$\text{TID}[\text{krad}] = 1.602 \times 10^{-8} \times S[\text{MeV} \cdot \text{cm}^2 \cdot \text{mg}^{-1}] \times F[\text{cm}^{-2}] \quad (3.1)$$

where S is the linear energy transfer (LET) and F is the proton fluence. The LET of silicon for 70 MeV is $7.614 \text{ keV} \cdot \text{cm}^2 / \text{mg}$. The result of the calculation is that 100 krad has the number of fluence of 8.2×10^{11} , and 500 krad has the number of fluence of 4.1×10^{12} .

The non-ionizing energy loss induced by the 70 MeV proton beam is calculated as

$$\text{NIEL}[1\text{MeVn}_{\text{eq}} \cdot \text{cm}^{-2}] = 1.552 \times F[\text{cm}^{-2}] \quad (3.2)$$

where the factor 1.552 is a tabled coefficient. When the beam is stopped, the current measurement and pulsing test were performed.

Figure 3.15 illustrates the measurement of the mean cluster size and noise at a variety of back-bias voltages. Before and after proton beam irradiation, we observed that the mean cluster size values were comparable. When the APTS chip was applied to more back-bias voltages, the average cluster size increased from 1.48 to 1.65 pixels.

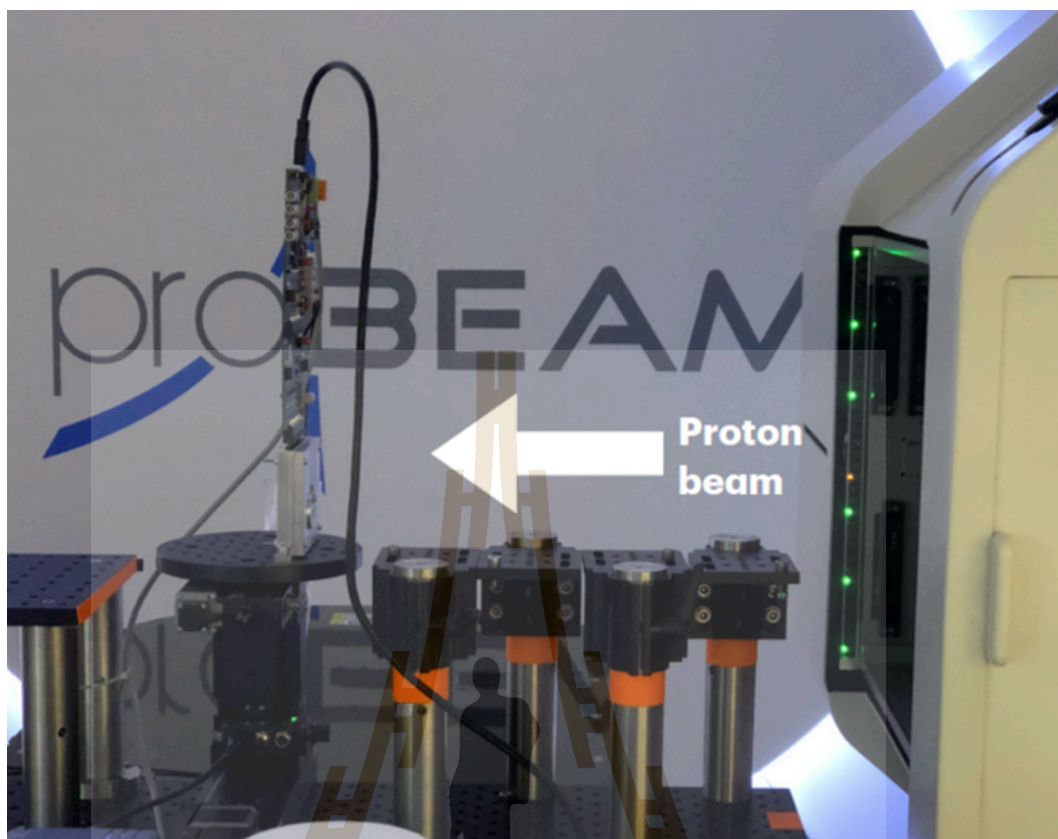


Figure 3.14 The sensor setup for irradiation with 70 MeV proton beam at HRSP.

The charge collection efficiency (CEE) was analyzed both before and after an irradiated sensor was used at various back-bias voltages, as illustrated in Figure 3.16. The non-irradiated sensor demonstrates the highest CCE at V_{BB} of -0.0 V. The CCE decreased as the irradiation dose increased.

3.5.2 Conclusion

In this chapter, the design concept, architecture, and performance evaluation of Monolithic Active Pixel Sensors (MAPS) for the ALICE ITS3 upgrade have been presented. The material budget optimization strategy for the new Inner Tracking System was outlined, highlighting the reduction of non-sensitive components to achieve minimal material thickness. The architecture and functionalities of the prototype chips, including the Analog Pixel Test Structure (APTS), Digital Pixel Test Structure (DPTS), and Circuit Exploratoire 65 nm (CE65), were described in detail. Laboratory characterization procedures were introduced, covering pulsing tests, threshold optimization, and measurements with a ^{55}Fe radioactive source. The influence of operating temperature and

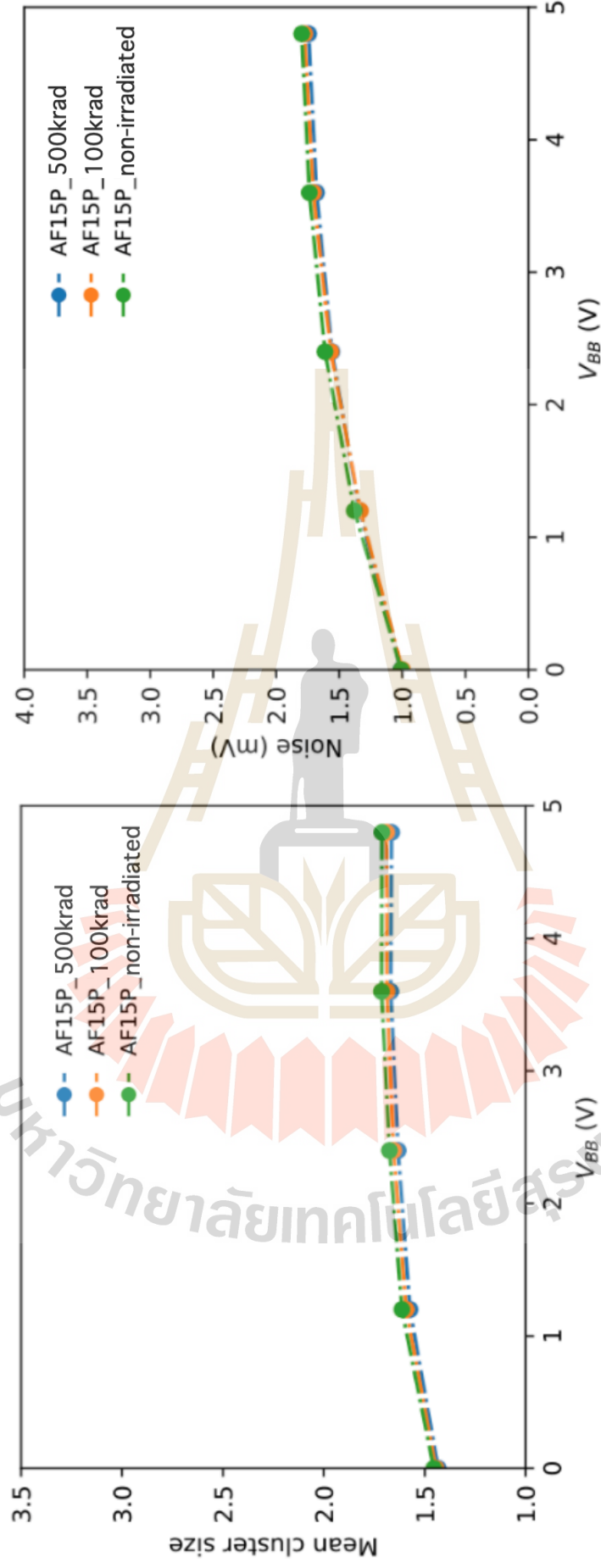


Figure 3.15 The relationship between mean cluster size (left) and noise (right) and back-bias voltage before and after being irradiated by a proton beam.

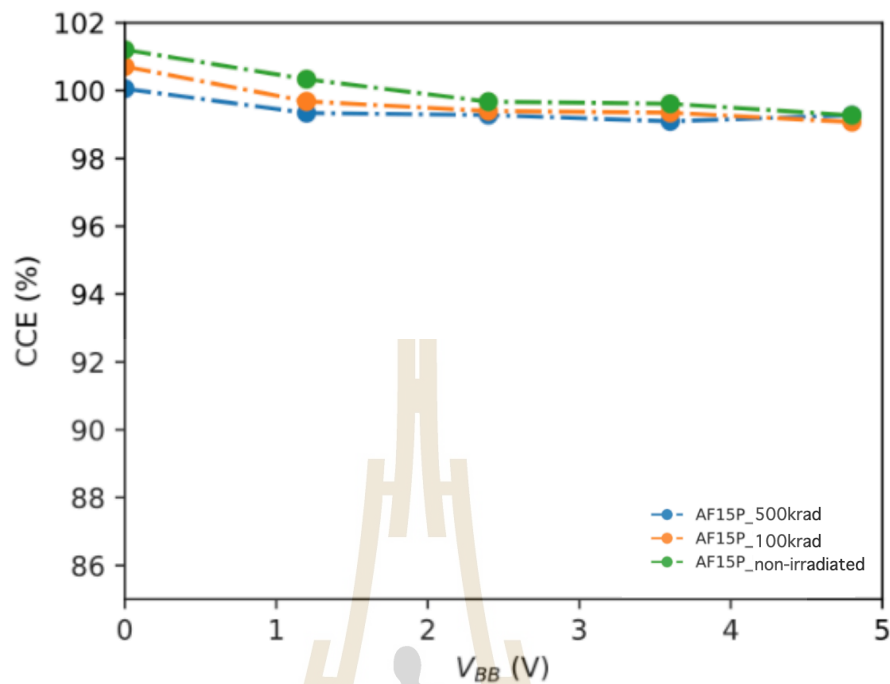


Figure 3.16 The relationship between the charge collection efficiency and back-bias voltage before and after being irradiated by a proton beam.

radiation exposure on sensor performance was also investigated, demonstrating the robustness of the devices under varied experimental conditions. These results provide critical input for optimizing the ITS3 design and serve as a reference for future MAPS development in high-energy physics experiments. In the next chapter, the focus will shift to the detailed analysis of beam test results, where the performance of the MAPS will be assessed under realistic particle detection conditions.

CHAPTER IV

BEAM TEST CHARACTERIZATION USING BEAM AT SLRI-BTF

This chapter describes the telescope construction utilized in the SLRI experiment. It is made up of six ALPIDE monolithic active pixel sensors and an APTS chip in the middle as a device under test (DUT). The EUDAQ framework is responsible for the telescope's control and data collection. The output data is in the form of a binary or raw file. The purpose of this section is to give preliminary results of the beam test with the telescope utilized at SLRI for electron beam testing.

4.1 SYNCHROTRON LIGHT RESEARCH INSTITUTE (SLRI)

The Siam Photon Source (SPS) provides synchrotron light (see Figure 4.1) that is produced by a 1.2 GeV electron beam to study fundamental science, biological, medical science, and industrial research. The SLRI accelerator includes four main parts as follows:

1. An electron gun which produces a large amount of electron.
2. A 40 MeV Linear Accelerator (LINAC) that provides an electron bunch.
3. A synchrotron booster that accelerates electron beams to an electron beam energy of 1.2 GeV.
4. A storage ring where the electron beam is stored to generate synchrotron light.

SLRI has initiated the project that utilizes the high-energy electron beam by setting up a dedicated Beam Test Facility (BTF). The aim of SLRI-BTF is to produce a defined number of electrons from a few to millions of electrons per burst. The electron energy can range up to 1.2 GeV. The main object is to characterize and test the high-energy detectors. SLRI-BTF has provided sufficient beam time that serves from the current injection scheme. The facility can operate during the normal service of synchrotron light. The facility is extended from the high-energy beam transport beamline (HBT) and is located underground together with other components.

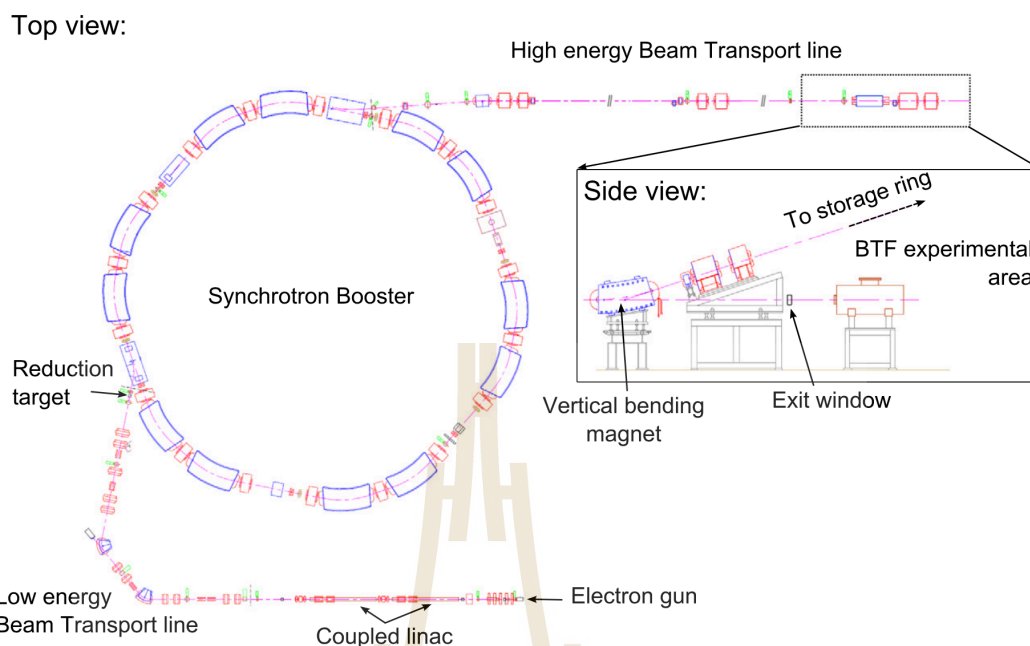


Figure 4.1 Layout of the Siam Photon Source (SPS) injector consisting of an electron gun, a coupled 40-MeV linacs, a Low-energy Beam-Transport line (LBT), a synchrotron booster, and a high-energy beam-transport line (HBT) (Kittimanapun, K., Chanlek, N., Klysubun, P., Kobdaj, C., Lakrathok, A., Laojamnongwong, N., . . . Musa, L., 2019).

4.1.1 BEAM TEST FACILITY (BTF)

The SLRI-BTF experimental station is located next to the vertical bending magnet in an area of 3.5 m × 3.5 m. While the SLRI-BTF is running, the bending magnet is deactivated. The synchrotron booster accelerates the electrons, whose energy is adjustable from 40 MeV up to 1.2 GeV. By modifying a tungsten target, the number of spilled electrons at very low beam intensities is fewer than 10 per spill (Kittimanapun et al., 2017). The experimental area has been renovated to accommodate the installation of detectors and tested instrumentation, as well as a local computer and electronics for detector components that are locally installed and remotely controlled during operation (Kittimanapun et al., 2016).

4.1.2 Intensity reduction system

The goal of reduction is to reduce the number of electrons to less than 10 electrons per bunch at the experimental station. A tungsten target manipulator has been mounted at two locations: the beginning of HBT and the end of LBT (see both

Table 4.1 Parameters of the electron beam at the High-Energy Beam Transport Line (HBT).

Particle	Electron
Energy	up to 1.2 GeV
Energy spread	0.05%
Current	10 mA
Pulse duration	8.5 ns
Bunch length	0.5 ns
Repetition rate	0.33 Hz
# of electron per burst	10^8

red arrows in Figure 4.2). A flat side facing the electron beam is used to install the 40 mm \times 60 mm target. The target is thick enough to entirely block the primary beam, and the center thickness of the transport line can be adjusted up to 6 mm with a resolution of 10 μ m. The interaction of electrons in the target reduces the primary beam intensity, while the secondary beam intensity is reduced within the synchrotron booster.

4.1.3 Energy selection for SLRI-BTF

This part is to study the energy that will be used for sensor characterization. The energy selection will be chosen from the synchrotron booster of SLRI. To investigate the energy at SLRI-BTF, it is necessary to study the current ramping pattern of the bending magnet.

Table 4.2 presents the ramping times to pulse the kicker and the septum to extract the electron beams, magnet currents of the synchrotron booster, energies of the extracted electron beams, and signal widths of the electron beam during the acceleration.

The pixel sensor telescope detected the electron beam, which is adjusted to transfer the electron beam to SLRI-BTF at the monitoring screen. Moreover, the electron beam with different energies can be confirmed. The electron beam profile is obtained by using the pixel sensor telescope. Figure 4.3 shows the electron beam profile that was detected on the first plane of the pixel sensor telescope. Beam size is 6.53 mm \times 2.64 mm.

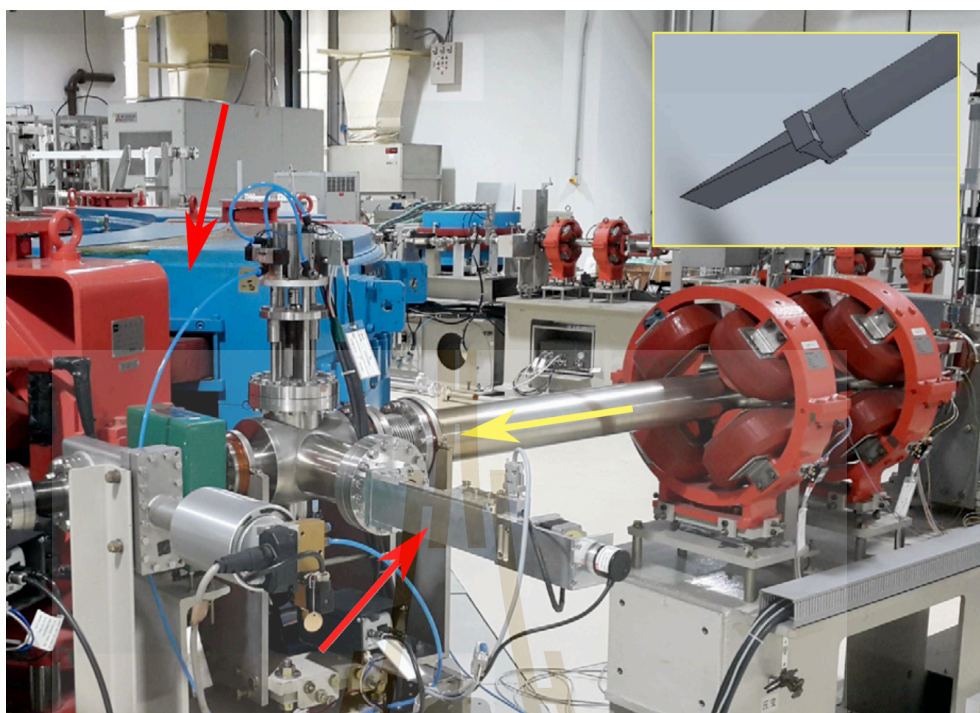


Figure 4.2 The installation of the tungsten target manipulator. The aim is to reduce the particle intensity of the 40 meV electron beam at the synchrotron booster. (Kittimapanun, K., Chanlek, N., Klysubun, P., Kobdaj, C., Lakrathok, A., Laojamnongwong, N., . . . Musa, L., 2019).

4.2 Pixel sensor telescope setup

A pixel sensor telescope has been installed at the SLRI-BTF experimental station in preparation for checking the quantity of electrons produced at SLRI-BTF and investigating the efficiency of the MAPS. The pixel sensor telescope was fixed to a lead box as a shielding box. The sensor stack is called a pixel sensor telescope. The pixel sensor telescope has a total of seven planes of sensors, six of which are reference and the other is Device Under Test (DUT) (Kaewjai et al., 2019).

4.2.1 Experimental setup

The pixel sensor telescope was fixed to the lead plate with a distance between each sensor plane of 2.5 cm. Figure 4.4 illustrates the idea and experimental setup of the test beam telescope at SLRI-BTF. The configuration of measuring position sensors that are perpendicularly aligned with the particle beam. The background

Table 4.2 Parameters to extract electron beam at different energies (Kittimanapun et al., 2024).

Ramping time (ms)	Magnet current (A)	Electron beam energy (GeV)	Signal width (ms)
1199	1464	1.20	1090
699	1249	1.05	591
599	1030	0.89	491
499	837	0.72	391
299	174	0.35	191

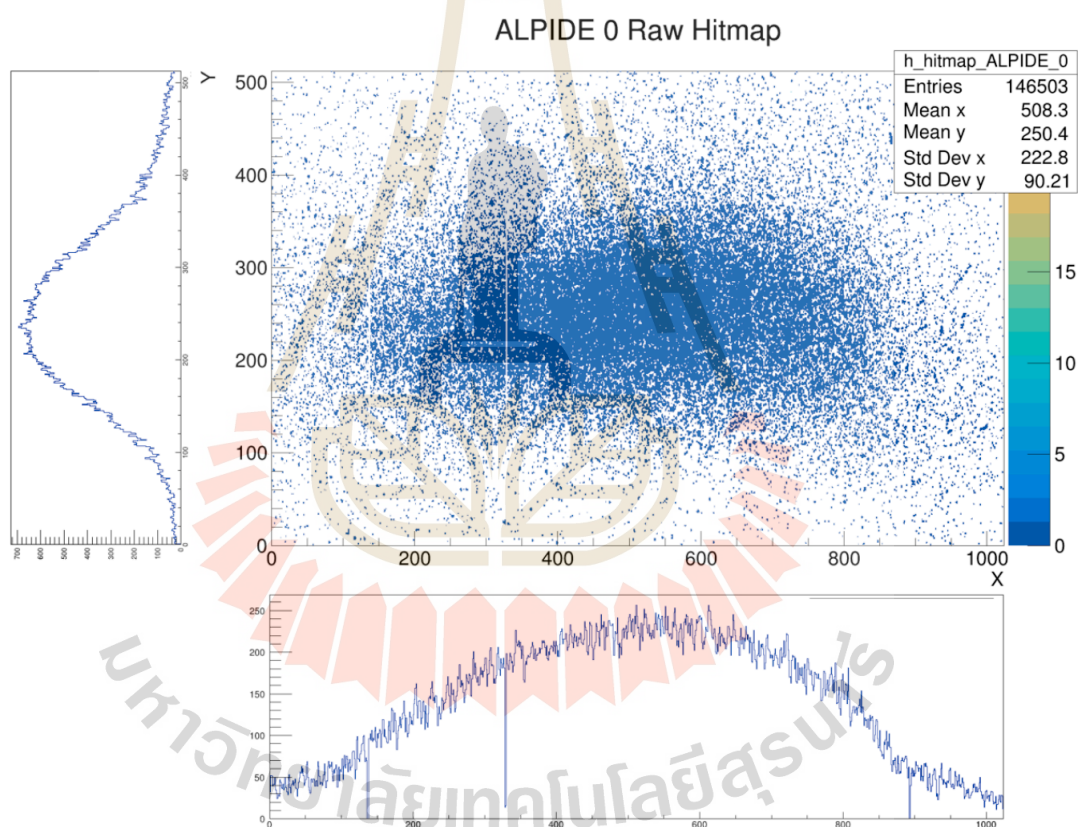


Figure 4.3 Electron beam profile of the first plane that captured at the SLRI-BTF (Kittimanapun et al., 2024).

bias voltage is applied to all ALPIDE sensors except the DUT. Once the particle passes through the pixel sensor telescope, the signal is detected and the track of the particle can be reconstructed. The data analysis is performed by the software that is developed

by the ALICE team based on the EUDET telescope framework.

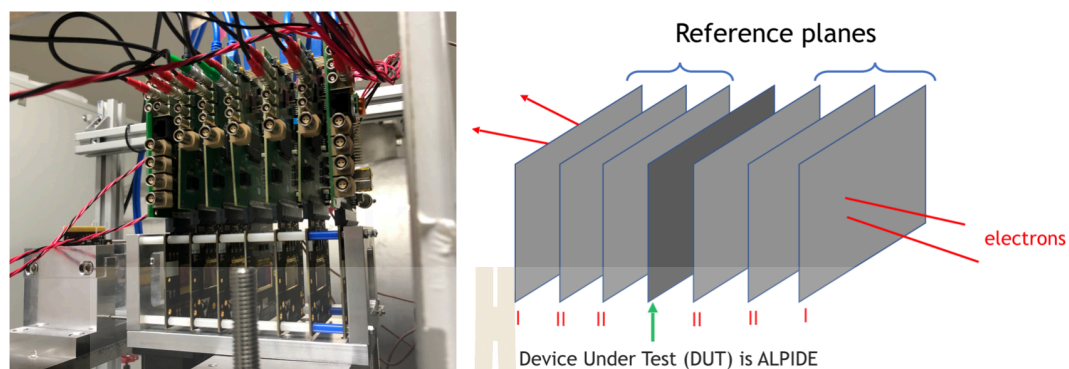


Figure 4.4 The SLRI-BTF pixel sensor telescope experiment (left) and the pixel sensor telescope concept (right) (Kaewjai et al., 2019).

In order to prepare the electron beam, SLRI-BTF has the target manipulator to adjust the beam intensity. This section provides the beam information for the beam test. The electron beam energy is 1 GeV with a repetition rate of 2 s. The trigger is used by the main clock. The telescope recorded 2,000 events. The beam profile is shown as low and high electron intensity (see Figure 4.5).

4.2.2 EUDAQ framework

The EUDAQ framework is primarily based on the trigger logic unit (TLU). The framework's many modules can run on separate machines and communicate with one another via an Ethernet network utilizing TCP/IP connections. This provides for a more flexible DAQ network architecture, which is especially useful for test beams where detectors and users may change often. A typical EUDAQ network is depicted in Figure 4.6. To begin, the EUDET TLU (Cussans, 2009) was employed in conjunction with renowned EUDAQ for the DAQ of EUDET-type Mimoso26 sensing telescopes (Jansen, H., Spannagel, S., Bulgheroni, A., Claus, G., Claus, G., Corrin, E., . . . Winter, M., 2016; Hu-Guo et al., 2010).

The EUDAQ version 2 is used in this work. The firmware must be installed in the DAQ board that contains the FPGA chip over USB. The configuration files are edited to match the experiment setup, such as the number of sensors, output file path, ALPIDE characteristics, and so on. TMUX is used to execute the EUDAQ GUI process while waiting for the signal from the trigger to initiate the execution. The GUI interface needs the user to enter the frequency as well as the optional HIGH/LOW signal per pulse. As

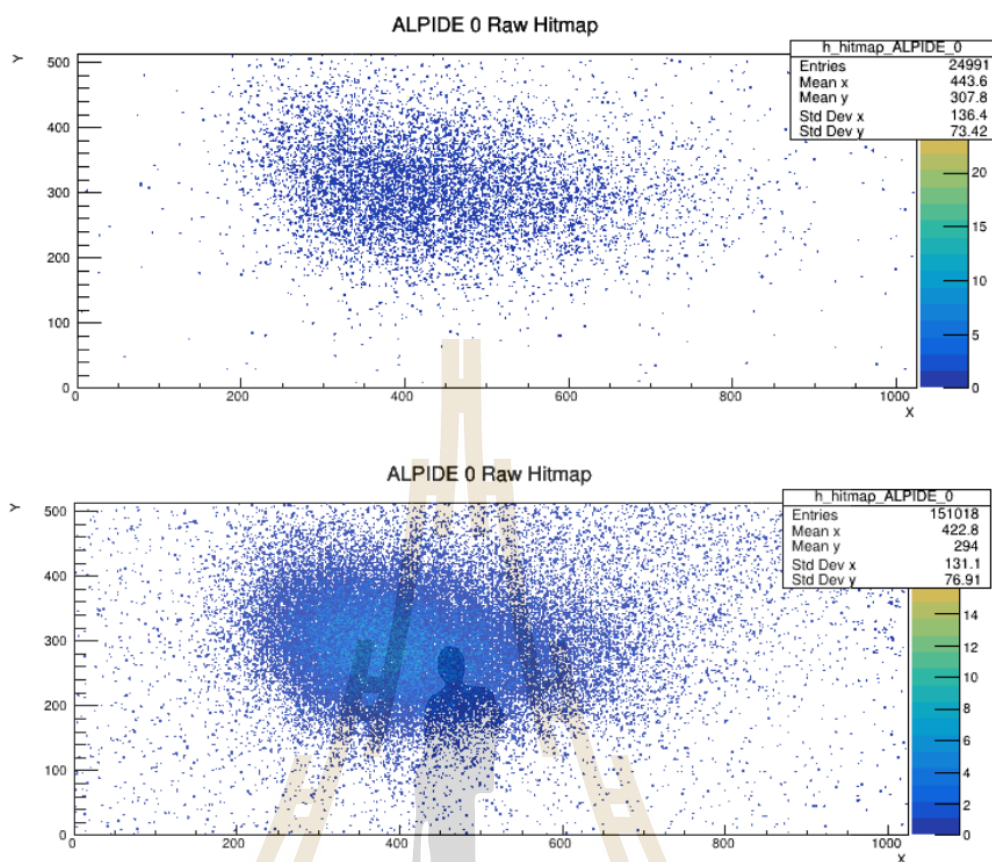


Figure 4.5 The electron hit position. The upper figure shows the low electron beam intensity (<5 of clusters) and the lower figure shows the high electron beam intensity (>30 of clusters).

illustrated in Figure 4.7, the micro-controller accepts the serial signal from the interface and stores user input in an FPGA register for creating a trigger signal to the DAQ.

4.3 Testbeam results

The APTS chip was tested with a pions beam of 120 GeV at the CERN SPS H6 (Banerjee, D., Bernhard, J., Brugger, M., Charitonidis, N., Doble, N., Gatignon, L., Gerbershagen, A., 2021). The aim of this experiment is to study the detection efficiency and spatial resolution. This was made possible by using a telescope made of ALPIDE chips as reference planes, providing a tracking resolution of $\sigma_{\text{track}} = 1.94 \mu\text{m}$ (Mager, 2014). The telescope setup was placed inside a closed box. Two APTS sensors were mounted between the reference planes, as shown in Figure 4.8. The APTS served as

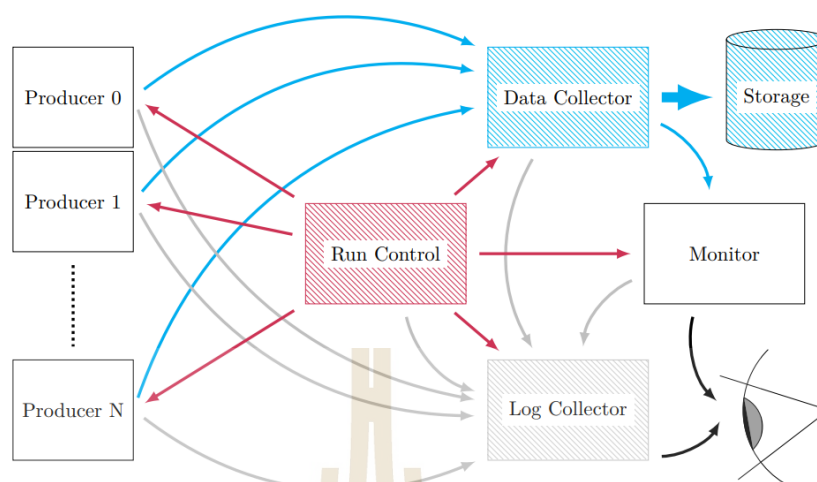


Figure 4.6 The EUDAQ network typically consists of several components, including the central command and control server known as Run Control, the Data Collector, which is responsible for creating global events and storing them on disk, the Log Collector, which manages and displays log messages, and the monitor application, which allows for real-time monitoring of data quality (Spannagel, 2016).

the DUT, while the other was positioned on a movable stage and operated as a trigger device. A cooling jig with circulating water at $T = 16.6$ C was used to maintain the DUT temperature constant. AF15P_W22B56 was set up as the DUT; the material budget is 0.05% of X/X_0 . The chip underwent 300 Mrad TID irradiation (much higher than the ALICE ITS3 requirement and reaching the ALICE 3 requirement). The DUT was tested with various back biases on the substrate ($V_{BB} = 0.0$ V, -1.2 V, and -4.8 V). AF25P_W22B7 was used as the external trigger with a constant substrate voltage of -1.2 V.

4.3.1 Analysis tools and method

Corryreckan is an analysis framework for test beam measurement of sensor telescopes. The performance of Corryreckan is to enable the telescope testing, qualification, and characterization in terms of efficiency, spatial resolution, and timing performance (Dannheim, D., Dort, K., Huth, L., Hynds, D., Kremastiotis, I., Kröger, J., . . . Williams, M., 2021). The major track model utilized in this work is the General Broken Lines (GBL) model (Blobe, 2006), which allows for kinks at each detector and accounts for multiple Coulomb scattering in all detector planes as well as the surrounding air.

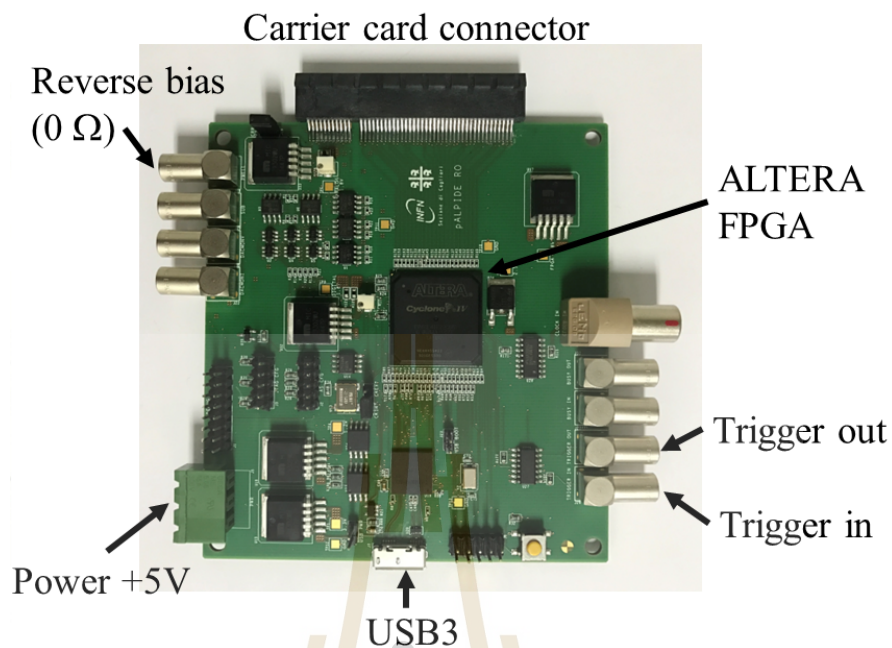


Figure 4.7 The board for data collecting. The external signal from the trigger system is received through the trigger-in port. The same signal is used as an output in the trigger-out. The Alterla FPGA is included in the board and is used to operate the EUDAQv2 firmware.

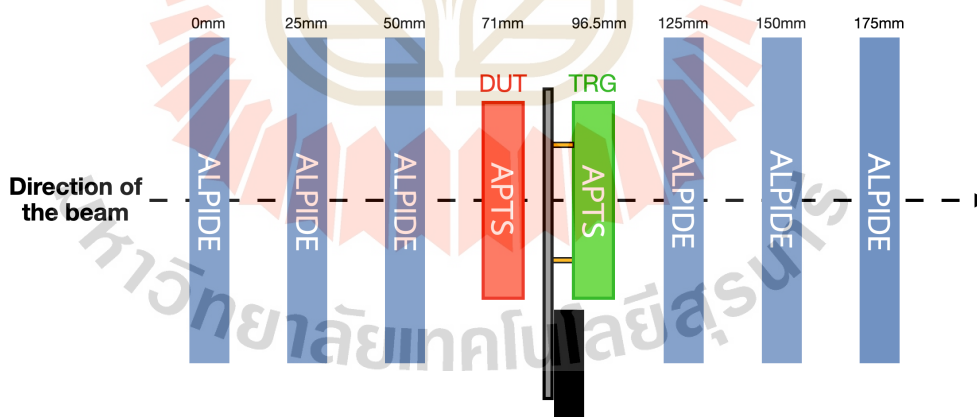


Figure 4.8 The scheme of the telescope setup consists of planes 3 and 4, which were made with APTS chips, and all others with ALPIDE chips. The telescope setup is not to scale. The setup was set at the SPS test beams.

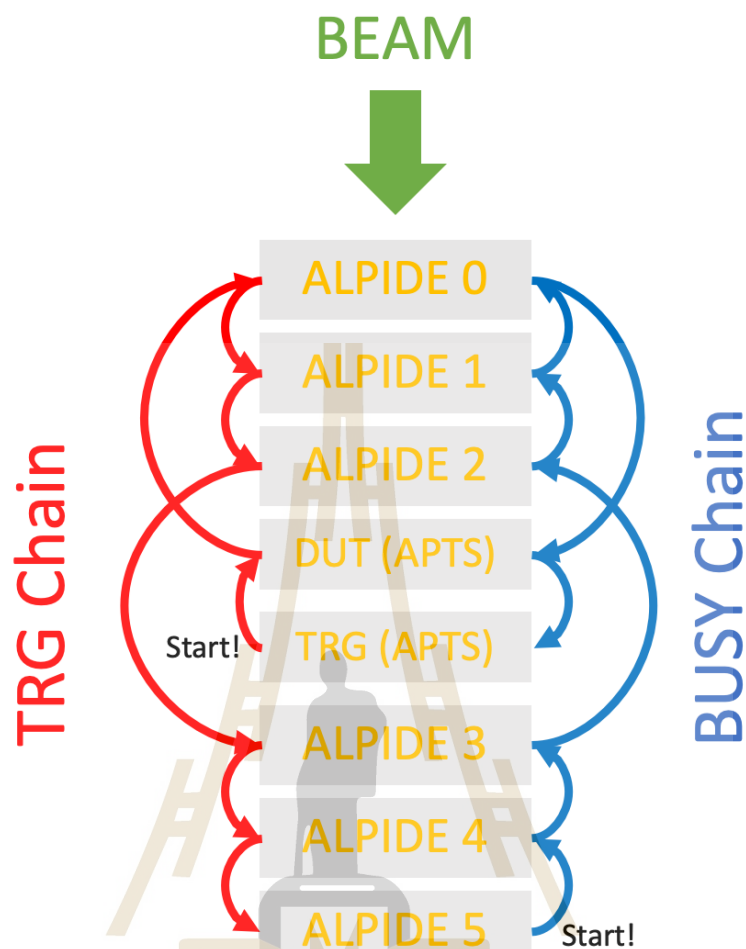


Figure 4.9 Pixel sensor telescope signal chain layout. The figure illustrates the wiring configuration of the ALPIDE sensors within the telescope, showing the paths of the trigger (TRG) chain and busy chain. The trigger chain (red arrows) initiates event acquisition, while the busy chain (blue arrows) manages readout synchronization and prevents overlapping triggers during data acquisition.

The Corryvreckan analysis chain begins with the assumption that a trigger APTS chip is a passive material (not employed in tracking). In the first step, all detectors are pre-aligned by calculating correlations between each detector in the setup and the reference plane. The framework comprises two processes for achieving alignment. The first is tracking the alignment of ALPIDE planes, with DUT excluded, while the second is DUT alignment. The algorithm optimizes the track χ^2 value with Minuit2, which uses the Millepede-II algorithm. The final phase is DUT analysis for charged thresholds of

80, 100, 120, 140, 180, 200, and 250 electrons. The detection efficiency and the spatial resolution have been determined by associating the DUT clusters to tracks passing inside a window that has a radius of $75 \mu\text{m}$ around the track intercept point on the DUT. The idea behind this configuration is that only tracks traveling through the four middle pixels were inspected to eliminate border effects.

The spatial resolution was measured as a hit/no-hit measurement. The residuals were calculated as the distance between the track's intercept on the DUT plane and the cluster position in both the x and y axes. The standard deviation of the two distributions was calculated, and σ_{track} was subtracted quadratically to get $\sigma_{x(y)}$. σ_{res} is the arithmetic average of σ_x and σ_y , indicating the final spatial resolution.

4.3.2 Alignment and residual

Alignment is the process of adjusting the sensor's geometry and positioning relative to the reference system. Misalignment can lead to systematic errors in hit position measurements, resulting in larger residuals. Residual calculation is one of the alignment processes. The residuals are computed as the difference between the measured hit positions and the predicted positions based on the alignment. The residuals show a symmetric distribution centered around zero, indicating that the measurements are well-aligned with the expected hit positions. The standard deviation values give insight into the spread of the residuals. Smaller standard deviations indicate better precision in hit detection.

Figure 4.10 shows the residual x and y distribution at different negative substrate bias. At $V_{\text{SUB}} = 0.0 \text{ V}$, the residuals exhibit a wider distribution, with standard deviations around $4.1 \mu\text{m}$ for X and $4.26 \mu\text{m}$ for Y, indicating lower precision and potentially higher noise levels. As the voltage is increased to -1.2 V , the standard deviation slightly decreases ($4.12 \mu\text{m}$ for X and $3.98 \mu\text{m}$ for Y), reflecting improved tracking accuracy and reduced misalignment. The most significant improvement is observed at $V_{\text{SUB}} = -4.8 \text{ V}$, where the standard deviations drop to $3.81 \mu\text{m}$ for X and $3.65 \mu\text{m}$ for Y, suggesting that the sensor's charge collection efficiency and overall resolution are optimized at this voltage. These trends indicate that a more negative V_{SUB} enhances the precision of hit localization, leading to more accurate measurements and better alignment between expected and measured hit positions in both directions.

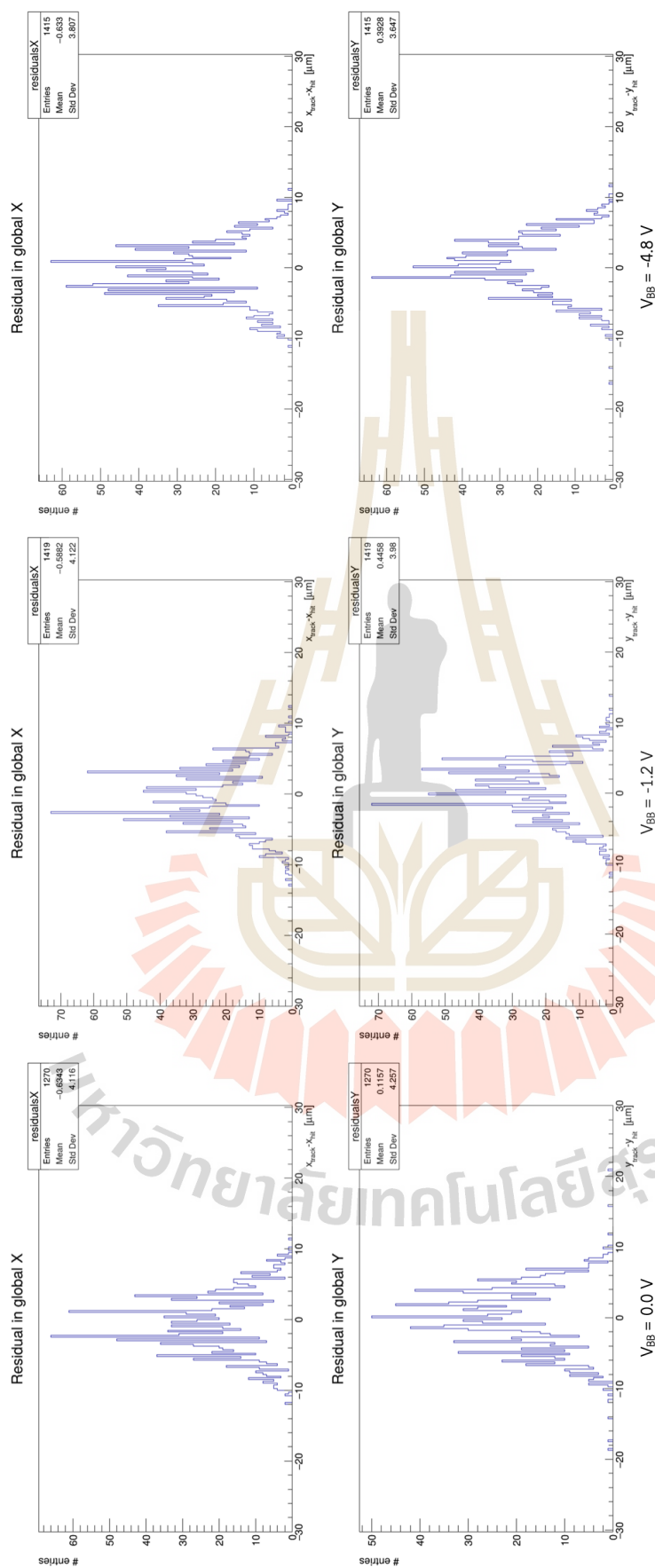


Figure 4.10 Residual distributions in global X (upper row) and global Y (lower row) coordinates at different negative substrate bias voltages (V_{BB}): 0.0 V (left), -1.2 V (middle), and -4.8 V (right). Each histogram illustrates the difference between the measured hit position ($x_{\text{hit}}, y_{\text{hit}}$) and the reconstructed track position ($x_{\text{track}}, y_{\text{track}}$).

4.3.3 Detection efficiency

The 15 μm modified with gap APTS sensor was irradiated with 300 Mrad TID. The detection efficiency of this chip was measured with four different values of V_{SUB} in relation to the charge threshold (e^-), as illustrated in Figure 4.11. Considering the beginning point for each curve, the detection efficiency with no bias voltage is lower than 99%. The oxide and interface portions of the APTS chip are significantly damaged from the irradiation, resulting in increased noise and decreased charge collection. These factors together lower detection efficiency. However, a higher negative voltage in the operating zone expands the depletion region within the silicon layer, enhancing charge collection. More negative V_{SUB} yields a greater detection efficiency of more than 99%.

Table 4.3 shows that the single APTS operation with a substrate bias V_{SUB} of -4.8 V can reach 99.728% efficiency up to 300 Mrad TID when the charge threshold is 100 electrons. At 0.0 V and -1.2 V, on the other hand, efficiencies are less than 99%.

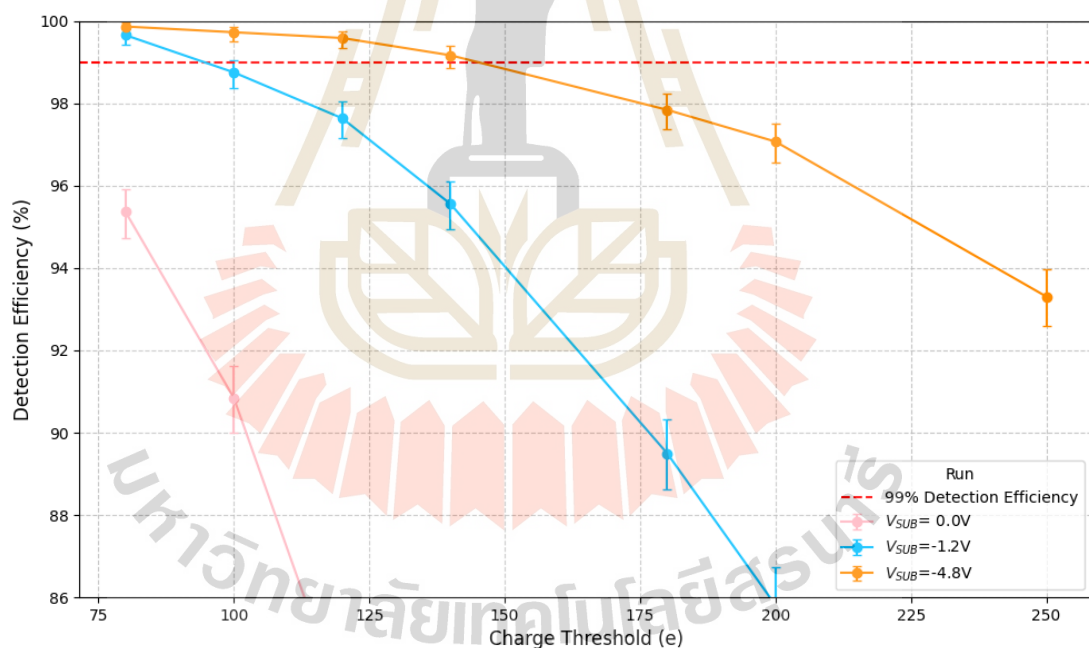


Figure 4.11 Detection efficiency plot of a 300 Mrad irradiated chip at various reverse substrate voltages as a function of the charge threshold. APTS with 15 μm pitch, modified with gap.

Table 4.3 The detection efficiency value of APTS chip at different charge threshold with variant substrate back bias.

Charge threshold (e)	Detection efficiency			TID
	$V_{SUB} = 0.0 \text{ V}$	$V_{SUB} = -1.2 \text{ V}$	$V_{SUB} = -4.8 \text{ V}$	
80	95.3605%	99.6518%	99.8611%	3×10^6
100	90.8441%	98.7474%	99.7218%	3×10^6
120	83.4167%	97.634%	99.5822%	3×10^6
140	75.9657%	95.5525%	99.1626%	3×10^6
180	57.2552%	89.4993%	97.8382%	3×10^6
200	48.3202%	85.8131%	97.067%	3×10^6
250	34.0746%	74.0484%	93.3054%	3×10^6

4.3.4 Spatial resolution and average cluster size

At lower charge thresholds (80–100 electrons), the spatial resolution remains around $3.7 \mu\text{m}$ at $V_{SUB} = 0.0 \text{ V}$ and gradually decreases as V_{SUB} increases (-1.2 V, -4.8 V). This indicates that increasing the substrate voltage improves spatial resolution. The average cluster size is consistently smaller at higher V_{SUB} values. At 80 electrons, for instance, the cluster size at $V_{SUB} = 0.0 \text{ V}$ is 1.137, while at $V_{SUB} = -4.8 \text{ V}$, it's 1.236, showing a slight increase with voltage.

As the charge threshold increases, the spatial resolution becomes more stable. However, the resolution at $V_{SUB} = 4.8 \text{ V}$ is noticeably better than at $V_{SUB} = 0.0 \text{ V}$ or $V_{SUB} = 1.2 \text{ V}$. The average cluster size decreases, reflecting better localization of hits in the sensor.

As the charge threshold increases beyond 100 electrons, the spatial resolution tends to degrade, primarily due to the reduction in average cluster size. This decrease happens because higher thresholds block out signals with lower energy. This means that fewer hits are found, which can make it harder to pinpoint exactly where particles interact. In turn, this causes the spatial resolution to degrade as fewer pixels are involved in detecting the event. These trends in spatial resolution and average cluster size as a function of charge threshold and substrate voltage are summarized in Figure 4.12.

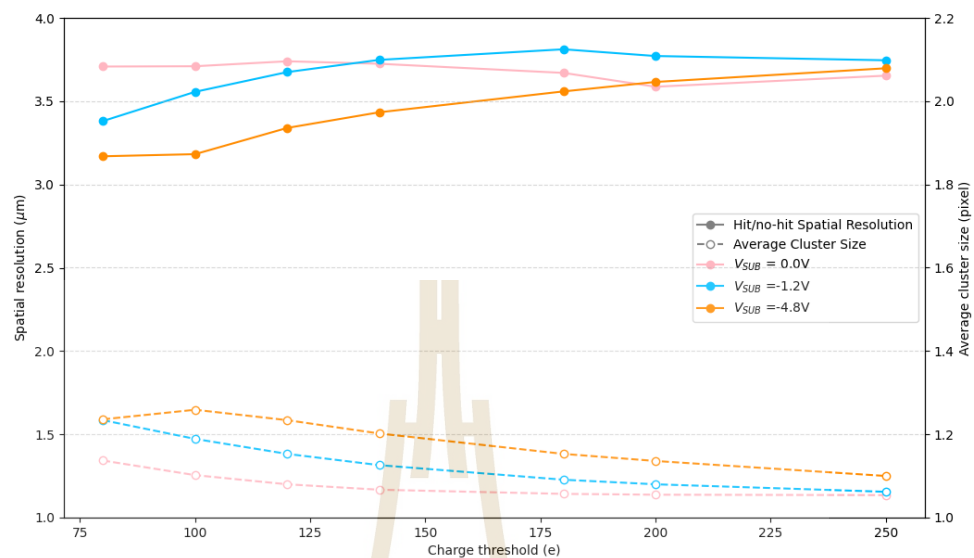


Figure 4.12 The spatial resolution (solid lines) and average cluster size (dashed lines) at different charge threshold with variant substrate back bias.

4.4 Summary

The trend in detection efficiency emphasizes the importance of substrate bias in increasing charge collection. At greater negative substrate biases, the depletion area expands, allowing for more efficient collection of charge carriers created by ionizing particles. At higher thresholds, the detection efficiency drops due to the absence of weaker signals, while lower thresholds could result in noise. The efficiency improvement with increased negative substrate bias highlights the importance of achieving a well-optimized electric field for effective charge collection.

At a charge threshold of 100 electrons, the detection efficiency shows a significant dependence on the substrate bias (V_{SUB}). At $V_{SUB} = 0.0$ V, the efficiency is relatively low ($90.84\% \pm 0.78\%$) due to insufficient depletion region, which limits charge collection and leads to recombination losses. Increasing the substrate bias to $V_{SUB} = -1.2$ V substantially improves the efficiency to $98.75\% \pm 0.29\%$, as the enlarged depletion region enhances charge collection and reduces recombination. At $V_{SUB} = -4.8$ V, the efficiency reaches $99.72\% \pm 0.13\%$, demonstrating near-complete charge collection and excellent performance.

The operation of the chip at lower thresholds increases the number of detected hits, improving the detector's overall efficiency and resolution. The lower threshold value allows more charge to be captured per hit, ensuring that even low-energy interactions are accurately recorded, which improves both the spatial resolution and efficiency. However, once the threshold is set too high, fewer hits are detected, which lowers the efficiency and increases the uncertainty in hit localization, thus degrading the spatial resolution. Therefore, the optimal operating condition for a sensor is one where the threshold is low enough to detect a majority of true hits while maintaining a high spatial resolution, balancing both detection efficiency and resolution precision.



CHAPTER V

SIMULATION OF CHARGE COLLECTION PROCESS IN MAPS

The simulation process is important to provide the prediction for the experiment. This chapter provides a simulation of the pixel sensor telescope based on the experiment that will be tested at SLRI-BTF. The G4beamline simulation used for this work is based on GEANT4. G4beamline is a particle simulation that is used to optimize and design beam lines and particle detectors. It can realistically simulate particle trajectories in the electromagnetic field and matter.

5.1 G4Beamline simulation

G4Beamline is a powerful software tool used for simulating particle beams and interactions in experimental setups (Roberts et al., 2008), particularly in high-energy physics. It is built on the Geant4 simulation toolkit (Agostinelli, S., Allison, J., Amako, K., Apostolakis, J., Araujo, H., Arce, P., . . . Zschiesche, D., 2003), which is widely used for simulating the passage of particles through matter. G4Beamline is designed specifically for beamline simulations, offering tools for modeling the particle beam transport, focusing elements, detectors, and other components in experimental setups.

G4Beamline is a specialized software tool built on the Geant4 framework, designed for simulating particle beams and interactions in high-energy physics experiments. It offers a comprehensive set of tools for modeling beamline components, such as magnets, collimators, and drift spaces, which are essential for steering and shaping particle beams. G4Beamline enables detailed particle tracking, providing precise simulations of particle propagation through various materials and fields. It also allows for custom experimental setups, where users can design geometries, define detector systems, and configure field elements. Additionally, G4Beamline's integration with Geant4 ensures access to a wide range of physics libraries, enabling simulations of particle interactions, energy deposition, and tracking in matter. The software also allows for the definition of various beam characteristics, such as energy, particle type, and spatial distribution.

5.2 Simulation Process with G4Beamline

The simulation begins by defining the electron beam characteristics. The electron beam is accelerated to an energy of 1.2 GeV and has a Gaussian distribution in the transverse plane with a full width at half maximum (FWHM) of 0.5 cm, representing the beam's spatial spread. Additionally, the energy distribution of the beam is specified with a FWHM of 60 MeV, which models the energy fluctuations typical of high-energy particle beams. These characteristics are crucial for accurately simulating the beam's interactions with the silicon sensors and ensuring that the resulting data reflect realistic conditions, including beam divergence and energy spread.

In the part of the simulation involving the silicon sensor, seven detectors are created to model the experimental setup. These detectors are designed as silicon-based sensors, with properties such as an atomic number of 14, an atomic mass of 28.0855 g.mol⁻¹, and a density of 2.57 g.cm⁻³. These values are chosen to match the physical characteristics of the silicon material used in the real experimental setup. The detectors are arranged as a pixel sensor telescope, where six ALPIDE sensors are positioned around one APTS sensor, which serves as the Device Under Test (DUT) placed in the middle. The distance between each plane is 25 mm along the z-axis.

The ALPIDE sensors used in this simulation have a thickness of 50 μm , which is composed of two layers: a 25 μm epitaxial layer of silicon and a 25 μm substrate layer. The APTS sensor, placed in the middle, has a different thickness profile, with a 10 μm epitaxial silicon layer and a 15 μm substrate. These specifications are important for simulating the sensor's response to the passing electron beam, as the thickness and structure of the sensors influence the charge collection efficiency and the detection of particle hits. Figure 5.1 shows the simulation models of the 1.2 GeV electron beam through the pixel sensor telescope, capturing energy deposition, charge collection, and the resulting pixel hits. This setup enables the study of key parameters such as cluster size, which is crucial for evaluating the performance and resolution of the MAPS detectors in detecting charged particles.

5.3 Data Flow for Digitizing and Analyzing Sensor Data

The data flow for digitizing and analyzing sensor data from the ALPIDE sensor simulations follows a systematic and structured process, starting from the G4Beamline simulation and progressing through various stages of data processing, calculation, and

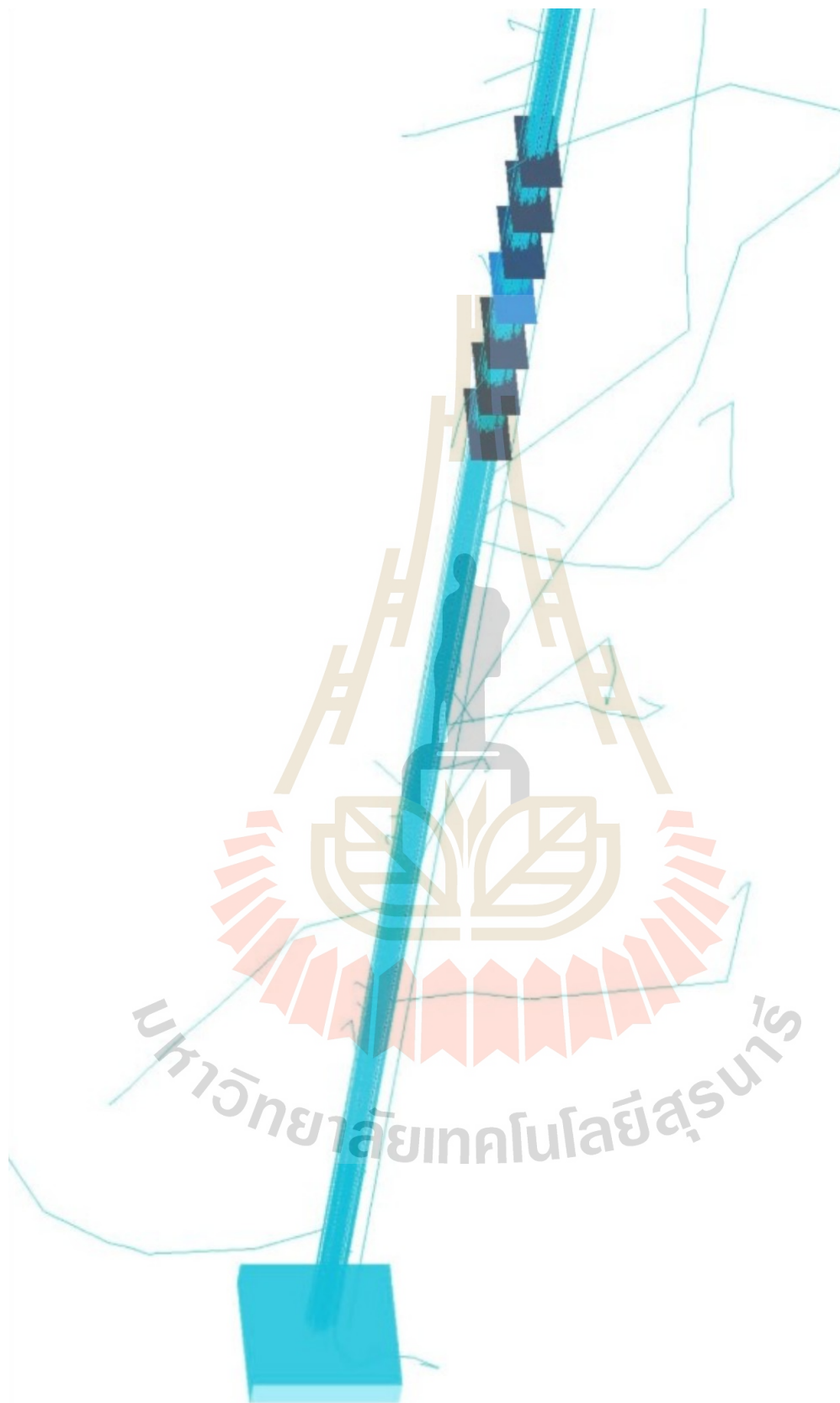


Figure 5.1 The simulation of 1.2 GeV electron beam passing through a pixel sensor telescope, and consisting of six silicon sensors as reference planes and one APTS chip as DUT.

analysis. Below is a detailed description of each step:

1. **Start:** The process starts from the G4Beamline simulation, where the particle beam is propagated through the experimental setup, and the interactions with the silicon sensors are simulated.
2. **Open ROOT File:** The ROOT file, which contains the simulation outputs from the ALPIDE sensors, is opened. This file includes the hit data corresponding to the electron beam's interaction with the sensors.
3. **Loop Over Detector Layers:** The program iterates over each detector layer to process the hits recorded by the sensors. Each layer is analyzed individually to extract relevant information, such as pixel positions, for further calculation.
4. **Path Calculation:** In this step, the particle's path within the sensor is calculated. The interaction points, including the entry (hitIn) and exit (hitOut) positions, are computed. The method *calculatePathInPixelLengths()* is used to calculate the particle's trajectory through each pixel in the detector layers.
5. **Charge Deposition:** The Linear Energy Transfer (LET) of the particle passing through the sensor is estimated based on the energy deposition (E_{dep}) and the calculated path. This LET value is then converted into electron-hole pairs, which are proportional to the energy deposited in the silicon material.
6. **Charge Diffusion:** After charge deposition, the charge carriers diffuse across the sensor. The pixel intensity map is created by considering both the direct and indirect contributions of ionized electrons in the epitaxial layer along the particle's path. This map simulates the spread of the charge carriers as they move through the sensor.
7. **Cluster Formation:** The charge distribution from the pixel intensity map is used to group nearby pixels into clusters. A clustering threshold is applied based on spatial proximity and intensity values to form meaningful clusters of hit pixels.
8. **Histogram Storage:** The processed data, including the sensor hitmap and cluster size distribution, is stored in histograms. These histograms facilitate further analysis and visualization of the sensor's performance.

9. **End:** The data flow concludes, and the results are saved for further examination or statistical analysis.

5.4 Results

This section provides analysis results of the simulation from G4Beamline, which provides insights into the behavior and performance of the ALPIDE sensors under the 1.2 GeV electron beam. The results include an analysis of the beam profile, energy deposition, and cluster size, which are key metrics for evaluating the performance of the sensors in detecting and tracking particles. The beam profile is examined to assess the spatial distribution of the electron beam as it interacts with the sensors. Energy deposition is analyzed to understand how the energy from the electron beam is transferred to the silicon material, and how this energy is subsequently converted into electron-hole pairs. Finally, the cluster size distribution is studied to evaluate the effectiveness of the sensor in grouping adjacent pixels triggered by a single particle, providing insight into the resolution and sensitivity of the detector system. These results form the basis for further performance optimization and comparison with experimental data.

5.4.1 Hitmap

The 2D beam profile was analyzed by plotting the x and y positions of the electron beam hits, with the sensor dimensions set to 1024 pixels by 512 pixels. The 1.2 GeV electron beam used in the simulation was generated with a Gaussian distribution, having a full width at half maximum (FWHM) of 0.5 cm in the transverse plane, and a 60 MeV FWHM in energy. A total of 5,000 electrons were generated for the simulation. The resulting beam profile, shown in Figure 5.2, represents the electron hit map in both the x and y coordinates. This hit map visualizes the spatial distribution of the beam as it interacts with the detector, providing a clear view of the beam's spread and intensity within the sensor area. The beam profile is essential for understanding the beam's behavior and alignment in the experimental setup, and it serves as a reference for further analysis of energy deposition and cluster formation.

5.4.2 Energy deposit

The energy deposition in the sensor is an essential factor in understanding how the electron beam interacts with the silicon material of the ALPIDE sensors. Figure

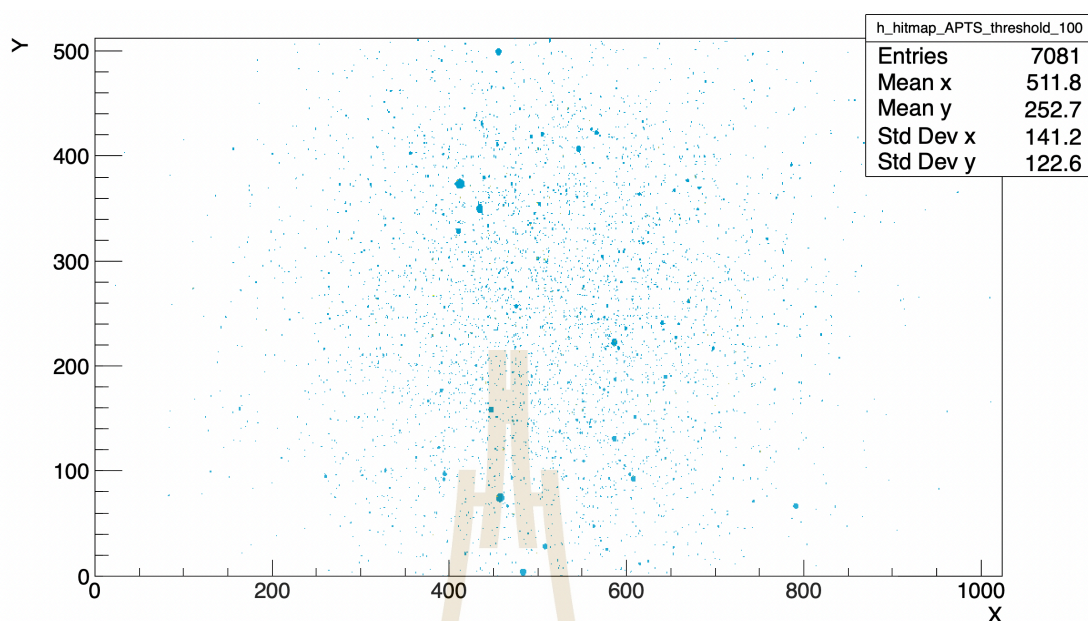


Figure 5.2 Beam profile on ALPIDE sensor in the case of a charge threshold of 100 electrons. The beam profile is performed by using G4beamline software to do a simulation and using ROOT to analyze for analysis process.

5.3 shows the histogram of energy deposition (E_{dep}) for the 1.2 GeV electron beam simulated through the sensors. The energy deposition distribution is sparse, with the majority of energy deposited in small amounts across the sensor, as shown by the peak in the lower energy range.

From the histogram, we can observe that the energy deposition primarily falls within a narrow range, with a mean value of 0.00291 GeV and a standard deviation of 0.002742 GeV. This distribution reflects how the energy of the electron beam is transferred to the silicon material, with the majority of the energy being absorbed by the sensor in small, discrete portions. The spread of energy deposition values can be attributed to variations in the path and interactions of the individual electrons as they traverse through the sensor.

5.4.3 Energy to Electron-Hole Pair Conversion

The energy deposited in the sensor, E_{dep} , is converted into electron-hole pairs based on the energy required to create a single electron-hole pair in the silicon material. For silicon, this energy is approximately 3.6 eV. The number of electron-hole

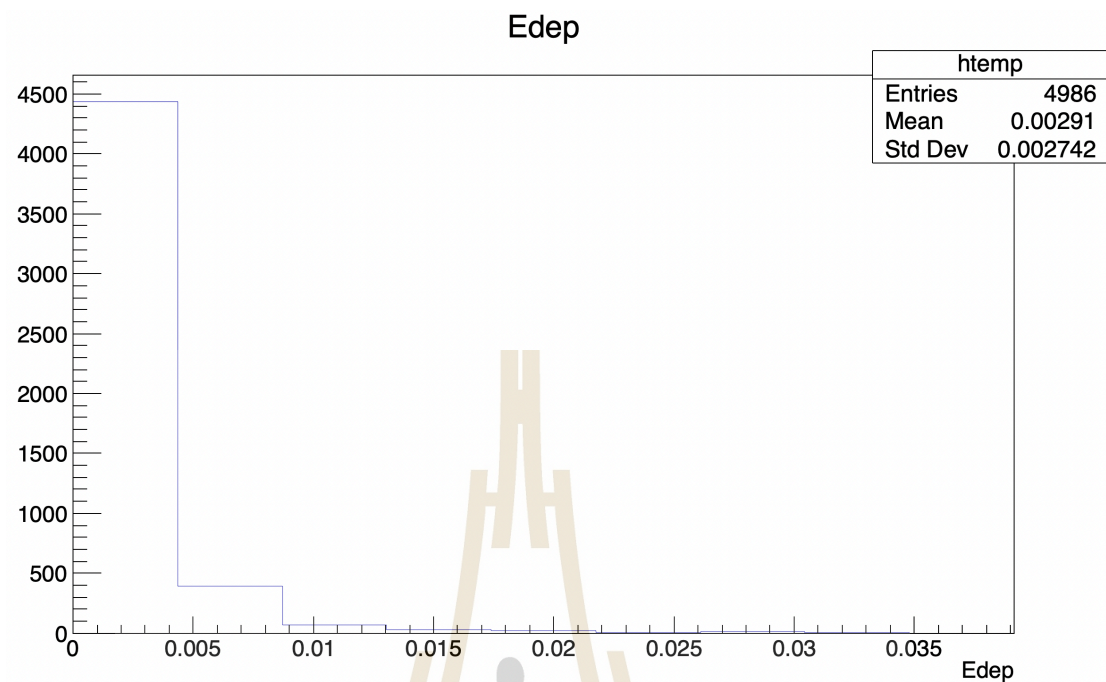


Figure 5.3 Distribution of energy deposit (E_{dep}) of 1.2 GeV electron beam on APTS sensor.

pairs generated can be calculated using the following equation:

$$\text{Number of electron-hole pairs} = \frac{E_{\text{dep}}}{\text{Energy per electron-hole pair}},$$

where E_{dep} is the energy deposited in the sensor (in eV), The energy per electron-hole pair for silicon is approximately 3.6 eV.

For example, with an energy deposition of 0.00291 GeV (or 2.91 MeV), the number of electron-hole pairs can be calculated as:

$$\text{Number of electron-hole pairs} = \frac{0.00291 \times 10^9}{3.6} \approx 808,333 \text{ pairs.}$$

This calculation is important for understanding how the energy deposited by the electron beam is transformed into detectable charge carriers, which are then used for further processes like charge diffusion and clustering.

5.4.4 Cluster size

In this subsection, we investigate the behavior of cluster size in the simulation, as it depends on the charge threshold (in electrons). The cluster size represents the number of adjacent pixels triggered by a single particle passing through the sensor. We study how the cluster size varies with different charge threshold values, which are set to 80, 100, 120, 140, 180, 200, and 250 electrons. The charge threshold determines the minimum amount of charge required for a pixel to be considered part of a cluster.

Figures 5.4, C.4, and 5.6 show the cluster size distributions for three different charge thresholds: 80, 100, and 250 electrons. These distributions provide insight into the pixel grouping behavior for different thresholds. As the threshold increases, fewer pixels meet the charge requirements to form a cluster, leading to smaller cluster sizes. This trend is observed across the different charge thresholds.

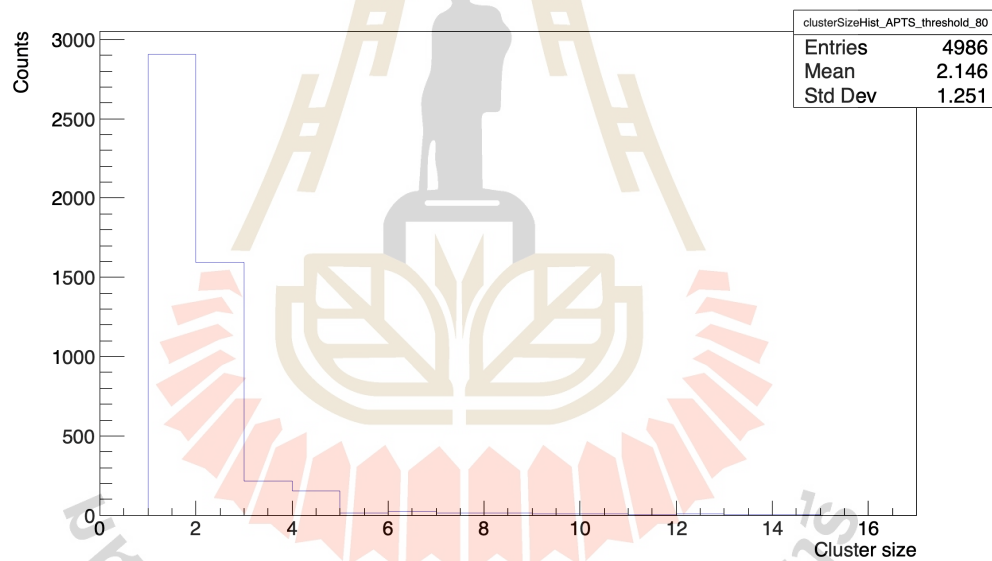


Figure 5.4 Cluster size distribution for a charge threshold of 80 electrons.

In addition, Figure 5.7 illustrates the relationship between the average cluster size and the charge threshold. As the charge threshold increases from 80 to 250 electrons, the average cluster size decreases, as higher thresholds require a higher amount of charge for clustering, reducing the number of clustered pixels.

These results demonstrate the influence of the charge threshold on the cluster size, which is a key factor in optimizing sensor performance for detecting and tracking charged particles. Understanding this relationship helps in determining the optimal

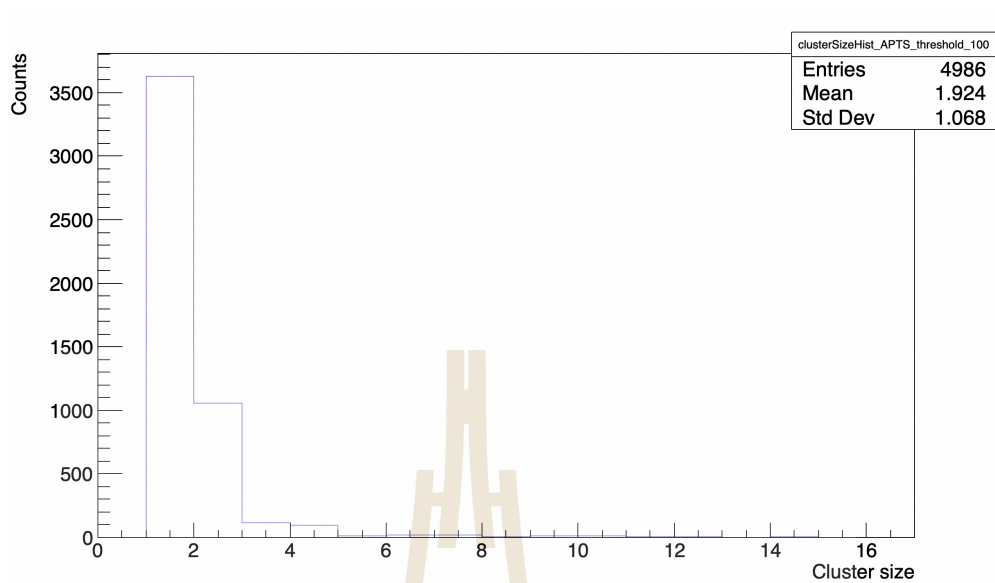


Figure 5.5 Cluster size distribution for a charge threshold of 100 electrons.

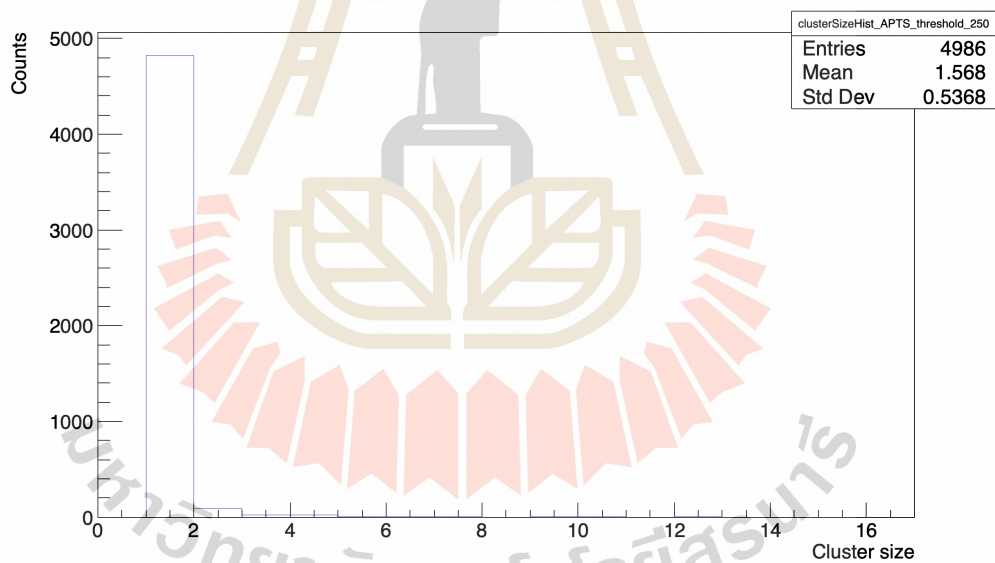


Figure 5.6 Cluster size distribution for a charge threshold of 250 electrons.

threshold value for different experimental conditions.

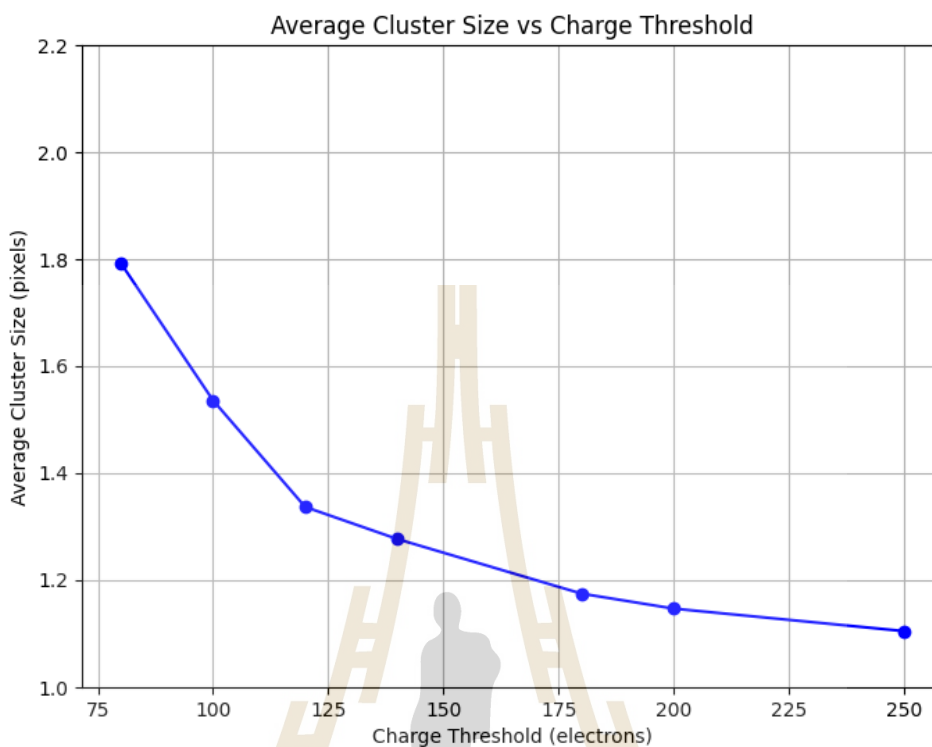


Figure 5.7 Average cluster size vs. charge threshold. This plot shows how the average cluster size decreases as the charge threshold increases from 80 to 250 electrons, indicating that higher thresholds require more charge to trigger a cluster, demonstrating that as the threshold rises, the number of detected pixels per cluster decreases.

5.4.5 Summary

The results of the simulation provided insights into the beam profile, energy deposition, and the dependence of cluster size on charge threshold. The beam profile analysis revealed the spatial distribution of electron hits on the sensor, confirming the Gaussian nature of the beam. The energy deposition study demonstrated how the beam interacts with the silicon sensor, where the deposited energy was converted into electron-hole pairs. This charge was then diffused within the silicon material, contributing to the clustering of pixels.

A key aspect of the study was the investigation of cluster size as a function of charge threshold. By varying the charge threshold from 80 to 250 electrons, we observed a clear inverse relationship between the charge threshold and the average

cluster size. As the threshold increased, fewer pixels contributed to clustering, leading to smaller clusters. This trend was confirmed by analyzing cluster size distributions at different charge thresholds and a summary plot showing the dependence of the average cluster size on the charge threshold.

These findings are crucial for optimizing the sensor's performance in particle tracking applications. The choice of charge threshold significantly impacts the spatial resolution and efficiency of the detector. The results from this study serve as a reference for tuning the sensor parameters to achieve the best trade-off between spatial resolution and detection efficiency for future experiments.



CHAPTER VI

SUMMARY AND CONCLUSION

This thesis titled “INVESTIGATION OF MONOLITHIC ACTIVE PIXEL SENSOR” has explored the advancements in Monolithic Active Pixel Sensors (MAPS) and their applications in high-energy physics experiments. The research presented covers fundamental semiconductor physics, sensor architecture, experimental validation through beam tests, and detailed simulations of charge collection processes.

The 65nm CMOS imaging process technology is the basis of the new sensor prototype; the first submission is called “Multi Layer Reticle 1 (MLR1)”. The deep p-well implant is the most important part of the sensor prototype. It can create an active area in the silicon layer without getting in the way of the deposited charge collection. It also uses the new technology, known as “stitching”, to create a large sensor ($14 \times 14 \text{ cm}^2$) with very low thickness. The sensor prototype will be developed for the ALICE upgrade, called ITS3. The main upgrade is to reduce the layer materials; a material budget was reduced to 0.05% X_0 per layer. The new beam pipe will be installed with a thinner profile of $500 \mu\text{m}$ and a lower radius of 16 mm. The goal is to achieve Pb-Pb interaction readout speeds faster than 50 kHz. The vertexing and tracking performance will reach to detect the low transverse momentum ($p_T < 1 \text{ GeV}/c$).

This work is focusing on one of the MLR1 prototypes, called “Analog Pixel Test Structure—Source Follower (APTS SF)”. The main feature of APTS is a high-speed analog readout. The chip was studied in the laboratory test to check and observe the sensor performance. To observe the pulsing signal behavior, the sensor was optimized on the variant pulsing bias voltage (V_H) with the different substrate bias voltage (V_{BB}). We can achieve the highest maximum amplitude by applying more V_H and higher V_{BB} . The proper trigger threshold was achieved by optimizing the balancing of the background noise value and data-collection time. After receiving the proper trigger threshold, this value was set for the source scan measurement. The goal is to measure the sensor’s accurate particle detection. Iron-55 (^{55}Fe) was used in this work as a radioactive source, releasing a low-energy gamma ray. The APTS chip was tested with ^{55}Fe at different V_{BB} , and the results were compared with a reference chip. However, no clear difference was achieved for the different V_{BB} . The charge collection efficiency (CCE) has no ma-

major impact; only the sensor operation at V_{BB} of 0V provides a higher CCE. The sensor performances were also observed at different temperatures, starting at 10 - 60 degrees Celsius. Nevertheless, there is no significant difference in the CCE. A further laboratory test is to examine the radiation hardness of the sensor. The APTS chip was mounted and exposed to irradiation with a 70 MeV proton beam at KCMH with a total ionizing dose of 100 krad and 500 krad. The non-irradiated chip has CCE when operated at $V_{BB} = 0V$. An increased quantity of TID dosages results in a reduction in CCE.

Test beam measurement is one of the sensor characterizations. The Siam Photon Source (SPS) provides synchrotron radiation with a 1.2 GeV electron beam. The Beam Test Facility (SLRI-BTF) is a station for beam characterization, located next to the vertical bending magnet. The SLRI-BTF can yield fewer than 10 electrons per repetition rate by manipulating a tungsten target, positioned at the end of LBT. You can also change the energy selection at SLRI-BTF by changing the ramping times, which are linked to the magnet current. The pixel sensor telescope consists of six ALPIDE sensors, with one APTS chip positioned centrally among three ALPIDE sensors. This setup was installed at the SLRI-BTF for the aim of APTS characterization. The 1.2 GeV electron beam was used for this work. Data collection and observation were performed by the EUDAQ2 software, implemented using the C++ programming language. The output of the EUDAQ2 is generated as event-by-event data as a RAW binary file.

The test beam data from the Super Proton Synchrotron (SPS) was considered in this work. The APTS chip was irradiated with 300 Mrad TID and tested under a 120 GeV pion beam. The goal is to achieve the detection efficiency and spatial resolution of the APTS chip. Corryvreckan software was used for all analysis methods and the analysis framework for test beam measurement. The DUT was considered under the variant charge threshold of 80, 100, 120, 140, 180, 200, and 250 electrons. The detection efficiency and spatial resolution have been determined by associating the DUT cluster with a window that has a radius of $75 \mu m$. The detection efficiency can reach 99% even if the chip was irradiated with a high TID dose. The APTS operation with a substrate bias of -4.8 V achieves optimal efficiency at a charge threshold of 100 electrons. As the charge threshold increases, the spatial resolution improves. Optimal operating conditions are required to balance detection efficiency and spatial resolution. The operation at a substrate bias voltage of -4.8 V yields nearly full charge collection and exceptional performance.



REFERENCES

มหาวิทยาลัยเทคโนโลยีสุรนารี

REFERENCES

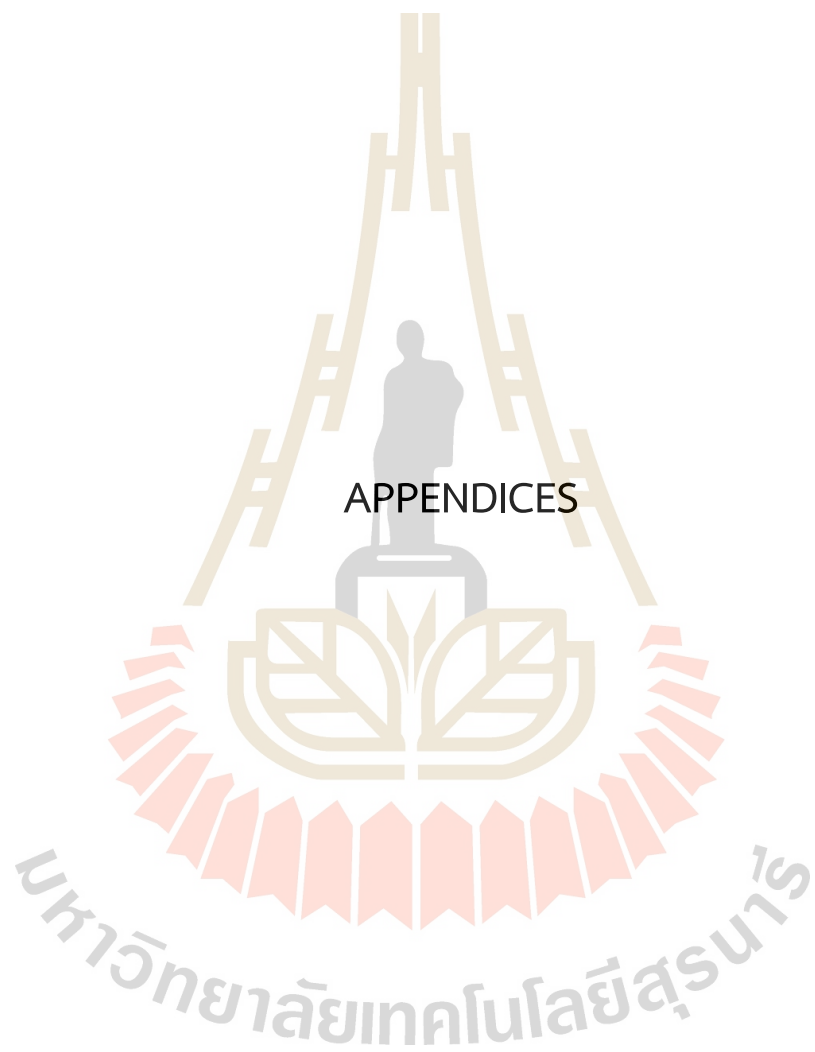
- Abelev, B., Adam, J., Adamová, D., Aggarwal, M. M., Aglieri Rinella, G., Agnello, M., . . . Zyzak, M. (2014). Technical design report for the upgrade of the alice inner tracking system. *Journal of Physics G: Nuclear and Particle Physics*, 41(8), 087002.
- Agostinelli, S., Allison, J., Amako, K., Apostolakis, J., Araujo, H., Arce, P., . . . Zschesche, D. (2003). Geant4—a simulation toolkit. *Nuclear Instrument Method A*, 506(3), 250-303.
- Antonioli, P., Kluge, A., and Riegler, W. (2013). *Upgrade of the ALICE Readout & Trigger System* (cern-lhcc-2013-019). Retrieved from Research on Poverty Alleviation website: <https://cds.cern.ch/record/1603472>.
- Apadula, N., Armstrong, W., Brau, J., Breidenbach, M., Caputo, R., Carinii, G., . . . Zurek, Z. (2022). Monolithic active pixel sensors on cmos technologies. *The Proceedings of the US Community Study on the Future of Particle Physics*, (2203.07626). USA: Snowmass.
- Bai, Y. and Long, A. J. (2018). Six flavor quark matter. *Journal of High Energy Physics*, 2018(6), 1029–8479.
- Banerjee, D., Bernhard, J., Brugger, M., Charitonidis, N., Doble, N., Gatignon, L., Gerbershagen, A. (2021). *The North Experimental Area at the Cern Super Proton Synchrotron* (CERN-ACC-NOTE-2021-0015). Retrieved from Research on Poverty Alleviation website: <https://cds.cern.ch/record/2774716>.
- Bartschat, K. (1989). Excitation and ionization of atoms by interaction with electrons, positrons, protons and photons. *Physics Reports*, 18(1), 1–81.
- Biesdorf, C., Menezes, D. P., and Lopes, L. L. (2023). Qcd phase diagrams via qhd and mit-based models. *Brazilian Journal of Physics*, 53(5).
- Blobel, V. (2006). A new fast track-fit algorithm based on broken lines. *Nuclear Instruments and Methods in Physics Research Section A: Accelerators, Spectrometers, Detectors and Associated Equipment*, 566(1), 14–17.

- Buballa, M. (2005). Njl-model analysis of dense quark matter. *Physics Reports*, 407(4), 205–376.
- Buncic, P., Krzewicki, M., and Vande Vyvre, P. (2015). *Technical Design Report for the Upgrade of the Online-Offline Computing System* (ALICE-TDR-019). Retrieved from Research on Poverty Alleviation website: <https://cds.cern.ch/record/2011297>.
- Carnesecchi, F., Sabiu, B., Strazzi, S., Vignola, G., Agrawal, N., Alici, A., . . . Zichichi, A. (2023). Measurements of the cherenkov effect in direct detection of charged particles with sipms. *Eur. Phys. J. Plus*, 138(788).
- Collaboration, A. (2015). *Addendum to the Technical Design Report for the Upgrade of the ALICE Time Projection Chamber* (CERN-LHCC-2015-002). Retrieved from Research on Poverty Alleviation website: <https://cds.cern.ch/record/1984329>.
- collaboration, T. A. (2024). Technical Design report for the ALICE Inner Tracking System 3 - ITS3 ; A bent wafer-scale monolithic pixel detector.
- Cussans, D. (2009). *Description of the JRA1 Trigger Logic Unit (TLU), v0.2c* (eudet-memo-2009-4). . Retrieved from Research on Poverty Alleviation website: <https://api.semanticscholar.org/CorpusID:61414353>.
- Dannheim, D., Dort, K., Huth, L., Hynds, D., Kremastiotis, I., Kröger, J., . . . Williams, M. (2021). Corryvreckan: a modular 4d track reconstruction and analysis software for test beam data. *Journal of Instrumentation*, 16(3), P03008.
- Dorokhov, A., Bertolone, G., Baudot, J., Colledani, C., Claus, G., Degerli, Y., . . . Winter, M. (2011). High resistivity cmos pixel sensors and their application to the star pxl detector. *Nuclear Instruments and Methods in Physics Research Section A: Accelerators, Spectrometers, Detectors and Associated Equipment*, 650(1), 174–177.
- Essig, R., Plestid, R., and Singal, A. (2024). Collective excitations and low-energy ionization signatures of relativistic particles in silicon detectors. *Commun. Phys.*, 7(1), 416.
- Gray, H. M. (2024). LHC Experiments. *Theoretical Advanced Study Institute in Particle Theory, (TASI2022)*, USA: TASI.

- Heinz, U. and Jacob, M. (2000). *Evidence for a New State of Matter: An Assessment of the Results from the CERN Lead Beam Programme*. Retrieved from Research on Poverty Alleviation website: <https://arxiv.org/abs/nucl-th/0002042>.
- Hu-Guo, C., Baudot, J., Bertolone, G., Besson, A., and Brogna, A. (2010). First reticule size maps with digital output and integrated zero suppression for the eudet-jra1 beam telescope. *Nuclear Instruments and Methods in Physics Research Section A: Accelerators, Spectrometers, Detectors and Associated Equipment*, 623(1), 480–482.
- Jakubassa-Amundsen, D. H. (2021). *Advances in bremsstrahlung: a review*. Retrieved from Research on Poverty Alleviation website: <https://arxiv.org/abs/2103.06034>.
- Jansen, H., Spannagel, S., Bulgheroni, A., Claus, G., Claus, G., Corrin, E., . . . Winter, M. (2016). Performance of the eudet-type beam telescopes. *EPJ Techniques and Instrumentation*, 3(7), 33.
- Kaewjai, J., Kobdaj, C., and Kittimanapun, K. (2019). Upgrade of pixel sensor telescope for the characterization of alpine sensor. *Journal of Physics: Conference Series*, 1380(1), 012126.
- Kittimanapun, K., Chanlek, N., Juntong, N., Cheedket, S., Klysubun, P., and Supajeerapan, S. (2017). IMPROVEMENT OF ELECTRON INTENSITY REDUCTION SYSTEM AT SLRI BEAM TEST FACILITY. *IPAC2017, MOPIK015*, 528.
- Kittimanapun, K., Chanlek, N., Klysubun, P., Krainara, S., and Supajeerapan, S. (2016). Sri beam test facility development project. *IPAC2016, MPIK002*, 2539-41.
- Kittimanapun, K., Kaewjai, J., and Laojamnongwong, N. (2024). Energy selection of synchrotron booster for SLRI beam test facility. *IPAC2024, THPG10*.
- Kittimanapun, K., Chanlek, N., Klysubun, P., Kobdaj, C., Lakrathok, A., Laojamnongwong, N., . . . Musa, L. (2019). Development of the slri beam test facility for characterization of monolithic active pixel sensors. *Nuclear Instruments and Methods in Physics Research Section A: Accelerators, Spectrometers, Detectors and Associated Equipment*, 930, 105-111.

- Lebrun, P. (2010). *Commissioning and First Operation of the Large Hadron Collider (LHC)* (CERN-ATS-2010-178). Retrieved from Research on Poverty Alleviation website: <https://cds.cern.ch/record/1284331>.
- Mager, M. (2014). Telescope optimizer.
- Mager, M. (2016). Alpide, the monolithic active pixel sensor for the alice its upgrade. *Nuclear Instruments and Methods in Physics Research Section A: Accelerators, Spectrometers, Detectors and Associated Equipment*, 824, 434–438.
- Medenwaldt, R., Møller, S.P., Uggerhøj, E., Worm, T., Hvelplund, P., Knudsen, H., . . . Morenzoni, E. (1991). Measurement of the stopping power of silicon for antiprotons between 0.2 and 3 mev. *Nuclear Instruments and Methods in Physics Research Section B: Beam Interactions with Materials and Atoms*, 58, 1-5.
- Menezes, D. P. (2021). A neutron star is born. *Universe*, 7(8), 267.
- Meroli, S. (2015). In-depth study of phenomena characterizing the passage of ionizing particles through semiconductor layers [Online].
- Mrowczynski, S. (1999). Quark-gluon plasma. *Acta Phys. Pol.*, B29, 3711.
- Musa, L. (2019). *Letter of Intent for an ALICE ITS Upgrade in LS3* (CERN-LHCC-2019-018). Retrieved from Research on Poverty Alleviation website: <https://cds.cern.ch/record/2703140>.
- Podgorsak, E. (2009). *Interaction of Charged Particles with Matter*. USA: Springer.
- Roberts, T., Beard, K., Huang, D., Ahmed, S., and Kaplan, D. (2008). G4beamline particle tracking in matter-dominated beam lines, conf. *Proceeding Conference*, (110328). USA: PAC'11).
- Sadeghi, M., Soheibi, N., Kakavand, T., and Yarmohammadi, M. (2012). Targetry and nuclear data for the cyclotron production of ^{55}Fe via various reactions. *Journal of Radioanalytical and Nuclear Chemistry*, 293(1), 1–6.
- Salvat, F. (2022). Bethe stopping-power formula and its corrections. *Phys. Rev. A*, 106(25), 032809.

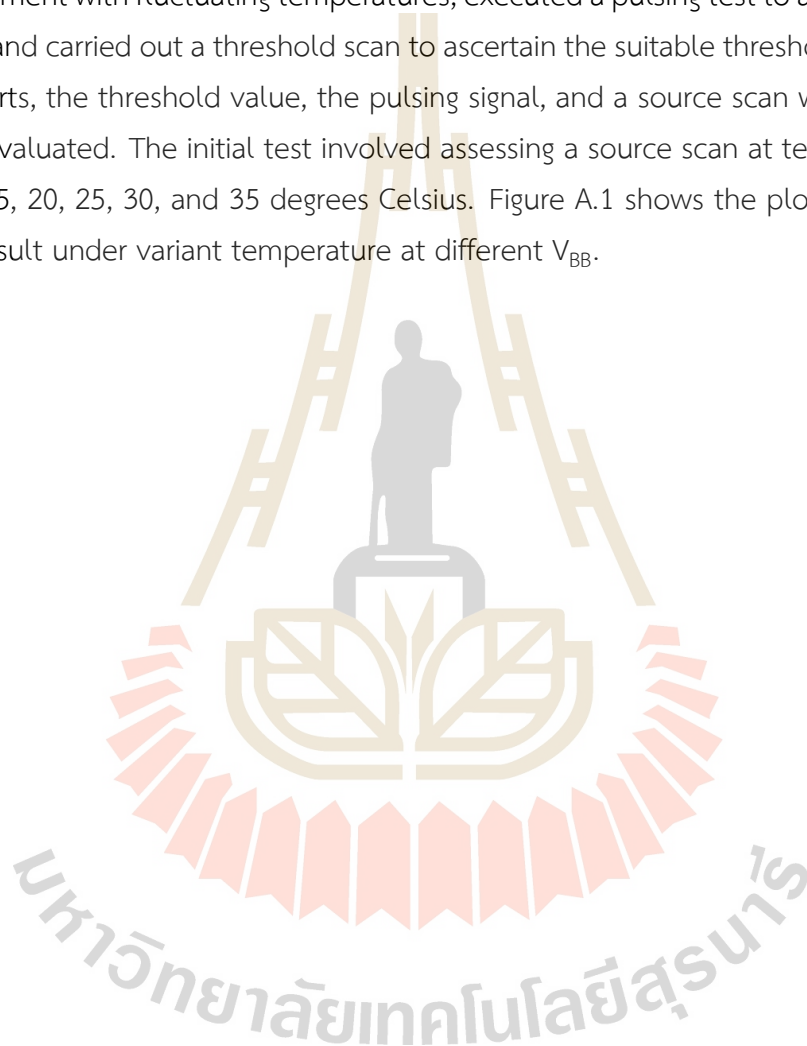
- Satz, H. (2011). The quark-gluon plasma: A short introduction. *Nucl. Phys.*, A862-863(BI-TP-2011-02), 4–12.
- Schambach, J., Anderssen, E., Contin, G., Greiner, L., Silber, J., Stezelberger, T., . . . Woodmansee, S. (2015). A maps based micro-vertex detector for the star experiment. *Physics Procedia*, 66, 514–519.
- Skands, P. (2013). Searching for new physics at small and large scales: Introduction to qcd. *WORLD SCIENTIFIC, TASI2012*, 520.
- Spannagel, S. (2016). *Test Beam Measurements for the Upgrade of the CMS Pixel Detector and Measurement of the Top Quark Mass from Differential Cross Sections* (desy-thesis-2016-010). Retrieved from Research on Poverty Alleviation website: <https://inspirehep.net/literature/1462486>.
- Turchetta, R., Fant, A., Gasiorek, P., Esbrand, C., Griffiths, J.A., Metaxas, M.G., . . . Bergamaschi, A. (2007). Cmos monolithic active pixel sensors (maps): Developments and future outlook. *Nuclear Instruments and Methods in Physics Research Section A: Accelerators, Spectrometers, Detectors and Associated Equipment*, 582(3), 866-870.
- Yagi, K., Hatsuda, T., and Miake, Y. (2005). Quark-gluon plasma: From big bang to little bang. *Camb. Monogr. Part. Phys. Nucl. Phys. Cosmol.*, 23, 1-446.



APPENDIX A

VALIDATION OF APTS WITH DIFFERENT TEMPERATURE

The objective is to verify the status of the APTS chip. We relocated it to an environment with fluctuating temperatures, executed a pulsing test to assess the sensor signal, and carried out a threshold scan to ascertain the suitable threshold. As the main test starts, the threshold value, the pulsing signal, and a source scan with ^{55}Fe are all being evaluated. The initial test involved assessing a source scan at temperatures of $T = 10, 15, 20, 25, 30,$ and 35 degrees Celsius. Figure A.1 shows the plots of the source scan result under variant temperature at different V_{BB} .



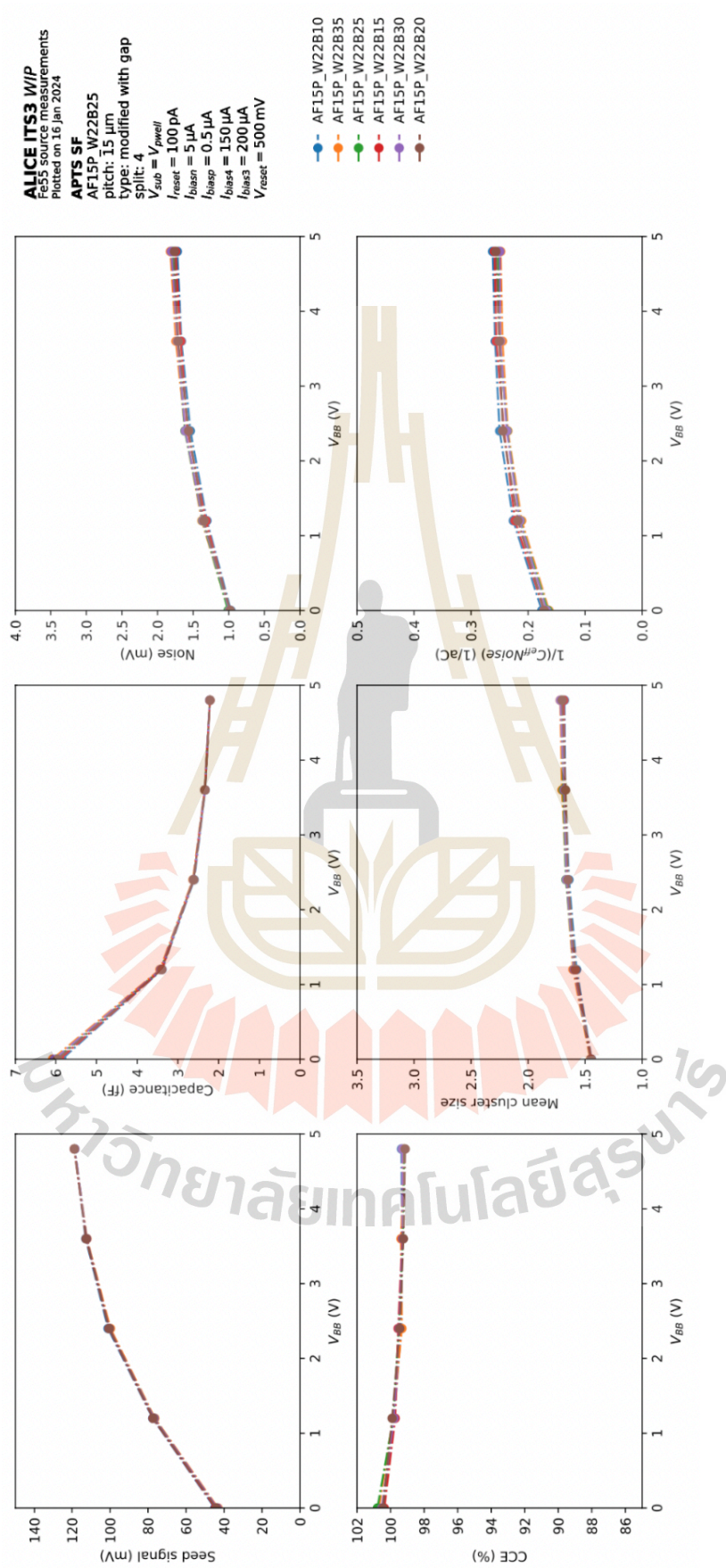


Figure A.1 APTS Source scan under low to normal temperature (10 - 35 degrees Celsius) at different substrate bias.

The below results show the validation of APTS by varying temperature $T = 60$ degree Celsius (Thermometer 60 degree Celsius).

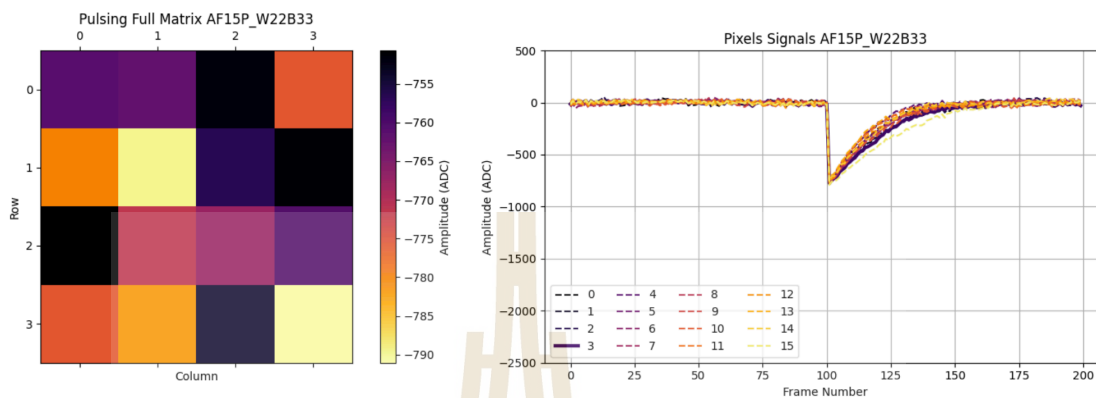


Figure A.2 Pulsing signal of 16 pixels of APTS chip at substrate bias of 0.0 V under temperature of 60 degree Celsius.

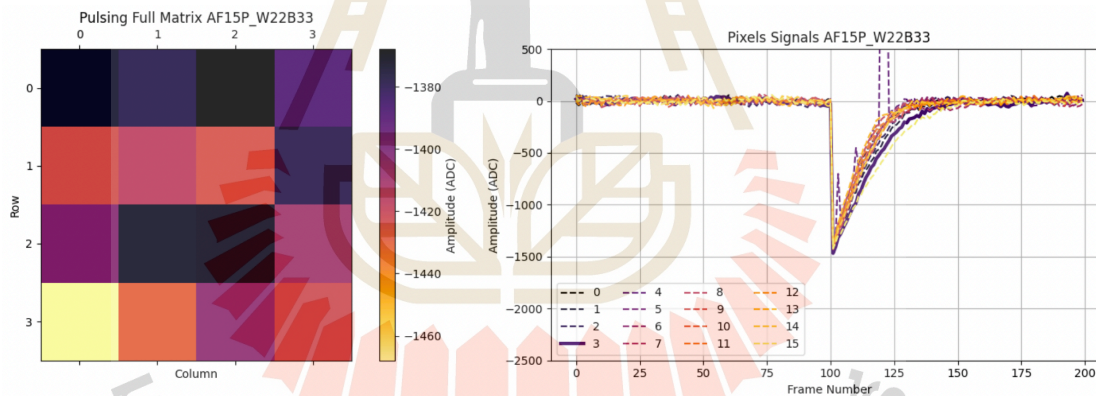


Figure A.3 Pulsing signal of 16 pixels of APTS chip at substrate bias of -1.2 V under temperature of 60 degree Celsius.

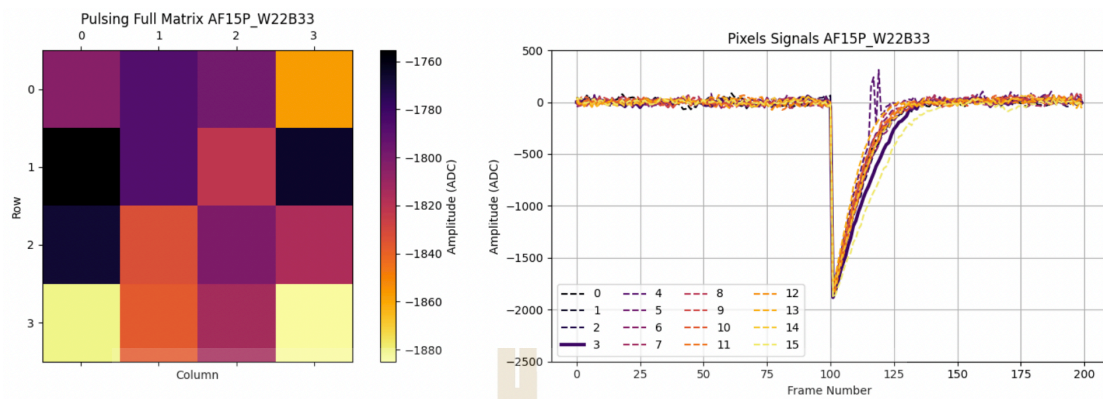


Figure A.4 Pulsing signal of 16 pixels of APTS chip at substrate bias of -2.4 V under temperature of 60 degree Celsius.

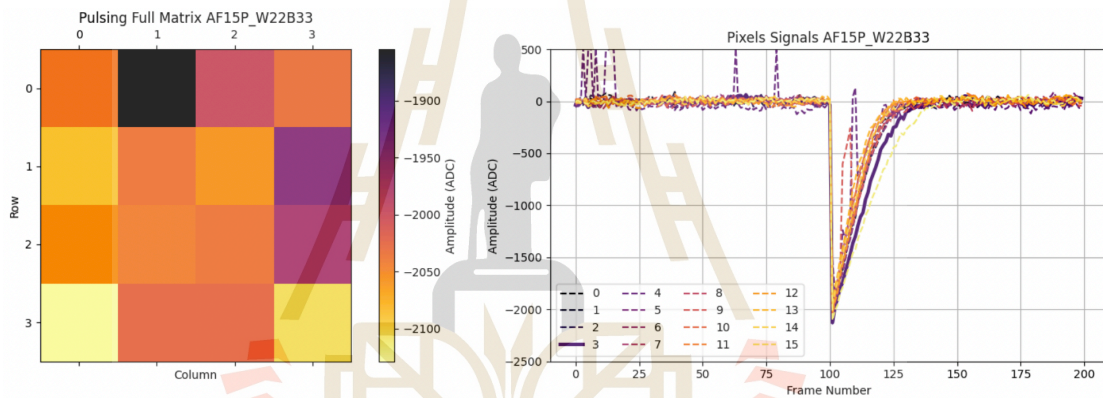


Figure A.5 Pulsing signal of 16 pixels of APTS chip at substrate bias of -3.6 V under temperature of 60 degree Celsius.

The below results show the validation of APTS by varying temperature $T = 50$ degree Celsius (Thermometer 49 degree Celsius).

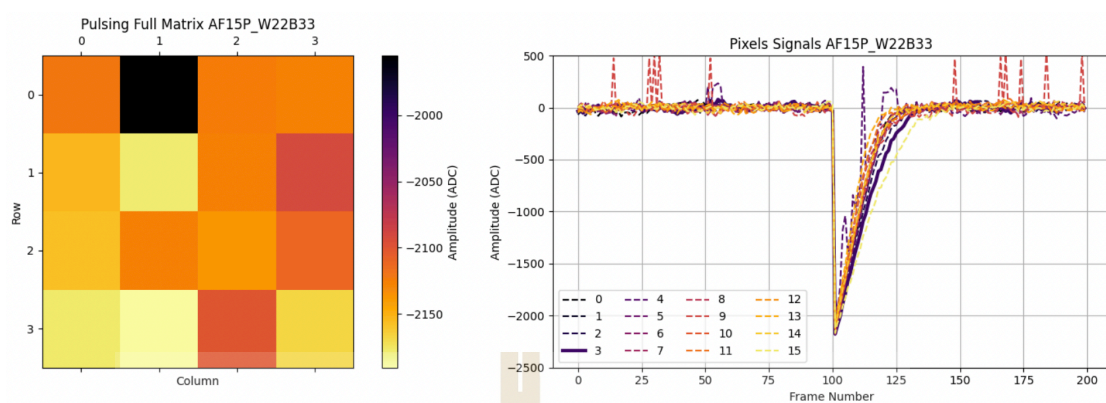


Figure A.6 Pulsing signal of 16 pixels of APTS chip at substrate bias of -4.8 V under temperature of 60 degree Celsius.

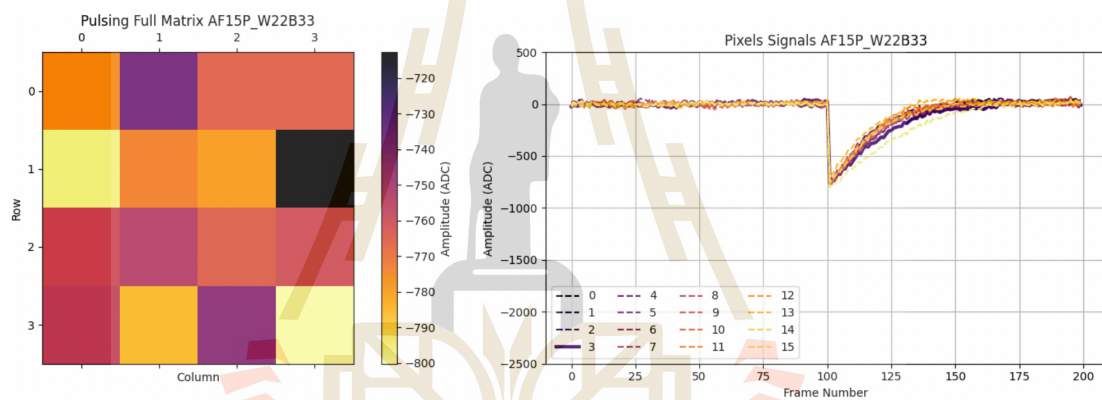


Figure A.7 Pulsing signal of 16 pixels of APTS chip at substrate bias of 0.0 V under temperature of 50 degree Celsius.

The below results show the validation of APTS by varying temperature $T = 40$ degree Celsius (Thermometer 39 degree Celsius).

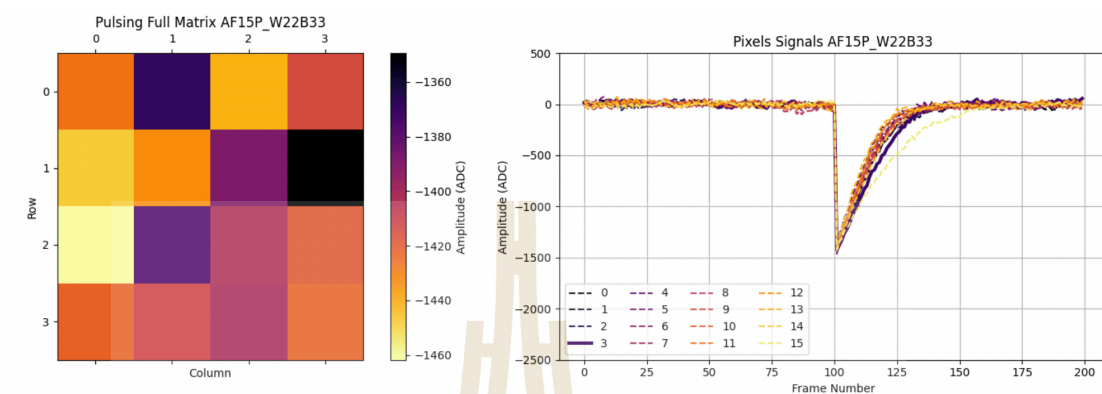


Figure A.8 Pulsing signal of 16 pixels of APTS chip at substrate bias of -1.2 V under temperature of 50 degree Celsius.

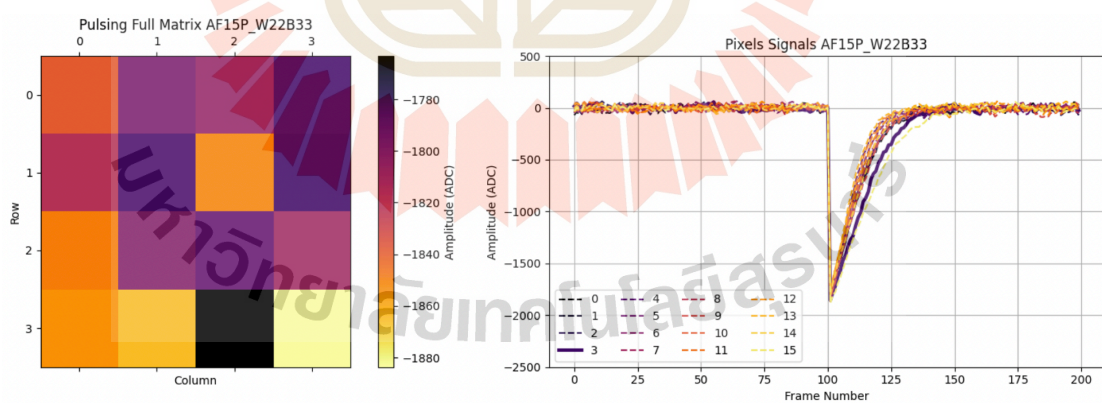


Figure A.9 Pulsing signal of 16 pixels of APTS chip at substrate bias of -2.4 V under temperature of 50 degree Celsius.

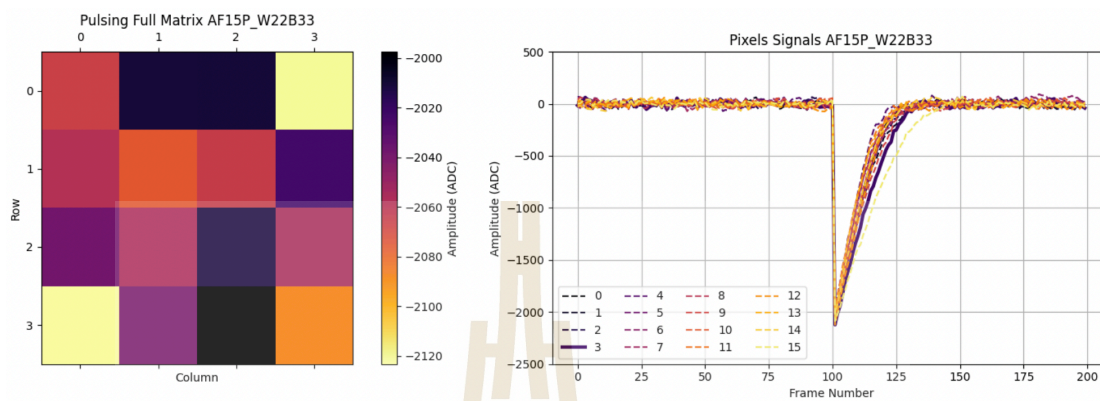


Figure A.10 Pulsing signal of 16 pixels of APTS chip at substrate bias of -3.6 V under temperature of 50 degree Celsius.

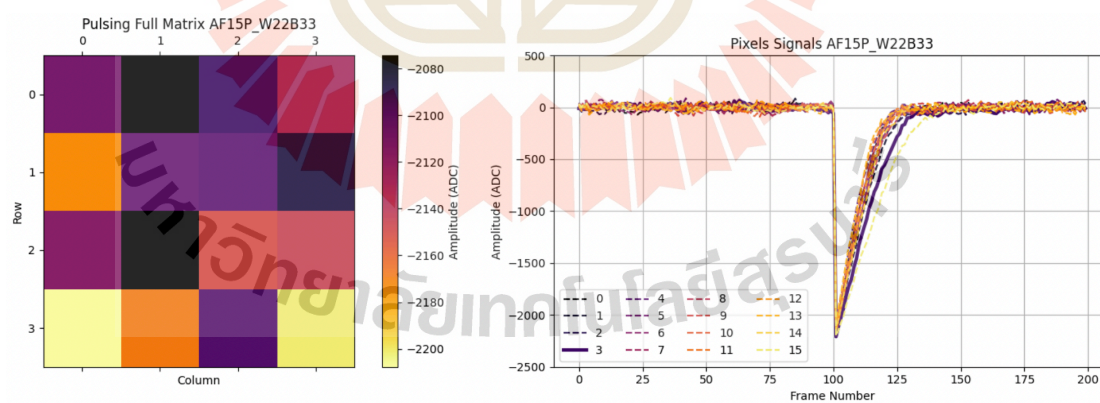


Figure A.11 Pulsing signal of 16 pixels of APTS chip at substrate bias of -4.8 V under temperature of 50 degree Celsius.

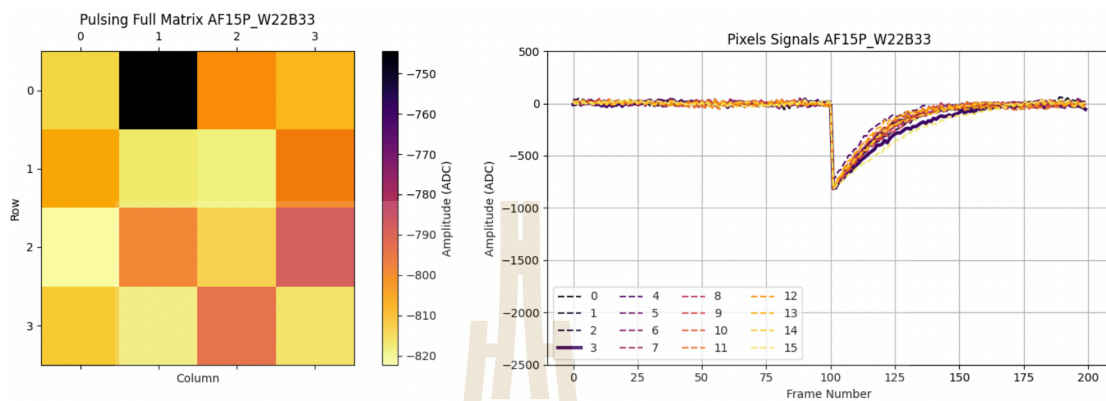


Figure A.12 Pulsing signal of 16 pixels of APTS chip at substrate bias of 0.0 V under temperature of 40 degree Celsius.

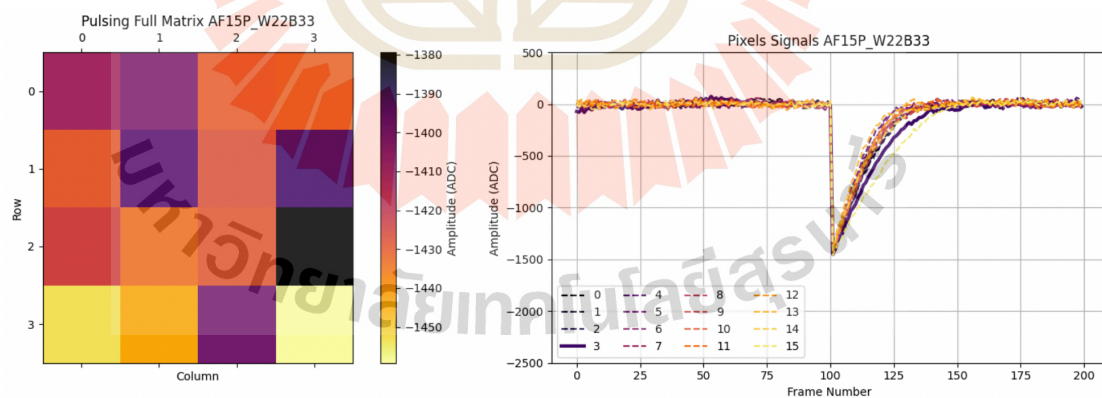


Figure A.13 Pulsing signal of 16 pixels of APTS chip at substrate bias of -1.2 V under temperature of 40 degree Celsius.

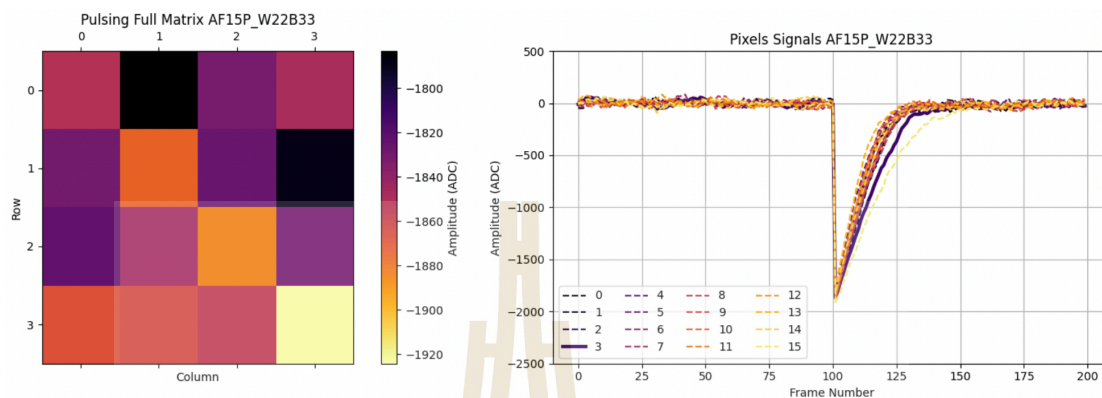


Figure A.14 Pulsing signal of 16 pixels of APTS chip at substrate bias of -2.4 V under temperature of 40 degree Celsius.

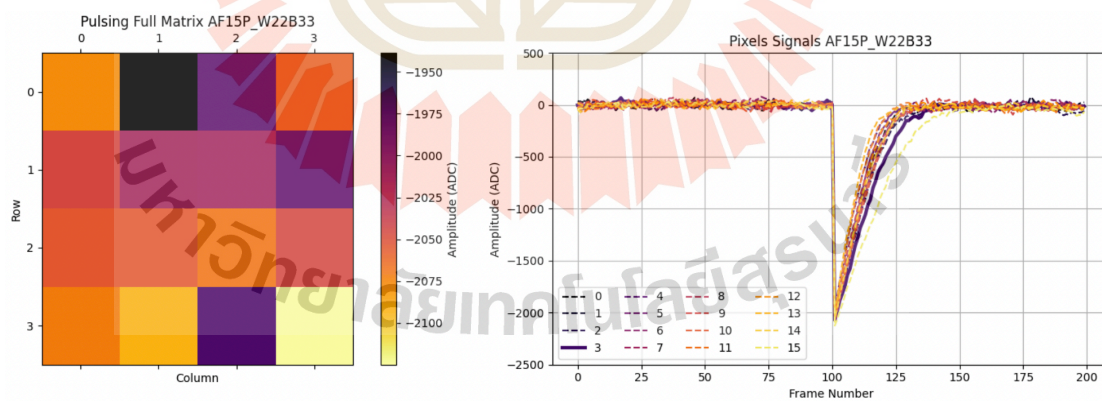


Figure A.15 Pulsing signal of 16 pixels of APTS chip at substrate bias of -3.6 V under temperature of 40 degree Celsius.

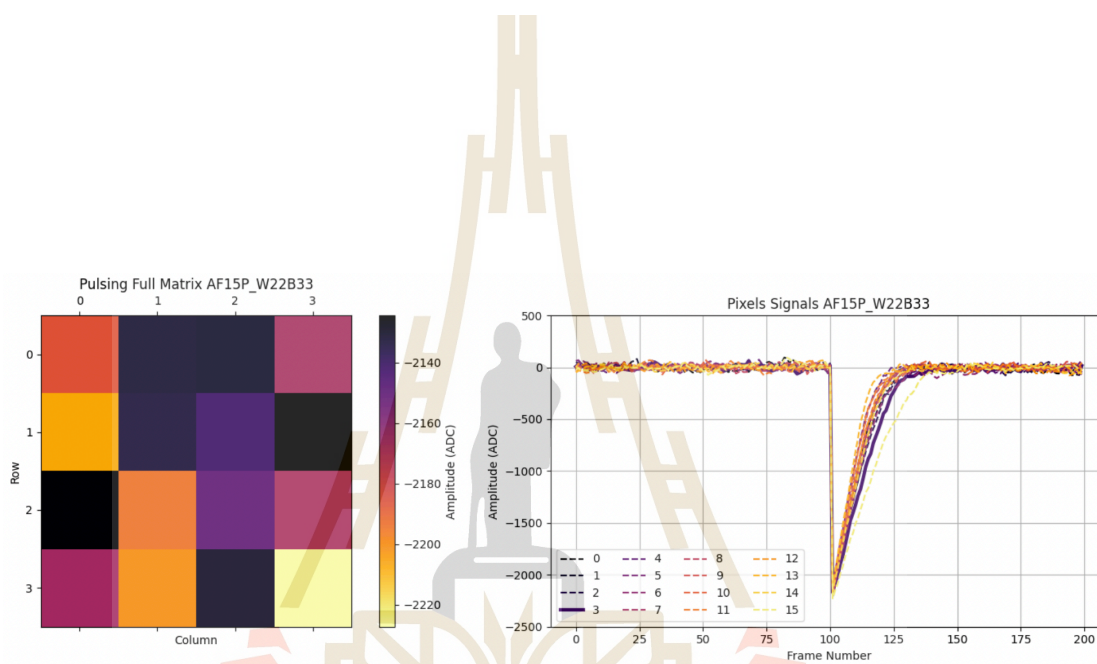


Figure A.16 Pulsing signal of 16 pixels of APTS chip at substrate bias of -4.8 V under temperature of 40 degree Celsius.

APPENDIX B

PERFORMANCE OF IRRADIATED APTS CHIP

APTS sensor was irradiated by a proton beam with a 100 krad and 500 krad TID dose. The APTS sensor was placed in front of the 70 MeV proton beam provided by the radiation test at HRH Princess Maha Chakri Sirindhorn Proton Center (HRSP). The APTS signal was compared to its performance post-irradiation.



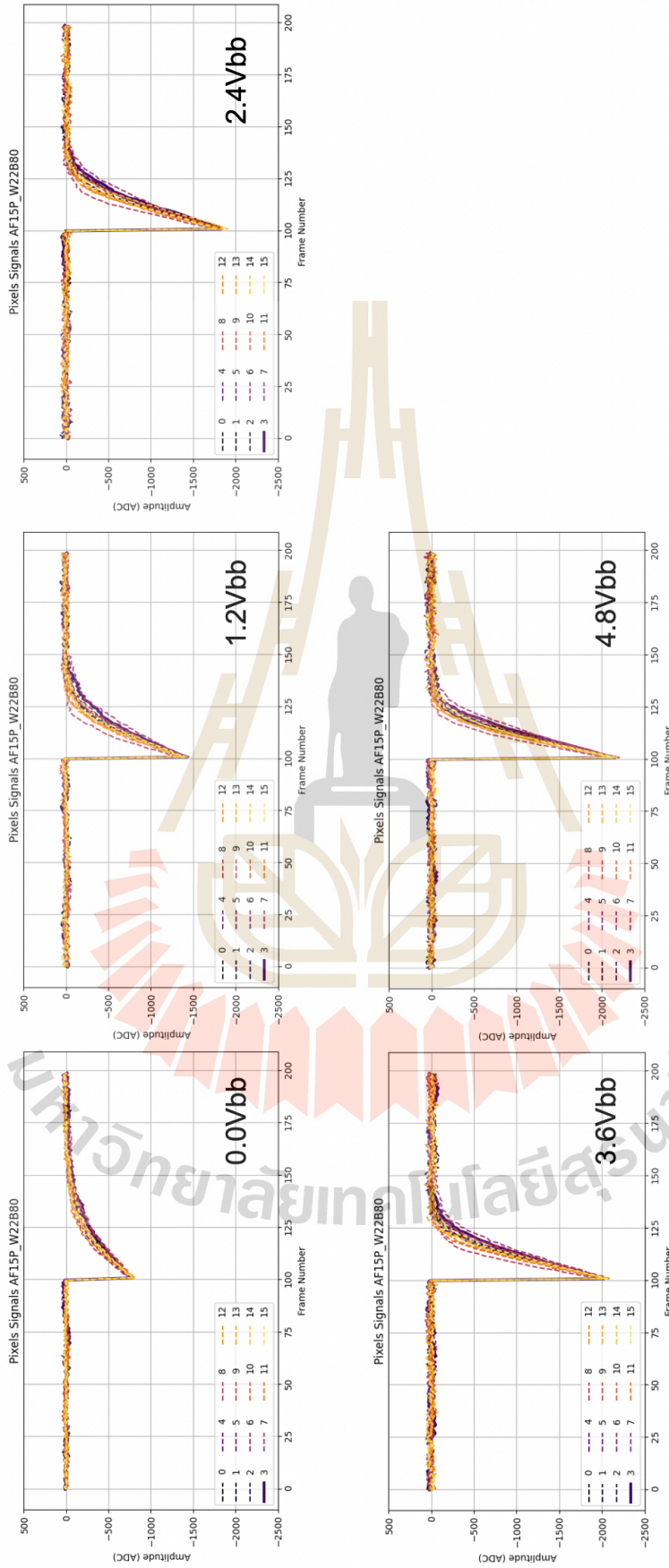


Figure B.1 Plusing signal of non-irradiated APTS chip at different substrate bias.

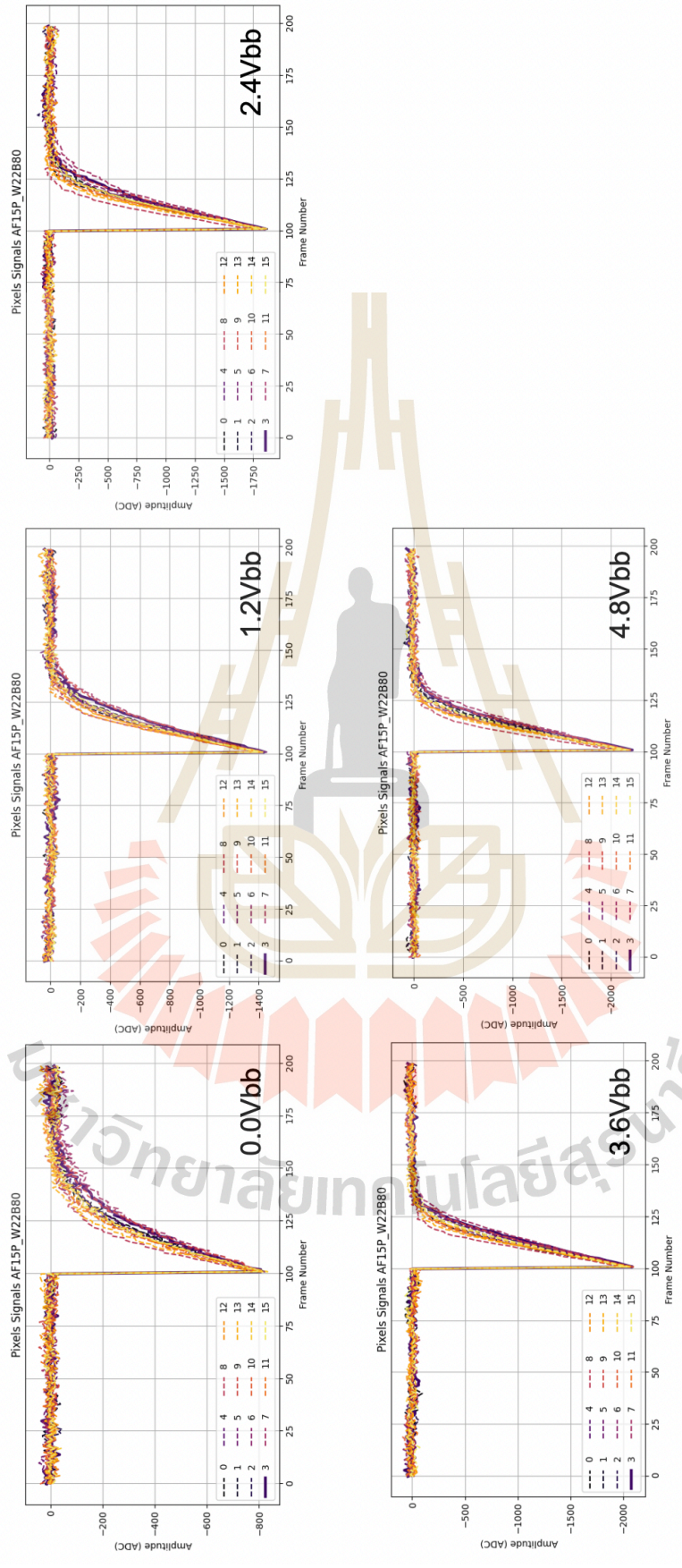


Figure B.2 Pulsing signal of irradiated APTS chip with 100krad TID at different substrate bias.

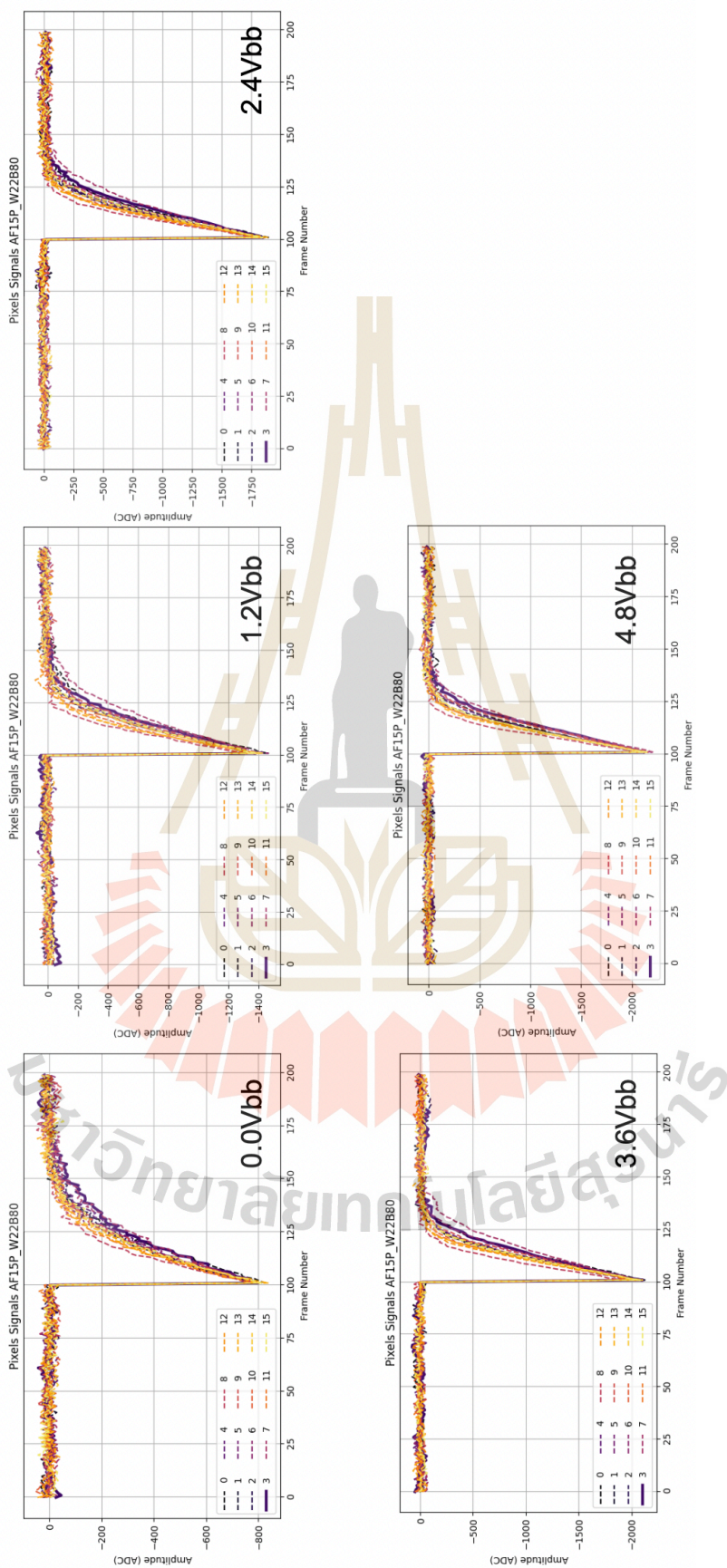


Figure B.3 Pulsing signal of irradiated APTS chip with 500krad TID at different substrate bias.

APPENDIX C

SENSOR CHARACTERIZATION USING 1.2 GEV ELECTRON BEAM

The pixel sensor telescope was installed at the SLRI-BTF, with ALPIDE sensors arranged as reference planes and an APTS sensor positioned in the center between the reference planes as DUT. The pixel telescope spacing between each sensor is set, and the trigger and busy chain signal wiring is connected as depicted in C.1.

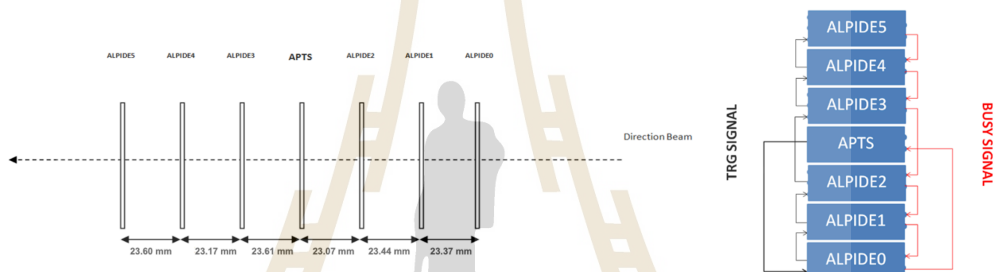


Figure C.1 Drawing schematic of the pixel sensor telescope. The APTS serves as the DUT, and the ALPIDE sensors are positioned in front of and behind the DUT as reference planes (left). The trigger signal wire is utilized for signal transmission within the sensor (right).

After installing the sensor performance test setup, the electron beam detection system is checked. The Timepix sensor takes a hit of the electron beam profile, and a tungsten manipulator was used for adjusting the number of electrons. Additionally, both the EUDAQ software (which sets up and controls the tests of the APTS and ALPIDE sensors) and the Corryvreckan software (which looks at the test results) are validated for beam test measurement. Both programs were developed by the CERN research team, as shown in C.2.

The number of events is set to 100,000 events for data collection. Substrate bias voltage applied to the APTS sensor is set at -1.2 volts. Figure 3 shows the raw hit map of all ALPIDE planes by using the monitoring feature from the EUDAQ software; the proper trigger threshold was used for optimizing the beam profile. Figure 4 displays

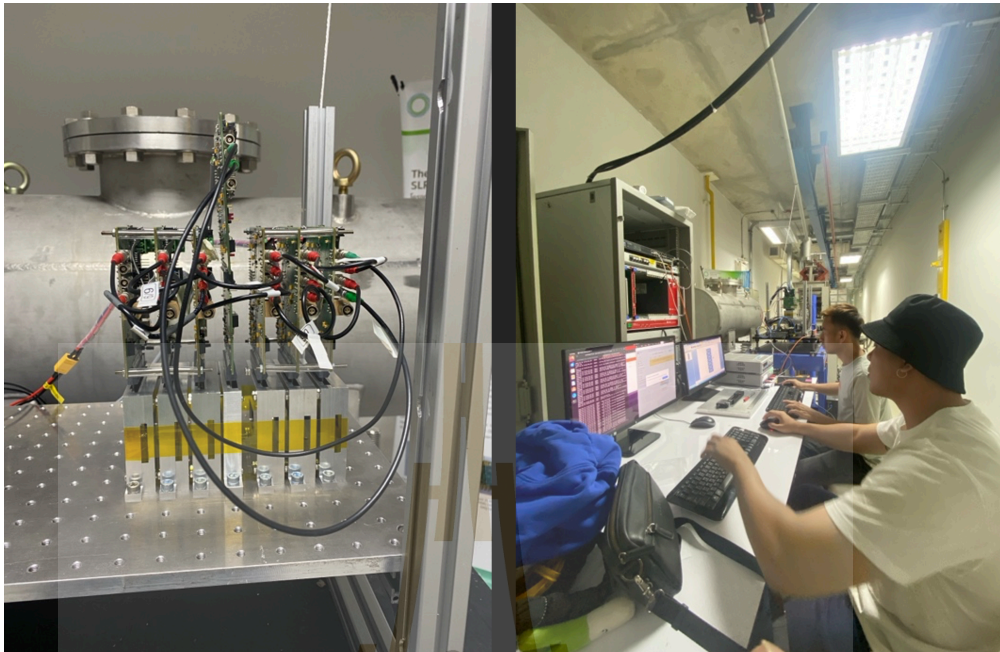


Figure C.2 The installation of the pixel sensor telescope. The setup was positioned in front of the electron beam's trajectory (left). A verification of the program was conducted for sensor testing and data collection (right).

the measurement from the DUT, which has an average cluster size of 3.907 pixels, an average number of clusters of 3.489, and a hit count of 13.63 electrons.

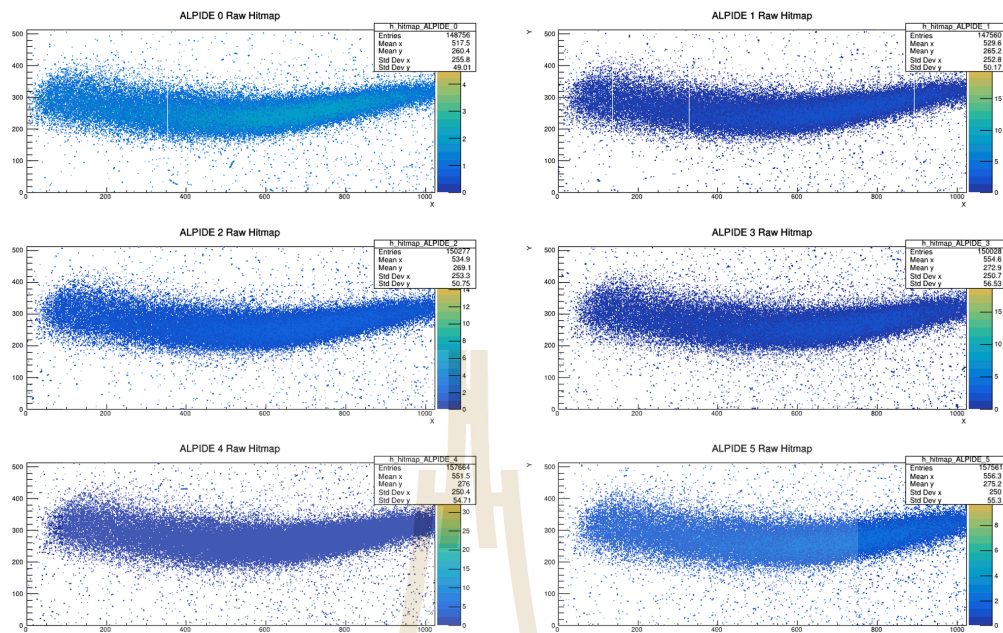


Figure C.3 The raw hit map of the ALPIDE sensor. The electron's hit position was represented as coordinates on the raw hit map, denoted by x and y values.

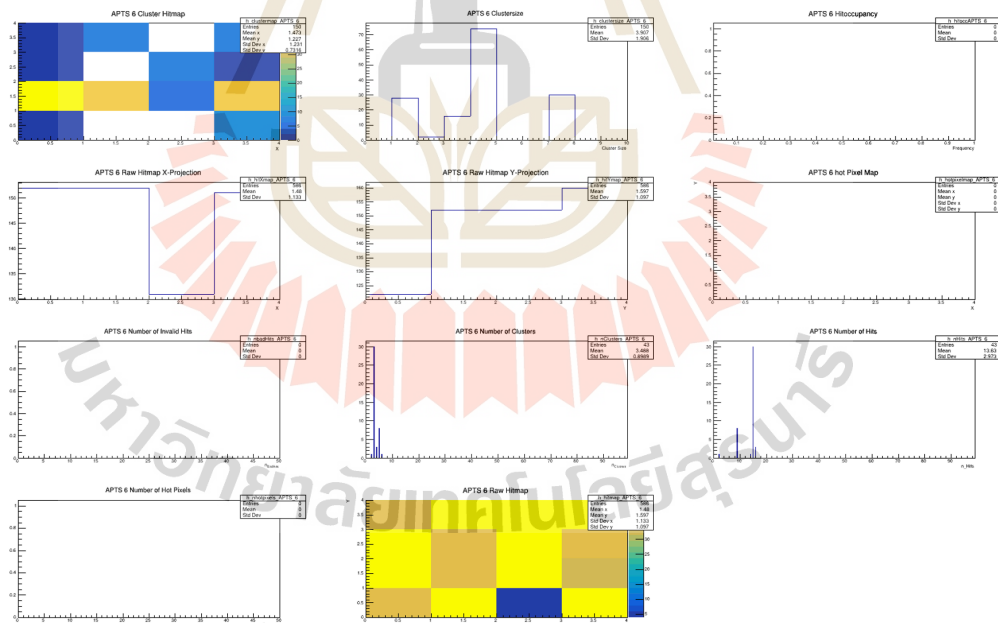


Figure C.4 The observation of the APTS chip as a DUT after being tested with a 1.2 GeV electron beam.

CURRICULUM VITAE

- Name** : Mr. Jetnipit Kaewjai
- Date of Birth** : January 13, 1995
- Place of Birth** : Yasothon, Thailand
- Education** :
- 2016 - 2019 Bachelor of Science, School of Physics, Institute of Science, Suranaree University of Technology, Thailand
- 2019 - 2021 Master of Science, School of Physics, Institute of Science, Suranaree University of Technology, Thailand
- 2021 - 2025 Doctor of Philosophy, School of Physics, Institute of Science, Suranaree University of Technology, Thailand
- Publications** :
1. Gianluca Aglieri Rinella, Giacomo Alocco, Matias Antonelli, **Jetnipit Kaewjai**, et al. (2024) Characterisation of analogue Monolithic Active Pixel Sensor test structures implemented in a 65 nm CMOS imaging process. *Nucl. Instrum. Methods Phys. Res. A* (publishe)
 2. **Jetnipit Kaewjai**, Kritsada Kittimanapun, Natthawut Laojamnongwong, Wanchaloem Poonsawat, Chinorat Kobdaj (2025) Study of the cluster size of a Monolithic Active Pixel Sensor using a Sr-90 source. *Journal of Physics: Conference Series* (published)
 3. Kritsada Kittimanapun, **Jetnipit Kaewjai**, Natthawut Laojamnongwong (2024) Energy selection of synchrotron booster for SLRI beam test facility. *JACoW IPAC2024, THPG10* (published)
 4. Kritsada Kittimanapun, Natthawut Laojamnongwong, **Jetnipit Kaewjai**, Chinorat Kobdaj, Wanchaloem Poonsawat (2023) Commissioning of Pixel Sensor Telescope for Monolithic Active Pixel Sensor Characterization. *Journal of Physics: Conference Series* (published)